博　士　論　文

Development of a low-background particle detector for a direction sensitive dark matter search (方向に感度を持つ暗黒物質探索実験のための低バックグラウンド検出器の開発)

2019年1月

神戸大学大学院理学研究科物理学専攻

Takashi Hashimoto

橋本　隆

Abstract

A number of astronomical observations indicate the existence of the dark matter, but there has not been any success of detecting the dark matter directly. While DAMA/LIBRA group has been claiming the detection of the dark matter, other groups have shown results contradictory to DAMA/LIBRA's claim. In order to overcome this situation, a dark matter search by a more convincing method is expected. A method with a direction sensitivity is said to be one of these methods. NEWAGE (NEw generation WIMP search with an Advanced Gaseous tracker Experiment) is a direction sensitive dark matter search experiment using a μ-TPC (micro Time Projection Chamber) read by a μ-PIC (micro PIxel Chamber). NEWAGE has the world's highest sensitivity in the direction sensitive method. However, the detection sensitivity of NEWAGE has not reached those of the conventional method, and a further improvement is required. The detection sensitivity of NEWAGE is limited by events that are not from the dark matter (background), and understanding and reduction of the background is necessary.

The purpose of this thesis is to understand and reduce the background of NEWAGE to improve the detection sensitivity. The main background was identified as α-rays by a study with a High Purity Germanium detector. Based on the study on the background, a new detector "low-α μ-PIC" was developed by replacing the material containing the main background source with a radio-pure material. It was confirmed that the low-α μ-PIC showed a required performance as a gas detector. The background was measured in an underground laboratory. The detection sensitivity is expected to be improved by a factor of 38^{+38}_{-24}(90 % interval) than the one of the previous run. It was found that some more study with increased statistics taking account of other background sources was still needed for a conclusive result on the background reduction of the μ-PIC.

Contents

1 Introduction

1.1 Dark matter

The dark matter is an unknown matter whose existence is strongly predicted from various astronomical observations. It is described as "Dark" because it can not be observed with electromagnetic waves such as light, X-rays and infrared rays. From the latest astronomical observations, the known matter is only 4.9% of the components of the universe, the remaining 26.8% is considered to be the dark matter and 68.3% is considered to be the dark energy (Figure 1.1[1]). The dark matter is expected to be a particle in a new theory beyond the framework of the standard model, but its nature is unknown, and a large number of researches aiming to discover dark matter around the world are under way.

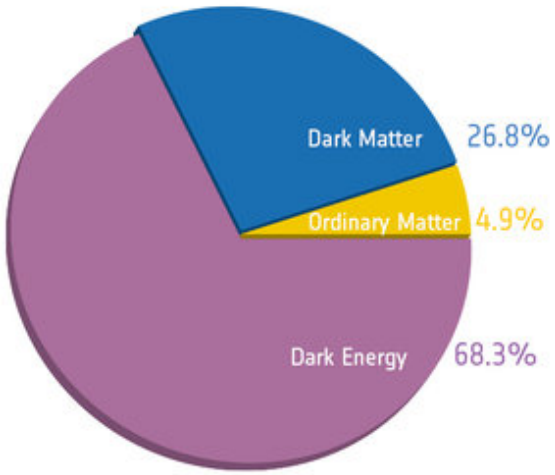

Figure 1.1: The energy composition diagram of the universe. The universe was known to consist of 68.3% dark energy, 26.8% dark matter and 4.9% known matter from the latest astronomical observations[1].

1.2 Dark Matter Evidences

The dark matter was proposed by a Swiss astronomer F. Zwicky in 1937[2]. By estimating the motion of the galaxies, he estimated the total mass of the cluster of galaxies. From the result, The mass of dark matter was 10 $\sim$ 100 times greater than the visible mass expected from the number of galaxies. In response to this result, he proposed "dark matter" as a substance that can not be observed with light to fill up the difference in mass. As observations of galaxies and cluster of galaxies subsequently progressed, various evidences suggesting the existence of dark matter were obtained.

1.2.1 The galactic rotation curve

A representative example showing the presence of the dark matter was the galactic rotation curve problem reported in the 1970s (Figure 1.2). This problem was that the

mass distribution expected from the galactic rotation curve was larger than the mass obtained from the distribution of stars. In order to solve this problem, the dark matter needed to exist over the galaxy scale.

The rotational velocity of the galaxy is calculated from Kepler's law as

$$\frac{v_c^2(r)}{r} = G\frac{M(r)}{r^2} \tag{1.1}$$

where r is a radial distance from the center of the galaxy, $v_c(r)$ is a rotation velocity as a function of r, G is constant of gravitation and $M(r)$ is a total mass within the radius r. The rotation velocity was measured from observations of the Doppler shift of bright lines in the spectra of stars, using 21 cm and 3.6 mm lines of the HI gas (neutral hydrogen gas) and the CO gas. Because the galaxy is very bright at the center part with respect to the disk region, it was thought that the stars concentrate in the center of the galaxy. If a galaxy consisted of only visible matter, since the observed stars concentrated at the center of the galaxy, the rotation velocity$v_c(r)$ should be reduced by $r^{-1/2}$.

Figure 1.2 shows an observed rotation curve of the NGC 6503 galaxy by Doppler shift of 21 cm line[3]. This galaxy has many stars within the radius of 2 kpc from the center. If the mass is concentrated in the center of the galaxy, the rotation curve should be slower at a large radius like the dashed line in Figure 1.2. However, the rotation curve obtained from the observation does not decrease and was distributed at a constant velocity like the point in Figure 1.2. From this result, the existence of massive matters that can not be optically observed in the galactic halo was thought to be indispensable and this invisible matter called dark matter was required in the galactic halo.

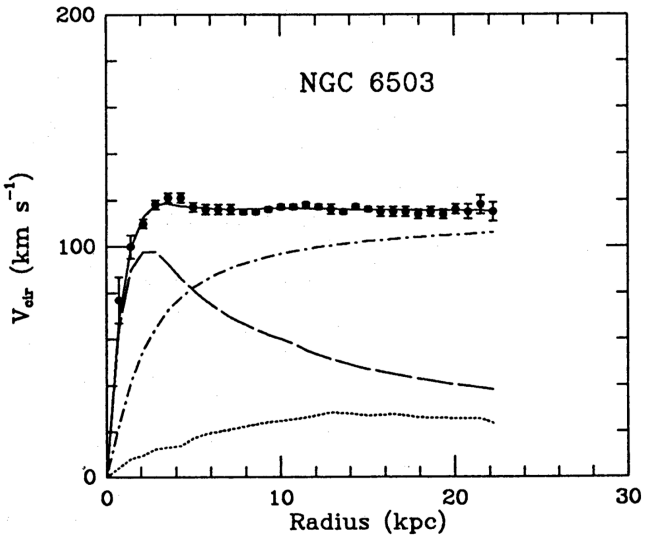

Figure 1.2: The rotation curve of NGC6503 spiral galaxy[3]. The vertical axis represents the rotation velocity of the galaxy, and the horizontal axis represents the distance from the center of the galaxy. The black points are measured velocity by Doppler shift of 21 cm line. The dashed line and the dotted line are contributions of the rotational velocity from the observed disk part and gas respectively, the one-dot chain line is the contribution by the invisible mass of the galactic halo, and the solid line shows the sum of them.

1.2.2 The weak gravitational lens effect

The gravitational lens effect is a phenomenon in which the light path is bent due to the existence of the gravity source. It is called this way because it seems that the gravity source plays a role like a lens. The distribution of the gravity source between the background galaxy and the observer can be known by a statistical investigation of the background galactic distortion using the gravity lens effect. When the gravitational lens effect by the cluster of galaxies is large enough to show the galaxy in the background as an arc, it is called the strong gravity lens effect. On the other hand, if the gravitational lens effect by the cluster of galaxies is relatively small and statistically researches the gravitational lens effect, it is called the weak gravity lens effect.

A cluster of galaxies "1E0657-558" was observed by the Hubble Space Telescope to investigate the mass space distribution of dark matter using the weak gravity lens effect[4]. 1E 0657-558 is called "Bullet Cluster" because it is a cluster of galaxies that emits strong X-rays as a result of collision of a small cluster of galaxies and a large cluster of galaxies. The green line in Figure 1.3 is the spatial distribution of the dark matter observed by using the weak gravitational lens effect. The observation results of 1E 0657-558 with visible light using the Magellan telescope are shown on the left side of Figure 1.3. The observation results on the X-ray using the X-ray astronomical satellite Chandra are shown on the right side of Figure 1.3. The results showed that gravitational potential does not trace the high temperature plasma distribution by observation on the X-ray and weakly interacting dark matter goes ahead in contrast to the viscous plasma. This is one of the evidences of the presence of an astrophysical dark matter at the clusters of galaxies scale.

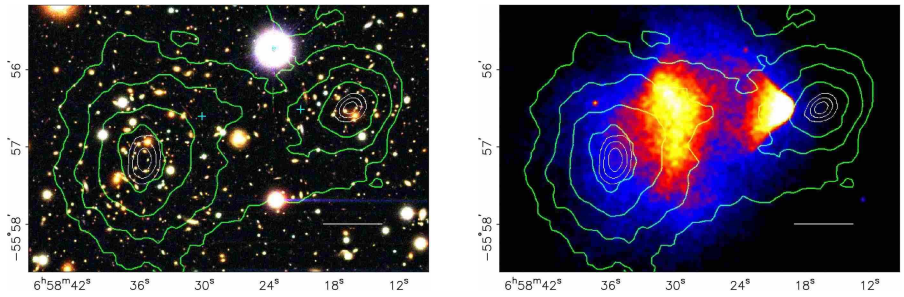

Figure 1.3: Space distribution of 1E 0657-558 where galaxy cluster collided[4]. The left figure shows visible light and the right figure shows the observation result with X-ray. The green contour in both figure is the distribution of gravitational potential measured by weak gravitational lens.

1.2.3 The cosmological parameter measurement

The evolution of the scale factor a, representing the size of universe, is written as

$$\left(\frac{\dot{a}}{a}\right)^2 = H_0^2 \left\{ \frac{\Omega_{\rm m}}{a^3} + \frac{\Omega_{\rm r}}{a^4} + \Omega_\Lambda - \frac{\Omega_{\rm k}}{a^2} \right\}, \tag{1.2}$$

where H_0 is the Hubble constant, $\Omega_{\rm m}$ and $\Omega_{\rm r}$ are the normalized parameters of the matter and radiation and $\Omega_{\rm k}$ is the normalized curvature of the universe. The baryon and the dark matter are discussed separately; the matter($\Omega_{\rm m}$) is divided into baryon($\Omega_{\rm b}$)

and dark matte($\Omega_{\rm DM}$). Eq.(1.2) is the normalized Friedmann equation and derived from general relativity assuming a homogeneous isotropic universe. By solving this differential equation, we can see the state of space development such as the contraction and expansion of the universe, whether the universe is flat or not, presence or absence of a big bang can be discussed. It turned out that the state of space evolution depended on cosmological parameters. The observation results of the cosmological parameters are shown in Figure 1.4. Constraints on Ω_Λ and $\Omega_{\rm m}$ by observations of Type Ia Supernova (IaSN) explosion [5], CMB observation [1], Baryon Acoustic Oscillation (BAO) observation[6] are shown in Figure 1.4. By each three observation, a flat universe with (Ω_Λ, $\Omega_{\rm m}$) $\simeq (0.7, 0.3)$ is favored. On the other hand, from the calculation of BBN, the baryon density $\Omega_{\rm b} = 0.044 \pm 0.004$ is obtained[7]. Since this value is too small to explain the matter density ($\Omega_{\rm m} \simeq 0.3$), it is suggested that there exists a non-baryonic matter (dark matter) of $\Omega_{\rm DM} \simeq 0.25$.

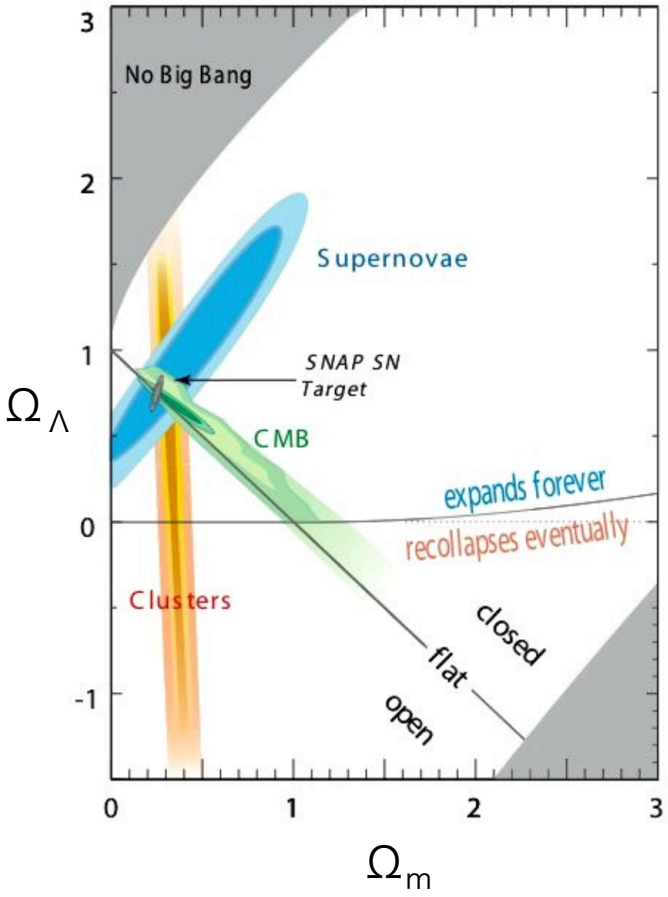

Figure 1.4: Allowed regions of cosmological parameters (Ω_Λ, $\Omega_{\rm m}$) by observations of IaSN ("Supernovae" in figure)[5], CMB[1], and BAO ("clusters" in figure)[6]. A flat universe with (Ω_Λ, $\Omega_{\rm m}$) $\simeq (0.7, 0.3)$ is favored by each three observations.

1.3 Dark Matter Candidates

As mentioned in the previous section, the existence of non-baryon matter (dark matter) is expected. As the dark matter candidates, there are axion[8], sterile neutrino[9], mirror

matter[10] and so on.

One candidate for the dark matter is Weakly Interacting Massive Particles (WIMPs). WIMP is a particle made from the theory beyond the energy scale ($> 1\,\mathrm{TeV}$) of the standard model (SM), and because of its properties it is a powerful candidate for the dark matter. There are several theories which produce WIMPs, and one of the representative ones is supersymmetry theory (SUSY). SUSY is a theory that predicts supersymmetric particles(SUSY particles) which have spins 1/2 different from those of SM particles. If the lightest particle (LSP) among the SUSY particles was electrically neutral, it could be a candidate for the dark matter[11]. In particular, " Neutralino " whose existence is produced by SUSY can be a good dark matter candidate. The theory that extended SM based on the minimum SUSY is called Minimum Supersymmetric extension of the Standard Model (MSSM) and introduces SUSY particles as shown in Table 1.1.

Table 1.1: SUSY particles introduced by MSSM[12].

SM particles			SUSY particles		
symbol	Name	Spin	symbol	Name	Spin
$q = u, c, t$	up quarks	1/2	$\tilde{q}_u^1, \cdots \tilde{q}_u^6$	up squarks	0
$q = d, s, b$	down quarks	1/2	$\tilde{q}_d^1, \cdots \tilde{q}_d^6$	down squarks	0
$l = e, \mu, \tau$	leptons	1/2	$\tilde{l}_6, \cdots \tilde{l}_6$	sleptons	0
ν_e, ν_μ, ν_τ	neutrinos	1/2	$\tilde{\nu}_1, \tilde{\nu}_2, \tilde{\nu}_3$	sneutrinos	0
g	gluons	1	$\tilde{g}$	gluinos	1/2
$W^\pm$	W bosons	1	$\tilde{\chi}_1^\pm, \tilde{\chi}_2^\pm$	charginos	1/2
$H^\pm$	charged higgs	0			
γ	photon	1	$\tilde{\chi}_1^0, \cdots \tilde{\chi}_4^0$	neutralinos	1/2
Z^0	Z boson	1			
h^0	light scaler Higgs	0			
H^0	heavy scaler Higgs	0			
A^0	pseudoscalar Higgs	0			

The intereaction between SUSY particles and SM particles is determined by R parity given as

$$R = (-1)^{3B+L+2S}, \tag{1.3}$$

where B, L and S are the baryon number, the lepton number and the spin, respectively. SM particles and SUSY particles have R parity of 1 and -1, respectively. From the conservation of R parity before and after the interaction, the LSP can not decay to SM particles without SUSY particles and can exist stably. LSP is the lightest gluino or chargino or neutralino, whose spins are 1/2. If LSP is the lightest neutralino, the neutralino can be a candidate of the dark matter.

1.4 Method of direct detection dark matter search

The direct detection aims to detect the WIMPs via WIMP-recoil nucleus elastic scatterings. The direct search could provide a direct evidence of the existence of dark matter

in the galactic halo. In this chapter the dark matter specific signals are discussed.

1.4.1 Dark Matter Direct Detection

In the direct search, the expected energy spectrum can be predicted in advance assuming the elastic scatterings of WIMP-nucleus interaction. The energy spectrum can be calculated by considering the relative velocity of WIMP and the earth[13].

The solar system is rotating at a distance of 8 kpc from the center of the galaxy, and the earth revolves around the sun. Thus, the velocity of the earth relative to the galactic halo is written as

$$\begin{aligned} v_{\rm E}(=|\mathbf{v}_{\rm E}|) &= v_{\rm sun} + v_{\rm orb}\cos\theta_{\rm orb}\sin 2\pi y \\ &\simeq 244 + 15\sin(2\pi y)\ [\mathrm{km/sec}], \end{aligned} \tag{1.4}$$

where $v_{\rm sun}$ is the velocity of the Sun relative to the galactic halo, $v_{\rm orb}$ is the orbital rotation velocity of the earth around the sun, $\cos\theta_{\rm orb}$ is the inclination of the earth orbital plane with respect to the galactic plane and y is the time in year from March 2nd. Figure 1.5 is a schematic diagram showing the movement of the sun and the earth in the galaxy. The earth revolves around the sun, and in June the relative velocity reaches the maximum because the direction of revolution of the earth and the direction of travel of the solar system are the same. On the other hand, the direction of revolution of the earth and the direction of travel of the solar system are opposite in December, so the relative velocity becomes the minimum.

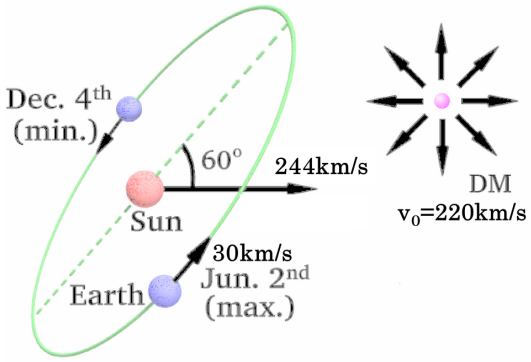

Figure 1.5: Schematic diagram the movement of the dark matter (DM), the sun, and the earth in the galaxy.

The differential density of WIMP dn is expressed using $v_{\rm E}$

$$dn = \frac{n_0}{k} f(\mathbf{v}, \mathbf{v}_{\rm E}) d^3v, \tag{1.5}$$

$$n_0 \equiv \int_0^{v_{\rm esc}} dn\,, \qquad k = \int_0^{2\pi} d\phi \int_{-1}^{+1} d(\cos\theta) \int_0^{v_{\rm esc}} f(\mathbf{v}, \mathbf{v}_{\rm E}) v^2 dv\,,$$

where k is the normalization constant, n_0 is the mean number density of WIMP, $v_{\rm esc}$ is the escape velocity of the galaxy, θ is the angle between $\mathbf{v}_{\rm E}$ and WIMP velocity, and

ϕ is azimuth angle taking WIMP velocity vector as a zenith. Here, assuming that the velocity distribution of the dark matter $f(\mathbf{v}, \mathbf{v}_{\rm E})$ follows the Boltzmann distribution

$$f(\mathbf{v}, \mathbf{v}_{\rm E}) = e^{-(\mathbf{v}+\mathbf{v}_{\rm E})^2/v_0^2}\,, \tag{1.6}$$

where v_0 is the velocity dispersion of our galaxy. The normalization constant k is derived in case $v_{\rm esc}$ is infinite or not as

$$k = k_0 = (\pi v_0^2)^{3/2} \qquad (v_{\rm esc} = \infty) \tag{1.7}$$

$$k = k_1 = k_0 \left\{ {\rm erf}\left(\frac{v_{\rm esc}}{v_0}\right) - \frac{2}{\pi^{1/2}} \frac{v_{\rm esc}}{v_0} e^{-v_{\rm esc}^2/v_0^2} \right\} \qquad (v_{\rm esc} \neq \infty), \tag{1.8}$$

where ${\rm erf}(x) \equiv \frac{2}{\pi^{1/2}} \int_0^x e^{-t^2} dt$ is the error function.

Next, the event number R of WIMP per observation time with 1 kg of target mass (total rate unit: tru) is discussed. R is written as

$$dR = \frac{N_{\rm A}}{A} \sigma v dn, \tag{1.9}$$

where $N_{\rm A}$ is the Avogadro number(6.02×10^{23}), A is the mass number of the target nucleus, $v = |\mathbf{v} - \mathbf{v}_{\rm E}|$ is the dark matter velocity relative to the target, σ is the WIMP-nucleus cross section. Strictly, σ depends on the momentum transfer. Precise scattering cross section that takes momentum transfer into account and here only a simplified case, $\sigma = \sigma_0$ (constant) is discussed. R is derived by integrating Eq.(1.9) as

$$R = \frac{N_0}{A} \sigma_0 \int v dn. \tag{1.10}$$

The total event rate R_0 for $v_{\rm E} = 0$ and $v_{\rm esc} = \infty$ is described as

$$R_0 = \frac{2}{\pi^{1/2}} \frac{N_{\rm A}}{A} \frac{\rho_{\rm D}}{M_{\rm D}} \sigma_0 v_0 \tag{1.11}$$

$$= \frac{361}{M_{\rm D} M_{\rm N}} \left(\frac{\sigma_0}{1\,{\rm pb}}\right) \left(\frac{\rho_{\rm D}}{0.3\,{\rm GeV/c^2/cm^3}}\right) \left(\frac{v_0}{220\,{\rm km/s}}\right), \tag{1.12}$$

where $\rho_{\rm D}$ is the local mass density of the dark matter, $M_{\rm D}$ is the mass of the dark matter, $M_{\rm N}(= 0.932A)$ is the mass of the target nucleus. Also, Eq.(1.12) is normalized with $\sigma_0 = 1\,{\rm pb}$, $\rho_{\rm D} = 0.3\,{\rm GeV/c^2/cm^3}$, $v_0 = 220\,{\rm km/s}$.

Next, the energy spectrum $\frac{dR}{dE_{\rm R}}$ of recoil nucleus elastically scattered with WIMP is discussed. Assuming that the kinetic energy of WIMP in the laboratory system is $E\left(= \frac{1}{2} M_{\rm D} v^2\right)$, the recoil energy $E_{\rm R}$ received by the nucleus of mass $M_{\rm N}$ is

$$E_{\rm R} = Er\left(1 - \cos\theta\right)/2, \tag{1.13}$$

$$r = \frac{4 M_{\rm D} M_{\rm N}}{\left(M_{\rm D} + M_{\rm N}\right)^2}, \tag{1.14}$$

where θ is the scattering angle in the center of mass system, r is a kinematic factor for $M_{\rm N}$. Assuming an isotropic scattering in the center of mass system, the $\cos\theta$ distribution

becomes uniform and the $E_{\rm R}$ distribution becomes in flat the energy range $0 \leq E_{\rm R} \leq Er$. Therefore, the energy spectrum $\frac{dR}{dE_{\rm R}}$ is written as

$$\begin{aligned} \frac{dR}{dE_{\rm R}} &= \int_{E_{\rm min}}^{E_{\rm max}} \frac{1}{Er} dR(E) \\ &= \frac{1}{E_0 r} \int_{v_{\rm min}}^{v_{\rm max}} \frac{v_0^2}{v^2} dR(v), \end{aligned}$$

where, $E_{\rm min} = E_{\rm R}/r$ is the minimum WIMP kinetic energy that can pass the recoil energy $E_{\rm R}$ to the recoiling nucleus. $E_{\rm max}$ is the maximum value of WIMP's kinetic energy in the laboratory system determined by $v_{\rm esc}$ and Earth movement. $v_{\rm min}, v_{\rm max}(= v_{\rm esc})$ are the corresponding WIMP velocities, respectively, and are defined as $E_0 = \frac{1}{2} m_{\rm D} v_0^2 = \frac{v_0^2}{v^2} E$. The energy spectrum is obtained using Eq.(1.5), (1.6) and (1.9) as

$$\frac{dR}{dE_{\rm R}} = \frac{R_0}{E_0 r} \frac{k_0}{k} \frac{1}{2\pi v_0^2} \int_{v_{\rm min}}^{v_{\rm max}} \frac{1}{v} f(\mathbf{v}, \mathbf{v}_{\rm E}) d^3 v. \tag{1.15}$$

By performing the integration of Eq.(1.15), the specific formula of energy spectra are obtained as

$$\frac{dR(0,\infty)}{dE_{\rm R}} = \frac{R_0}{E_0 r} e^{-E_{\rm R}/E_0 r}, \tag{1.16}$$

$$\frac{dR(0,v_{\rm esc})}{dE_{\rm R}} = \frac{k_0}{k_1} \left[\frac{dR(0,\infty)}{dE_{\rm R}} e^{-E_{\rm R}/E_0 r} - \frac{R_0}{E_0 r} e^{-v_{\rm esc}^2/v_0^2} \right], \tag{1.17}$$

$$\frac{dR(v_{\rm E},\infty)}{dE_{\rm R}} = \frac{R_0}{E_0 r} \frac{\pi^{1/2}}{4} \frac{v_0}{v_{\rm E}} \left[\mathrm{erf}\left(\frac{v_{\rm min} + v_{\rm E}}{v_0} \right) - \mathrm{erf}\left(\frac{v_{\rm min} - v_{\rm E}}{v_0} \right) \right], \tag{1.18}$$

$$\frac{dR(v_{\rm E},v_{\rm esc})}{dE_{\rm R}} = \frac{k_0}{k_1} \left[\frac{dR(v_{\rm E},\infty)}{dE_{\rm R}} - \frac{R_0}{E_0 r} e^{-v_{\rm esc}^2/v_0^2} \right]. \tag{1.19}$$

In Figure 1.6, a normalized energy spectrum is shown.

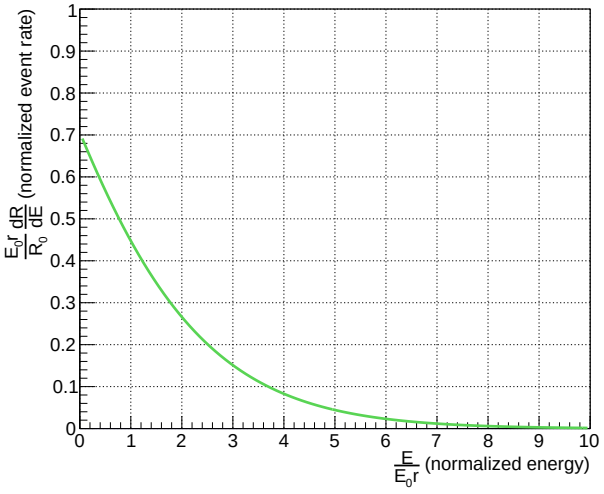

Figure 1.6: Normalized energy spectrum of elastic scattered nucleus.

The energy spectrum from the dark matter has a seasonal variation called "annual modulation". The annual modulation of the energy spectrum is caused by the Earth's motion v_E around the sun as described in Eq.(1.5). v_E is the largest on June 2nd and the smallest on December 4th. The annual modulation size is less than $O(v_{\rm orb}/v_{\rm sun}) \sim 5\%$. Figure 1.7 shows the energy spectra expected in June and December, where the target is ^{19}F for the spin-dependent interaction, $M_{\rm D} = 100\,{\rm GeV}$, and $\sigma^{\rm SD}_{\chi-{\rm p}} = 1\,{\rm pb}$.

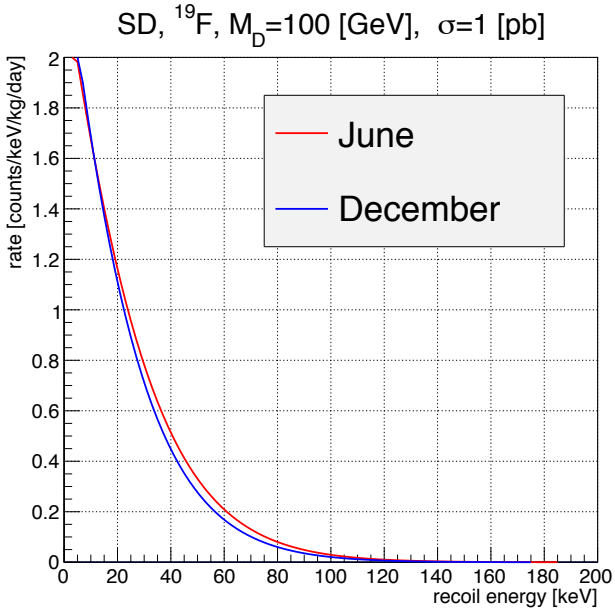

Figure 1.7: The energy spectra expected in June and December, where the target is ^{19}F for the spin-dependent interaction, $M_{\rm D} = 100\,{\rm GeV}$, and $\sigma^{\rm SD}_{\chi-{\rm p}} = 1\,{\rm pb}$.

The DAMA group has reported the discovery of dark matter from the observation of the annual modulation since 1998[14],[15]. In order to increase the reliability of the result, DAMA newly used 250 kg of NaI (Tl) scintillator of higher purity as DAMA/LIBRA and again annual modulation was observed again[16](Figure 1.8). The total exposure of DAMA / NaI and DAMA / LIBRA were 2.46 ton·year, and they strongly claimed on the discovery of the dark matter. However, since other experiments have shown the results contradictory to this DAMA's claim, there has been no consensus of the direct detection of the dark matter. There is also a discussion that the annual modulation observed by DAMA was systematic errors due to cyclic backgrounds (neutrons from muon and solar neutrinos)[17]. Because of these backgrounds, dark matter searches by different methods with more clear signals are required.

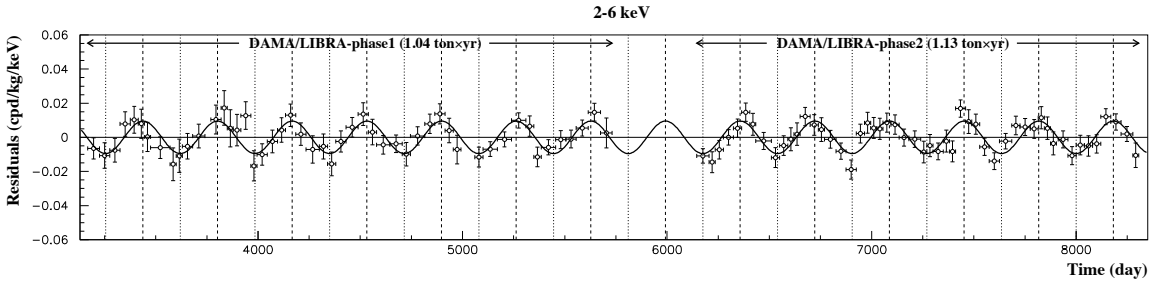

Figure 1.8: The observation result of the annual modulation in 2-6 keV region by DAMA, DAMA / LIBRA[16].

1.4.2 Directionality

The most convincing signal of the dark matter would be seen in the directional distribution of the recoil nucleus. This is the evidence of the detection of the dark matter by measuring the direction of "dark matter wind" caused by the movement of the solar system in the galaxy. Since the solar system is moving towards the constellation Cygnus direction in the galaxy system, dark matter can be interpreted as the are coming from the Cygnus direction. Since the Cygnus direction is varying time-to-time even in a day, the systematic error depending on day and season can be canceled.

In the laboratory system, the expected angular spectrum due to elastic scattering of the dark matter is calculated as follows[18]

$$\frac{d^2R}{dE_{\mathrm{R}}d\cos\theta} \simeq \frac{1}{2}\frac{R_0}{E_0 r}\exp\left[-\frac{(v_{\mathrm{E}}\cos\theta - v_{\mathrm{min}})^2}{v_0^2}\right] \tag{1.20}$$

where θ is the angle between the direction of the Cygnus and the nuclear track. The relation between this angle and energy is shown in Figure 1.9, where the target is ^{19}F for the spin-dependent interaction, $M_{\mathrm{D}} = 100\,\mathrm{GeV/c^2}$ and $\sigma^{\mathrm{SD}}_{\chi-\mathrm{p}} = 1\,\mathrm{pb}$. Figure 1.10 is obtained by extracting events whose recoil energy is in $100 - 120\,\mathrm{keV}$ from Figure 1.9. Because the $\cos\theta$ distribution due to isotropic background events is expected to be flat, the peak at $\cos\theta = 1$ as shown in Figure 1.10 could be a strong evidence for the detection of the dark matter.

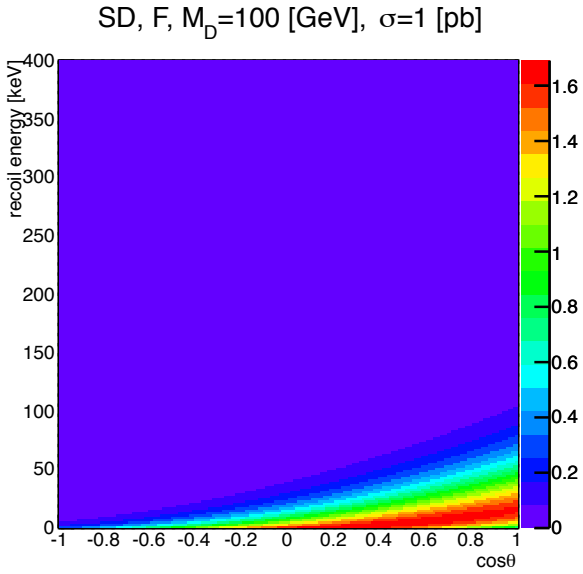

Figure 1.9: The expected energy-angular distribution due to the elastic scattering of the dark matter. θ is the angle between the direction of the Cygnus and the nuclear track, the target is ^{19}F for the spin-dependent interaction, $M_{\mathrm{D}} = 100\,\mathrm{GeV/c^2}$ and $\sigma^{\mathrm{SD}}_{\chi-\mathrm{p}} = 1\,\mathrm{pb}$.

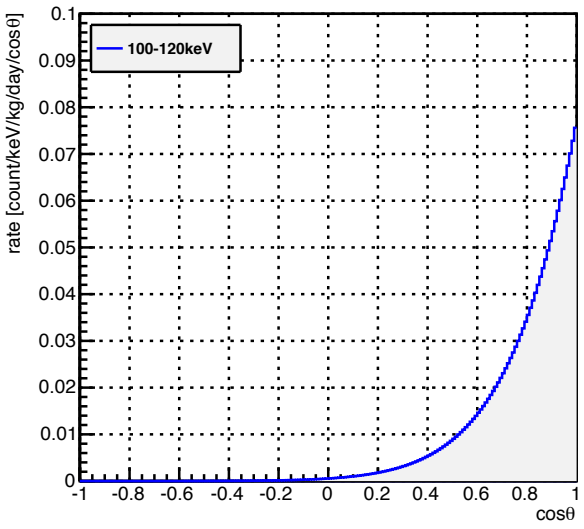

Figure 1.10: The expected $\cos\theta$ distribution$(100 - 120\,\mathrm{keV})$. θ is the angle between the direction of the Cygnus and the nuclear track, the target is ^{19}F for the SD interaction, $M_{\mathrm{D}} = 100\,\mathrm{GeV/c^2}$ and $\sigma^{\mathrm{SD}}_{\chi-\mathrm{p}} = 1\,\mathrm{pb}$.

In the direct detection dark matter search experiments, the direction of the dark matter to the detector is measured by detecting the track of recoil nucleus. A typical track length when the energy of the recoil nucleus is 100 keV is 1 mm or less in gas at the atmospheric pressure. For this reason, a lot of direction-sensitive dark matter search experiments are carried out with gaseous detectors using low pressure gas. In the direction-sensitive dark matter search experiments, Time Projection Chamber (TPC) combined with MPGD

(Micro-Patterned Gaseous Detector) using low pressure gas is generally used. It is called μ-TPC. MPGD used in the direction sensitive dark matter search experiments is will be reviewed in Chapter 2.2.

Figure 1.11 shows a conceptual diagram of a μ-TPC. A μ-TPC can obtain the track of charged particles. When charged particles recoiled by elastic scattering with a dark matter move through the gas, gas is ionized along the track. Primary electrons generated by the ionization are drifted in the -Z direction by the drift electric field applied inside the μ-TPC, and two-dimensional information of the track can be obtained on the reading device (XY plane). At this time, by considering the drift velocity of electrons and the time required for drift, the Z coordinate can be obtained and three dimensional track information can be obtained.

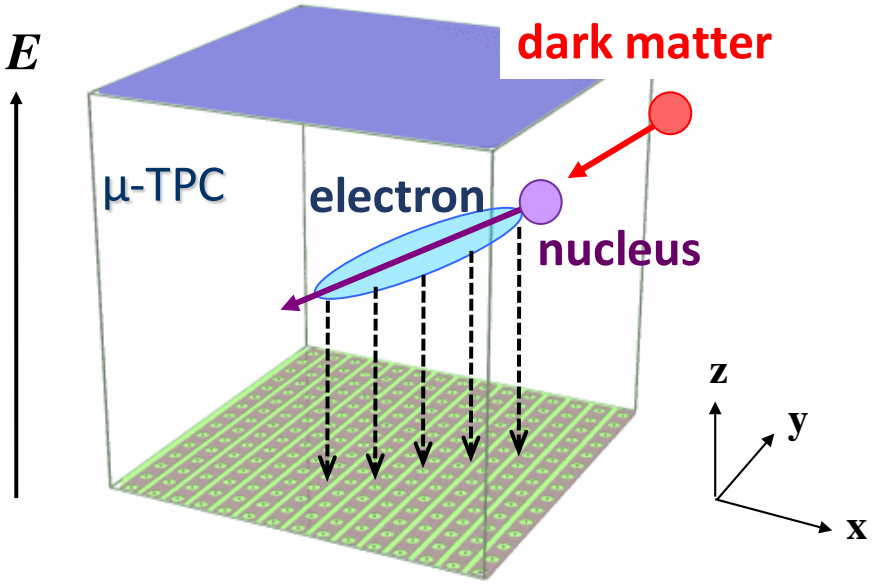

Figure 1.11: A conceptual diagram of TPC.

There are DRIFT[19] in the UK and DM-TPC[20] in the United States for the direction sensitive dark matter search experiment using gas detectors. The DRIFT group is a pioneer in the direction sensitive dark matter search experiments, and research on background reduction techniques is progressing particularly. The detector is a $1\,\mathrm{m}^3$ gas detector, and MWPC (Multi Wire Proportional Counter) is used for the readout device. The gas is a mixed gas of 30 Torr CS_2, 10 Torr CF_4 and 1 Torr O_2. Analysis using direction information has not been demonstrated yet, still the limits competitive with large conventional detectors were obtained. DM-TPC uses CCD for the readout device. Tracks can be obtained by reading the scintillation photons emitted by the drifted electrons with a CCD camera. Therefore, although the track obtained is two-dimensional, energy deposit of nucleus along tracks can be easily obtained as information of light intensity.

2 Review of gaseous particle detectors

This section summarizes the amplification principle and variation of gaseous particle detectors and their applications to low background experiments.

2.1 Physical process of the gas detectors

As a charged particle passes through the gas medium, ionization occurs along its track and electron-ion pairs are generated. The number n of electron-ion pairs generated by the charged particle is expressed as follows

$$n = \frac{Y_{\mathrm{dp}}}{W}, \tag{2.1}$$

where Y_{dp} is the total energy deposition in the gas and W is the average energy to produce an electron-ion pair. W is called "W-value". W-values of the gas used in the gas detector are summarized in Figure 2.1 together with other physical properties. In addition to the process of forming electron-ion pairs by the ionization, there is a process of generating excited molecules by exciting electrons to a higher bound state of molecules. In the case of the mixture gas, the excited noble gas molecules interact with the other gas to generate electrons. This process is called "Penning effect". Transfer probabilities to Penning effect in argon with 10 % alkane at 760 Torr is shown in Figure 2.2[21]. The four reaction formulas (Eq.(2.2), (2.3), (2.4) and (2.5)) occurred by the Penning effect are shown below. The most common mechanisms are the two-body collision of an excited atom with mixture gas molecule, which are shown as follows

$$A^* + B \rightarrow (AB)^+ + e^-, \tag{2.2}$$

$$A^* + B \rightarrow A + B^+ + e^-, \tag{2.3}$$

where, A and B represent the type of gas, and * represents the excited state. The reaction that occurs when A^* returns to the ground state is as follows

$$\begin{aligned} A^* &\rightarrow A + e^-, \\ B^* &\rightarrow B^+ + e^-. \end{aligned} \tag{2.4}$$

This process works over distances that are large compared with the molecule size. The bonding state of the excited noble gas atom and the ground state is known as "excimer". At atmospheric pressure, excimer is formed with three molecules of argon gas, and the following reaction occurs

$$\begin{aligned} A^* + 2A \rightarrow \; & A_2^* + A \\ & A_2^* + B \rightarrow 2A + B^* \\ & A_2^* + B \rightarrow 2A + B^+ + e^-. \end{aligned} \tag{2.5}$$

Gas unit	Density, mg cm^{-3}	E_x eV	E_I eV	W_I eV	$dE/dx\|_{\min}$ keV cm^{-1}	N_P cm^{-1}	N_T cm^{-1}
He	0.179	19.8	24.6	41.3	0.32	3.5	8
Ne	0.839	16.7	21.6	37	1.45	13	40
Ar	1.66	11.6	15.7	26	2.53	25	97
Xe	5.495	8.4	12.1	22	6.87	41	312
CH_4	0.667	8.8	12.6	30	1.61	28	54
C_2H_6	1.26	8.2	11.5	26	2.91	48	112
iC_4H_{10}	2.49	6.5	10.6	26	5.67	90	220
CO_2	1.84	7.0	13.8	34	3.35	35	100
CF_4	3.78	10.0	16.0	54	6.38	63	120

Figure 2.1: Properties of noble and molecular gases at normal temperature and pressure(NTP: 20°C, 760 Torr)[22].W_I is an average energy per electron-ion pair(W value).

Alkane	Ionisation potential [eV]	Molecular weight [g/mol]	Transfer probability
CH_4	12.65	16.04	0.212 ± 0.002
C_2H_6	11.52	30.07	0.31 ± 0.01
C_3H_8	10.95	44.096	0.43 ± 0.01
iC_4H_10	10.67	58.123	0.40 ± 0.01

Figure 2.2: Transfer probabilities to Penning effect in argon with 10 % alkane at 760 Torr[21].

Next, the movement of electrons and ions in the gas is explained. Ions and electrons generated by the ionization attract each other and recombine to return to neutral atoms. This recombination process can be suppressed by applying an electric field in the gas and drifting ions and electrons opposite directions. Positive ions move in the electric field direction, and electrons move towards the opposite direction to the electric field. Ions are accelerated by an electric field, collide with gas molecules, stop drifting and are accelerated by an electric field repeatedly. The drift velocity differs depending on the kind of ions. The drift velocity of the ions, ω, is expressed as follows

$$w = \mu \frac{E}{p/p_0}, \tag{2.6}$$

where the constant parameter μ is "mobility" of ions, E is the electric field, p is the pressure of the gas, and p_0 is the atmospheric pressure (760 Torr). μ is determined by the gas molecules. For example, μ of the argon ion in argon gas is 1.7 cm^2/(V $\cdot$ s). The dependence of w on E and p can be represented by a parameter, E/p so called the "reduced electric field". Electrons are also drifted in the same process as ions, but the distance until electrons cause ionizations, called mean free path λ, is shorter than that of ions. Therefore, electrons are accelerated much more than ions. It is known that the drift velocity of ions is 1 cm/ms in the order, whereas that of electrons are 1 cm/us in the order which is about 1000 times faster than the ions.

The principle of gas amplification is then explained. The larger the electric field, the more ionization occurs. This process, called secondary ionization, is caused by the

movement of the electrons generated by charged particles. α, which is the inverse of λ is called the first Townsend coefficient. α represents the number of ion pairs generated per a unit drift distance. α depends on the electric field E and the gas type as follows

$$\alpha = pA\exp(-\frac{B}{E/p}), \tag{2.7}$$

where p is the gas pressure and A and B are parameters depending on the gas type. The total number $N(x)$ of electrons after passing through the trajectory x is obtained as follows. The number $dN(x)$ of electrons amplified during the length dx is written as follows,

$$dN(x) = N(x)\alpha dx. \tag{2.8}$$

If alpha does not depend on x, this solution is as follows

$$N(x) = n_0\exp(\alpha x). \tag{2.9}$$

where, n_0 is the initial number of electrons. From this relation it can be seen that the amplification increases exponentially with respect to the trajectories of electrons. When α depends on x

$$N(x) = n_0\exp\left(\int \alpha(x)dx\right). \tag{2.10}$$

From Eq.(2.10), the gas amplification factor M is expressed as follows

$$M = N(x)/n_0 = \exp\left(\int \alpha(x)dx\right) \tag{2.11}$$

2.2 Variations of gaseous particle detectors

In the direction-sensitive dark matter search experiments, the MPGD is often used because it is necessary to detect the nuclear tracks of 1 mm or less. Several types of MPGDs used in the dark matter search experiments are introduced in this section.

2.2.1 GEM

The GEM (Gas Electron Multiplier) is an MPGD developed by F. Sauli in 1997[23]. The structure standard GEM developed in CERN is explained as an example. Enlarged photograph of the GEM by the electron microscope is shown in Figure 2.3[24]. Copper foils(electrodes) with a thickness of 5 µm are formed on the both sides of a polyimide film (insulator) with a thickness of 50 µm. The holes with a diameter of 70 µm are made at intervals of 140 µm in the film. The GEM is only to make gas amplification, and the charge is read out independently by an electrodes. Figure 2.4 shows the schematic drawings of the GEM set up. The region between the drift plane and the GEM is called the drift region, and the region between the GEM and the readout electrodes is called the induction region. Figure 2.5 shows the electric field of GEM. By applying a large potential difference between the electrodes on both sides, a high electric field is formed in the hole. The density of lines of electric force in the hole of the GEM is much larger than that of

the drift region and the induction region and the electrons in the hole cause avalanche of electrons. Multiple GEMs can be used stages, to obtain a large amplification factor in total while suppressing the risk of discharge by decreasing the amplification factor per a GEM. It can also be used with other detectors, which is a major advantage of the GEM.

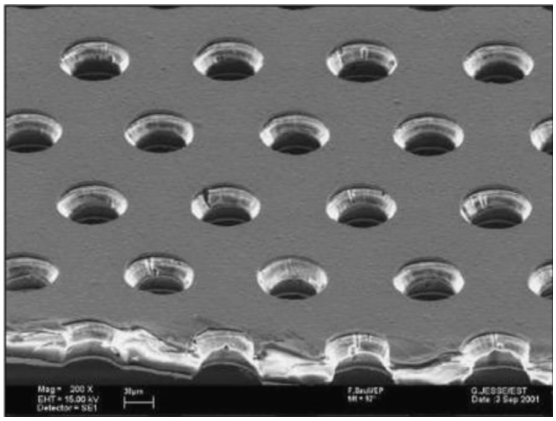

Figure 2.3: The microscopic photograph of the GEM[24].

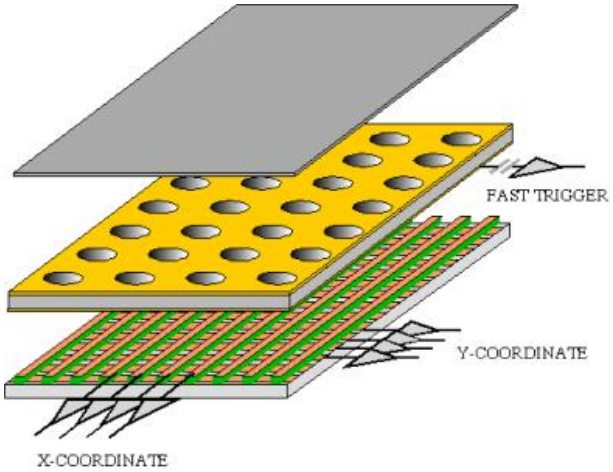

Figure 2.4: The schematic drawings of GEM set up[25]. The drift plane, GEM, read electrodes are set in this order from the top.

2.2.2 MicroMEGAS

MicroMEGAS (Micro-MEsh GAseous Structure) is an MPGD developed by Y. Geomataris in 1996[26]. The structure and operation principle are shown in Figure 2.6. A steel mesh separates the 5 mm drift region and the 128 µm amplification region. Readout electrodes for signal reading and pillars for supporting the mesh are arranged on PCB board. Primary electrons generated in the drift region are drifted to the mesh and then gas avalanche occur in the high electric field region between the mesh and the electrode substrate. The electric field of the drift region is several hundred V/cm, whereas the electric field of the amplification region is several tens of kV/cm which is about 100 times

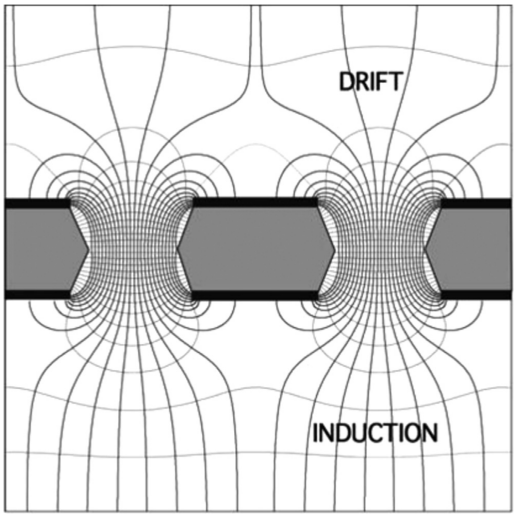

Figure 2.5: Electric field in the region of the holes of a GEM electrode[24].

the drift electric field, so that most electrons can pass through the mesh. Since the ions generated by the gas avalanche reach the mesh promptly, it can be used at an environment of a high particle-rate. There are several kinds of Micromegas.

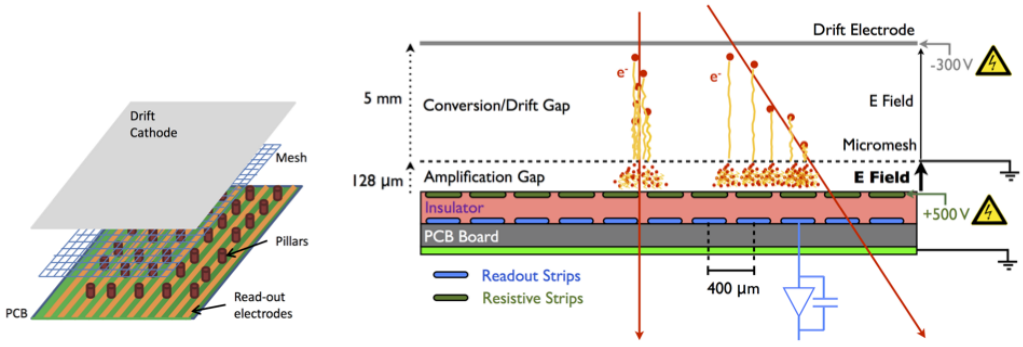

Figure 2.6: The structure of MicroMEGAS (left) and the operating principle image (right)[24].

2.2.3 μ-PIC

μ-PIC (micro PIxel Chamber) was developed by Tanimori and Ochi[27]. Figure 2.7 shows the structure of the μ-PIC. μ-PIC is installeat one end of a gas chamber. The plate-shaped electrode called drift electrode is install at the another end of the chamber. Anode pixels with a diameter of 50 µm are arranged in the form of pixels at a pitch of 400 µm on the insulating substrate of polyimide, and each anode pixel is surrounded by a cathode with a diameter of 250 µm. The anode pixel penetrates the insulator and is connected to the anode strip on the back side. The cathode electrodes are connected in strips one by one, and two-dimensional readout of signals can be realized with the structure in which the anode and the cathode strip are arranged crossing each other. When the μ-PIC is operated, a negative voltage is applied to the drift electrode, a positive voltage of several

hundred V is applied to the anode pixel, and the potential of the cathode is 0 V. In the vicinity of the anode, an electric avalanche occurs because a strong electric field is formed by the voltage applied between the anode and the cathode. Electrons generated by the avalanche of electrons are drifted to the anode and ions toward the cathode.

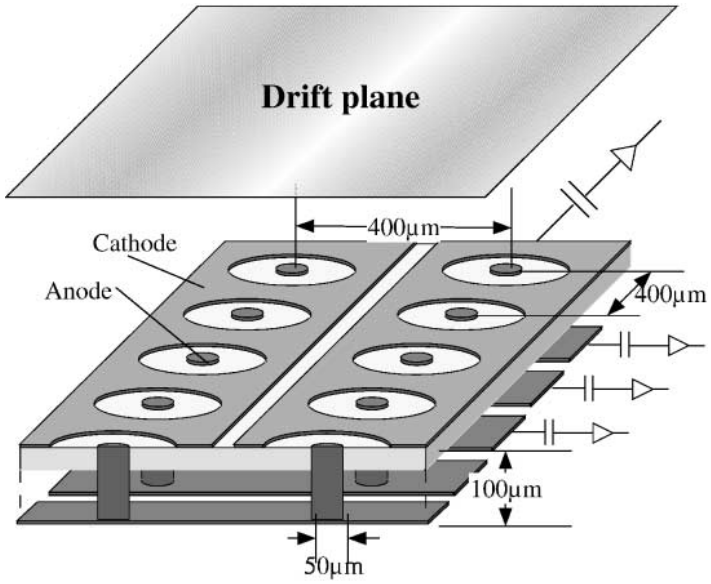

Figure 2.7: The schematic structure of the μ-PIC. Anode strips are formed through the substrate with a pitch of 400 µm[27]

2.3 Background of MPGD

Radioactive isotopes can be contaminated in the detector materials. They become serious background sources.

There are U series which decay series from ^{238}U to stable ^{206}Pb and Th series which decay series from ^{232}Th to stable ^{208}Pb in the typical background. The decay chains of ^{238}U and ^{232}Th(U/Th) series are shown in Figure 2.8. The half-lives of ^{238}U and ^{232}Th are 4.468×10^9 years and 1.405×10^{10} years, respectively, which are very long. ^{238}U and ^{232}Th are natural radio isotopes and are contaminated in various materials. The radioactive isotopes in the decay chains emit α-rays, β-rays and γ-rays of various energies. From the above, the background level in the dark matter search experiment is often discussed by the U/Th content.

The decay diagram of ^{40}K is shown in Figure 2.9. Since the half-life of ^{40}K is$1,277\times10^9$, it can be a background source. It is known that there are two types of decay in ^{40}K is, β decay and electron capture(EC).

Next, the background of MPGD is reviewed. MPGD is used for rare event searches. Therefore, the low background MPGD has been developed. A low background Micromegas was developed for the TREX-DM and its radioactivity was evaluated[28][29]. TREX-DM is a low-mass WIMPs search experiment using a gas TPC with a Micromegas. Table 2.1 summarizes the U/Th and ^{40}K content of the MPGD used in the rare event search experiments. The structure and measured sample of the microbulk Micromegas and the classical

Micromegas are shown in Figure 2.10. These were used in the CAST experiment. Since the microbulk Micromegas can provide large area at low cost by factory of manufacturing method and the microbulk Micromegas is potentially very clean, as the microbulk Micromegas is made from Kapton and copper, the microbulk Micromegas is used in rare event search experiment. From Table 2.1, the measurement result of the microbulk Micromegas,CAST of U/Th and ^{40}K. Since the original material of the sample part of the microbulk Micromegas, CAST was very radiopure, it is considered that radio isotopes were mixed from another layer(like epoxy) different from the sample part and chemical processing of the etching process. More detailed analysis was performed on ^{40}K, and it was found that the adhesive contained a large amount of ^{238}U and ^{40}K(Table 2.2)[30]. From the above, in order to fabricate a low background detector, it is necessary to pay attention not only to the material of the detector but also to processes and adhesives.

Table 2.1: ^{238}U, ^{232}Th and ^{40}K measurement results using the HPGe detector. The uncertainties listed are statistical errors.

Sample, Supplier	^{238}U [µBq/cm^2]	^{232}Th [µBq/cm^2]	^{40}K	Note
Classical Micromegas, CAST	< 40.3	4.6 ± 1.6	< 46	[28]
Microbulk Micromegas, CAST	26 ± 14	< 9.3	57 ± 25	[28]
Microbulk Micromegas, CERN	< 49	< 1.2	< 2.3	[29]
Kapton-copper foil	< 10.8	< 4.6	< 7.7	[28]
Copper-kapton-copper foil	< 10.8	< 4.6	< 7.7	[28]

Table 2.2: ^{238}U, ^{232}Th and ^{40}K measurement results using the HPGe detector. The uncertainties listed are statistical errors[30].

Sample	^{238}U [µBq/kg]	^{232}Th [µBq/kg]	^{40}K	Note
Stycast, Henkel	$(3.7 \pm 1.4) \times 10^3$	44 ± 12	$(0.32 \pm 0.11) \times 10^3$	Previous adhesive
Epoxy Hysol, Henkel	< 273	< 20	< 83	New adhesive

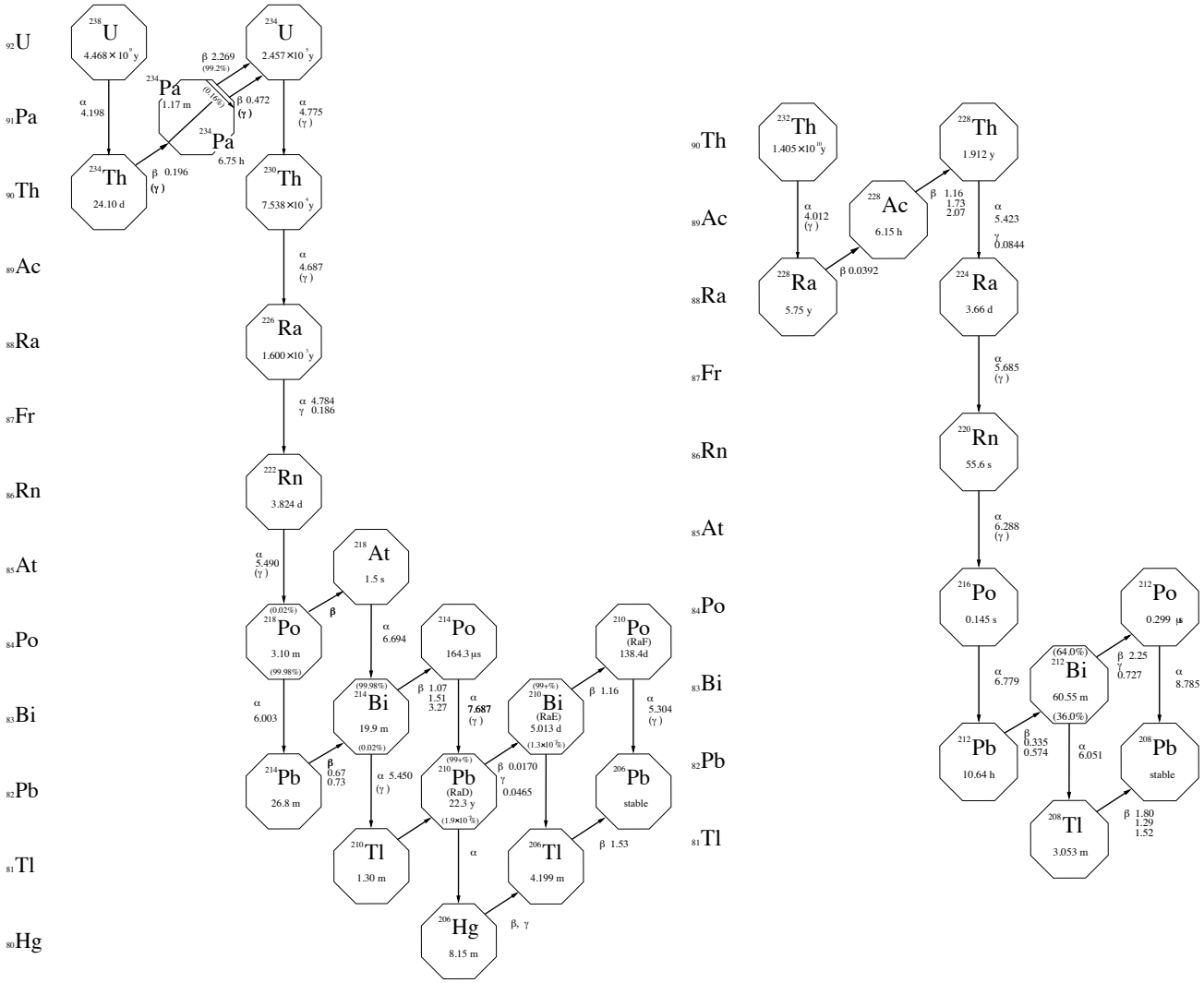

Figure 2.8: Decay chains of U series (left) and Th series (right)[31]. The whole chain of the U series is divided into three by relatively long-lived isotopes of ^{226}Ra and ^{210}Pb. They are defined as upper-stream, middle-stream and down-stream from the top of the chain.

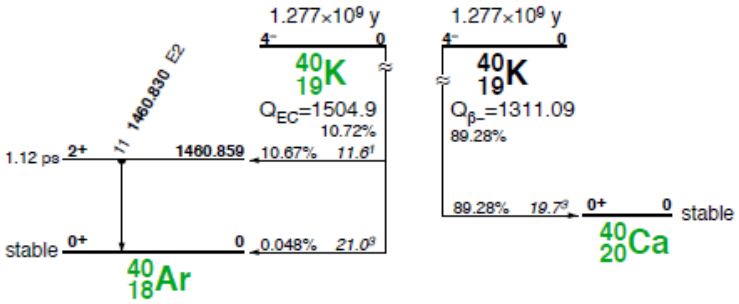

Figure 2.9: The decay diagram of ^{40}K[32].

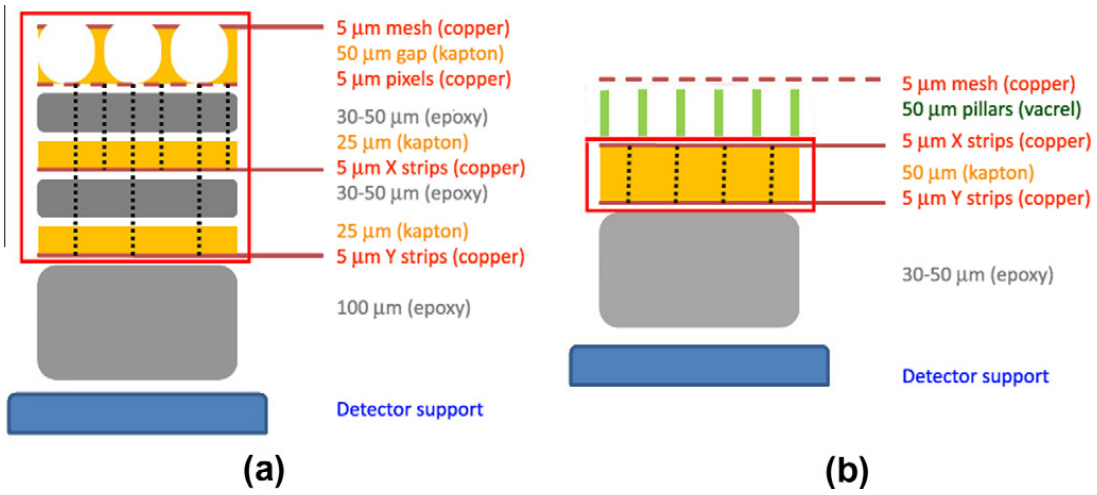

Figure 2.10: (a) is the structure of the microbulk Micromegas[28]. (b) is the structure of the classical Micromegas. The measured samples include only the components squared in red.

3 Background study on NEWAGE

NEWAGE(NEw generation WIMP search with an Advanced Gaseous tracker Experiment) is a direction sensitive dark matter experiment. As discussed in Section1.4.2, direction sensitive method would provide a convincing evidence of the dark matter. The NEWAGE detector uses a three-dimensional gaseous tracking detector " μ-TPC " read by a two-dimensional imaging detector μ-PIC which is a variation of MPGDs.

NEWAGE has the world's best sensitivity among the direction sensitive searches. However, the sensitivity is not good enough to reach the region where the detection of dark matter is indicated by DAMA and further sensitivity improvement is required. In this section, the previous work of NEWAGE is explained, and the method for improving the sensitivity to the DAMA region is discussed. Chapter 3.1, 3.2 and 3.3 are reviewing Ref.[33] and Chapter3.4 reviews Ref.[34]. Chapter 3.5 describes an original work of this thesis.

3.1 NEWAGE-0.3b'

In NEWAGE, a μ-TPC " NEWAGE-0.3b' " comprising of a drift region of 41 cm, a first-stage amplifier GEM of $32 \times 31\,\mathrm{cm}^2$ and a two-dimensional imaging detector μ-PIC of $30.72 \times 30.72\,\mathrm{cm}^2$ is used. NEWAGE-0.3b ' was installed in the Kamioka Underground labolatory in 2013[35]. The appearance of the detector system is shown in Figure 3.1, the schematic view of the μ-TPC is shown in Figure 3.2, and the internal structure is shown in Figure 3.3.

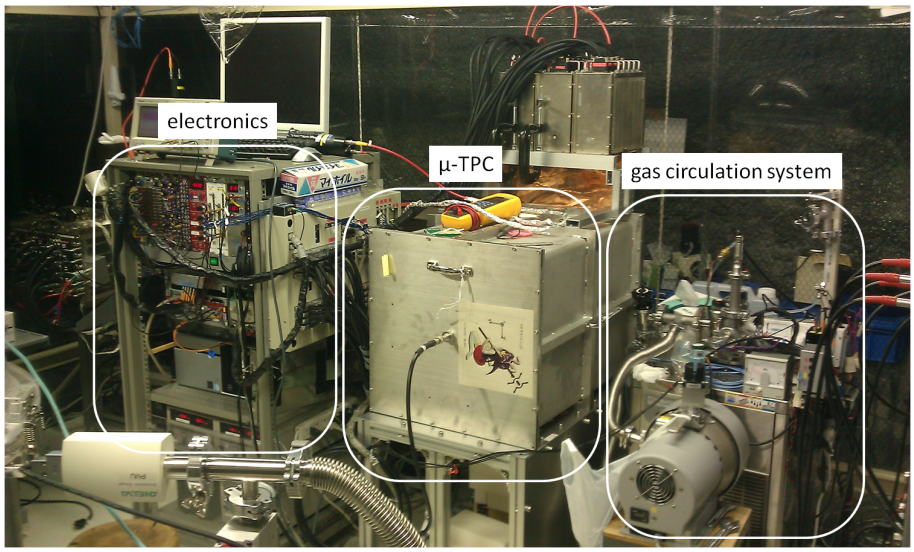

Figure 3.1: The photograph of whole system of the NEWAGE-0.3b' in the Kamioka underground laboratory[33]. In the figure, " electronics " shows the readout electronics, " μ-TPC " is NEWAGE-0.3b' , " gas circulation system " is a device to circulate for a gas purification.

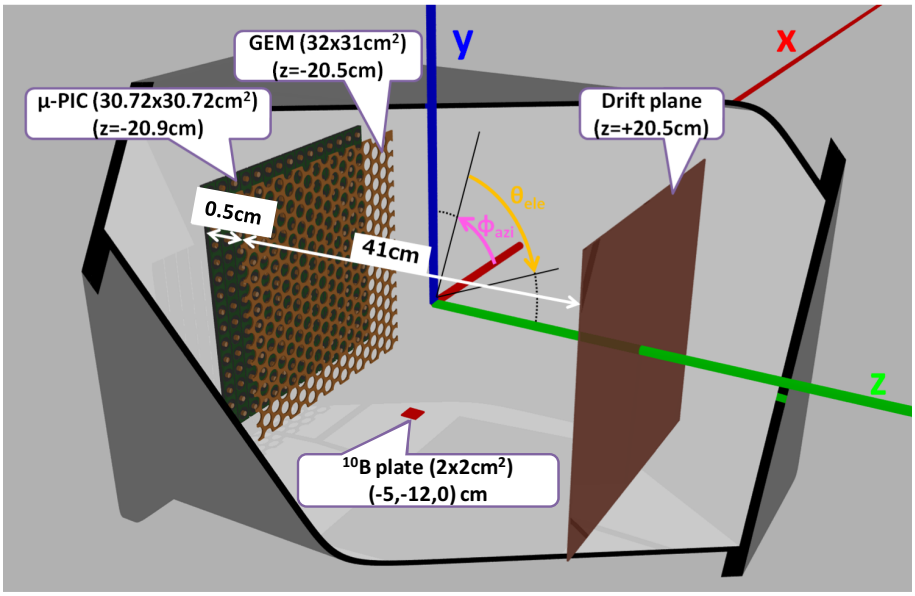

Figure 3.2: The schematic drawings of the NEWAGE-0.3b'. The red, blue and green lines are x, y, and z axes, respectively, and the center of the TPC is the origin $(0, 0, 0)$.

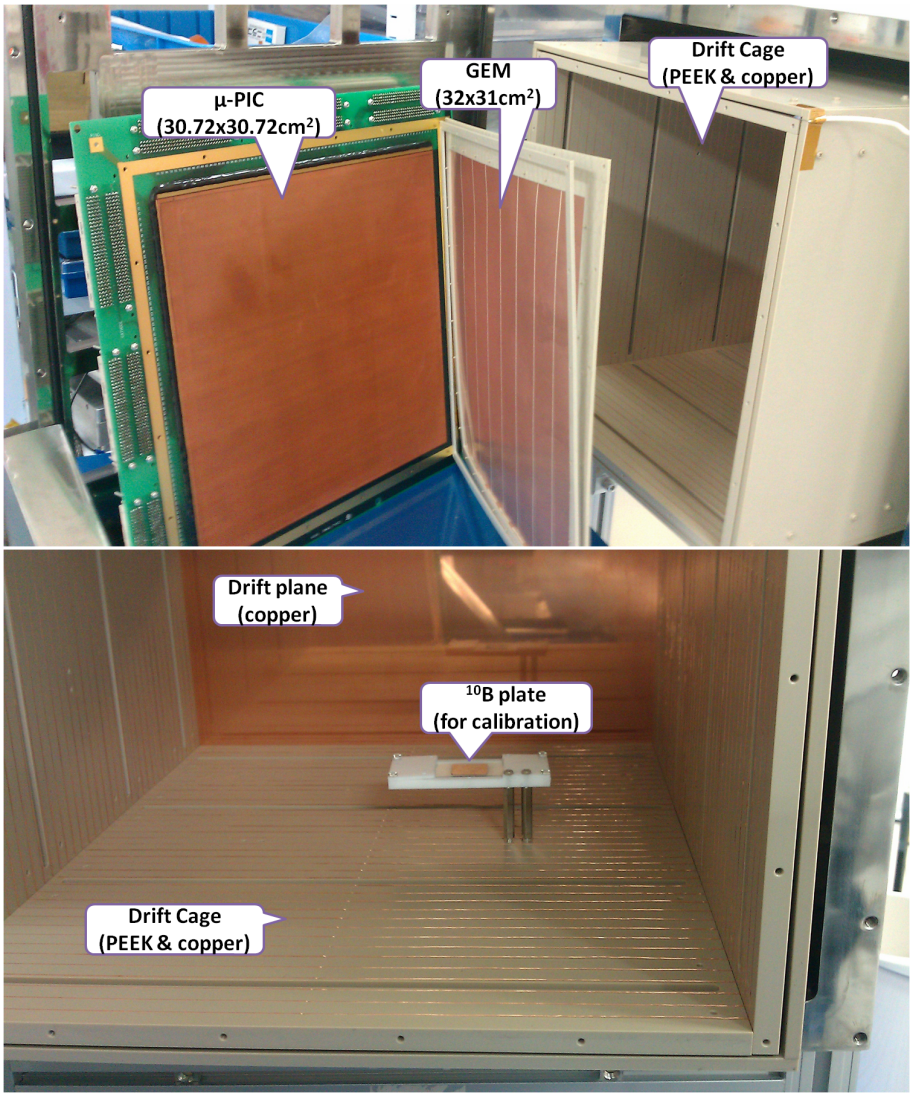

Figure 3.3: $30.72 \times 30.72\,\mathrm{cm}^2$ two-dimensional imaging detector μ-PIC installed in NEWAGE-0.3b' and the first-stage amplifier GEM of $32 \times 31\,\mathrm{cm}^2$(upper). The figure below shows the electric-field forming cage and the glass plate on which ^{10}B is vapor deposited[33].

Figure 3.4 shows pictures and a schematic drawing of the μ-PIC. The detail of the μ-PIC was stated in Chapter 2.2.3. The μ-PIC is a detector made by the printed circuit board processing technology and is used for gas amplification and charge reading. The printed circuit board processing technology is capable of making large detectors at a reasonable cost, which is an advantage in fabricating detectors used for the dark matter search requiring a large mass. Gas gain can be increased by supplying higher voltage to the anode electrodes with a risk of discharges and it is important to operate at a safe voltage in a dark matter run which requires a long-term stable measurement.

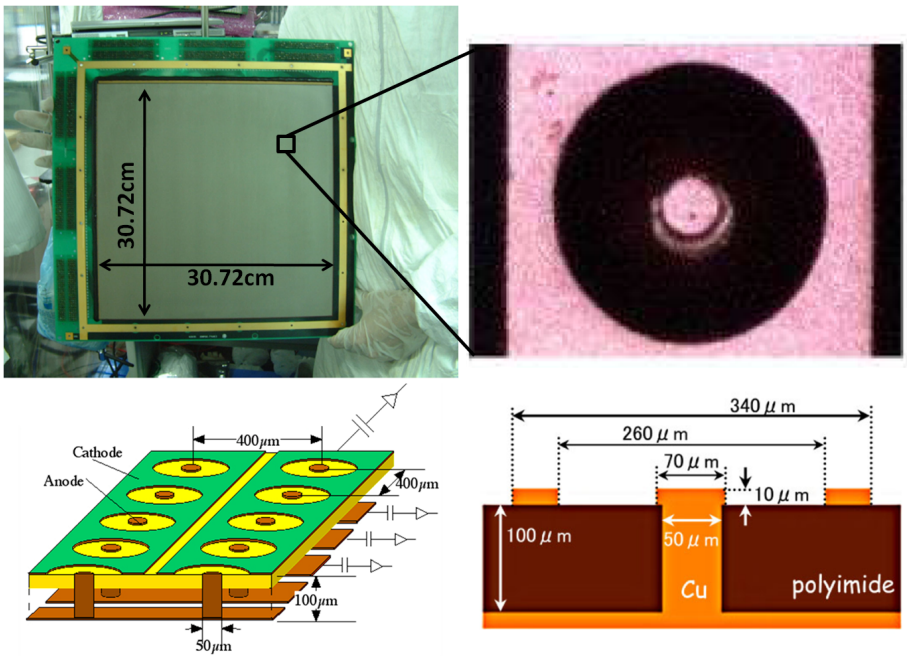

Figure 3.4: The photograph of μ-PIC (left top) and the enlarged photograph by microscope (right top). The left down figure shows the schematic view of a μ-PIC. The right down figure shows the cross-sectional view of the μ-PIC structure[33].

A GEM manufactured by Scienergy Co. is used as a first-stage amplifier to help the stable operations of the μ-PIC in low-pressure gas. A schematic view of the GEM is shown in Figure 3.5. GEM has 5 µm-thick copper electrodes formed on the both sides of a liquid crystal polymer (LCP) with a thickness of 100 µm. Holes with a diameter of 70 µm are made with a pitch 140 µm. By applying a voltage difference to the copper electrodes on both sides and creating a high electric field, the electrons are amplified by the gas avalanche. In the NEWAGE-0.3b', a GEM is installed at a distance of 5 mm from the μ-PIC.

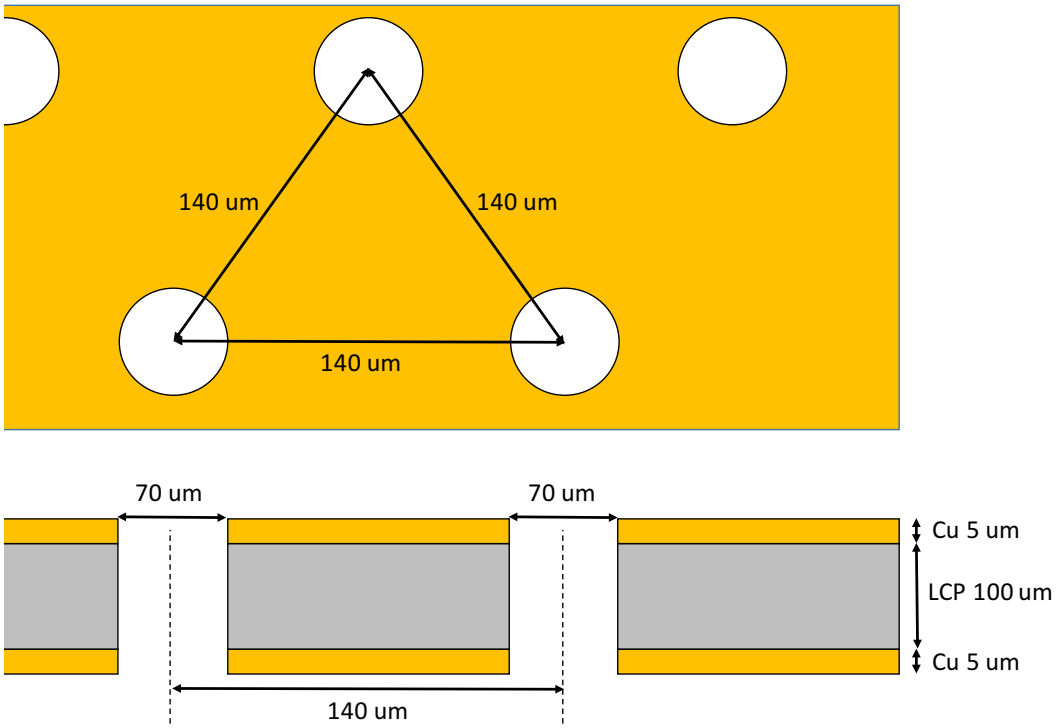

Figure 3.5: The schematic view of GEM.

CF_4 gas is used in NEWAGE from the point that the electron diffusion is small and the scattering cross section for the SD reaction of a fluorine is relatively large. In order to detect the track of nuclear recoil events of the low energy, the pressure is set at 0.1 pressure (76 Torr).

3.1.1 Data acquisition system (DAQ)

The signal read by the μ-PIC is processed by a dedicated data acquisition system (DAQ) shown in Figure 3.6. The charges from 756 anode electrodes and 756 cathode electrodes are processed by ASD (Amplifier-Shaper-Discriminator) chips, and then recorded as the " charge information " (analogSUM in Figure 3.6) and " tracking information " (LVDS in Figure 3.6). For the " charge information ", waveforms obtained by summing up the waveforms of 768 analog outputs of the cathode side ASD to 4 lines are recorded using a 100 MHz Flash ADC (FADC). The energy is know from the waveform.

There are so-called " self trigger mode " (self TRIG in Figure 3.6) and " external trigger mode" (ext TRIG in Figure 3.6) for the DAQ trigger mode. In the self-trigger mode, 768 anode strips of μ-PIC are grouped into 16 channels and a trigger is issued when a hit comes to any of them. In the self trigger mode, since the trigger information corresponding to the actual event time in the μ-TPC can not be obtained, the information in the Z direction is the relative length of the Z component. Absolute position information in the Z direction can not be obtained in the self trigger mode. This mode is used for most of the measurements including the dark matter run. Only the self-trigger mode was used for the measurements discussed in this thesis.

The time-over-threshold (TOT) of corresponding strips are recorded the " track information ". Here, the conceptual diagram of the TOT is shown in Figure 3.7. The TOT

is the duration time that the waveform exceeds the threshold. The length in the drift direction per a clock can be calculated with the drift velocity (about 9 cm/µs) and the system clock (10 ns). An event sample is shown in Figure 3.8. TOT has a correlation with the energy deposit on each strip.

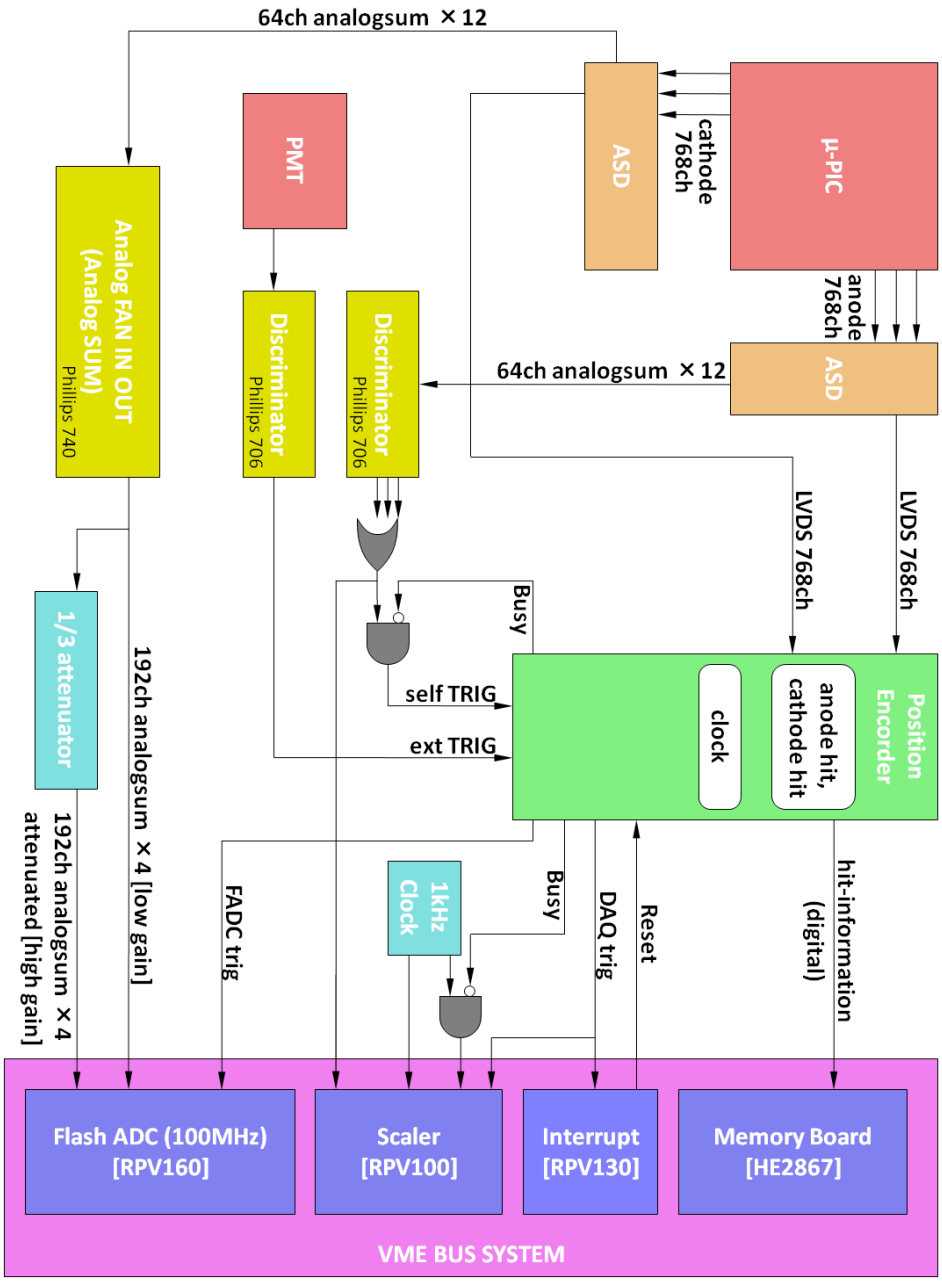

Figure 3.6: Data acquisition system (DAQ) of the NEWAGE-0.3b' detector[33].

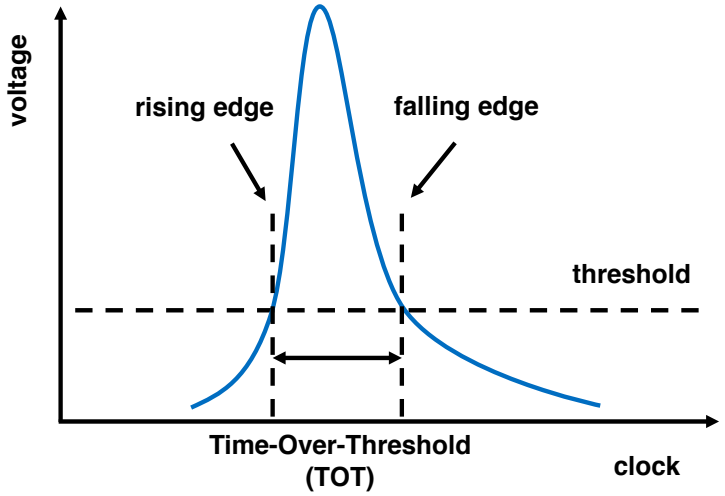

Figure 3.7: The schematic image of time-over-threshold (TOT)[36]. The blue line shows the waveform of a strip.

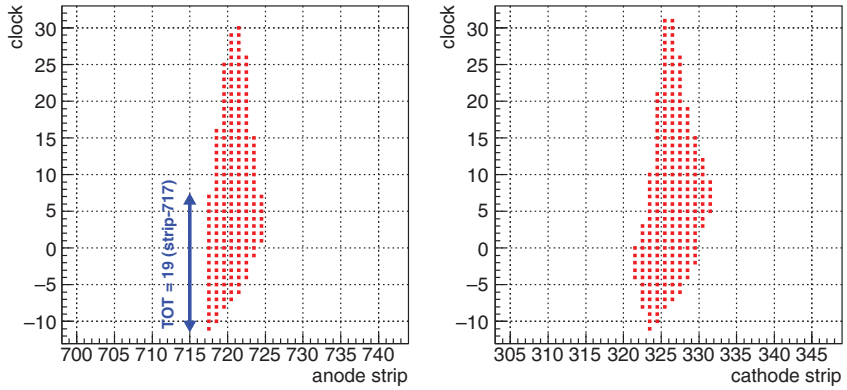

Figure 3.8: An α-ray event sample[35]. The left figure shows a track information in the (z-x) plane and the right figure shows that in the (z-y) plane. The allow in the figure indicates TOT of a strip.

3.1.2 Event selection

Several stages of event selections are applied to the data to discriminate various background events from nuclear recoil events. A fiducial volume of $28 \times 24 \times 41\,\mathrm{cm}^3$ is defined in the detection volume of $30.72 \times 30.72 \times 41\,\mathrm{cm}^3$. This is to remove the electrons and nuclear tracks from the field-cage walls. The energy cut is introduced to select the low energy region near the threshold(50 keV). The threshold is determined by the energy that can acquire sufficient track-length of the nuclear recoil event.

Three kinds of cuts to mainly remove the γ-ray backgrounds are applied. The cut parameters are "track-length", "TOT-sum" and "roundness". These three types of cuts are based on the fact that the energy deposition per a unit length of electrons is smaller than that of the nucleus. Figure 3.9 shows an example of a nuclear recoil event using a ^{252}Cf source that survived three cuts, Figure 3.10 shows an example of an event of electric

recoil removed by the track-length cut, Figure 3.11 shows an example of an electric recoil event removed by the TOT-sum cut and Figure 3.12 shows an example of an electric recoil removed by the roundness-cut. We used a ^{252}Cf source for the generation of nuclear and electric recoil events and a ^{137}Cs source for the generation of purely electric recoil events. The track-length means the detected track length. Electric recoil events can be discriminated because they are longer than the nucleus recoil events. TOT-sum is the sum of TOT of hit strips. TOT has correlation with energy deposit, and the TOT increases as the energy deposition. Roundness is defined as Eq.3.1.

$$\text{roundness}_{\text{x}} = \frac{\sum^{N_{\text{x}}}(z_{\text{risex}} - a_{\text{x}}x - b_{\text{x}})^2}{N_{\text{x}}}, \qquad \text{roundness}_{\text{y}} = \frac{\sum^{N_{\text{y}}}(z_{\text{risey}} - a_{\text{y}}y - b_{\text{y}})^2}{N_{\text{y}}},$$
$$\text{roundness} = min(\text{roundness}_{\text{x}}, \text{roundness}_{\text{y}}), \tag{3.1}$$

where, N_{x} and N_{y} are the number of hits on the x and y strips, z_{risex} and z_{risey} are the samallest-z corresponding the blue points shown in Figure 3.9, 3.10, 3.11, 3.12, (a_{x},b_{x}) and (a_{y},b_{y}) are the best fit values in the linear fit for (x, z_{risex}) and (y, z_{risey}), respectively. Nuclear recoil events have larger roundness than the electronic recoil events do. The electric recoil events are discriminated by these selections.

The cut parameters for selecting the nuclear recoil events are summarized below[33].

- **Fiducial-cut** : -14 [cm] < X < 14[cm], -10 [cm] < Y < 14[cm]

- **Energy-cut** : 50 [keV] < Energy < 400[keV]

- **length-cut** : track-length[cm] < 0.6 + 0.004 × E[keV]
  The long track events are removed (example : Figure 3.10[33]).

- **TOT-sum-cut** : TOT-sum> 100
  Small ToT-sum small events are removed (example : Figure 3.11[33])

- **roundness-cut** : roundness > 0.05
  The event that the rise point of z are close to a straight lines are removed (example : Figure 3.12[33]).

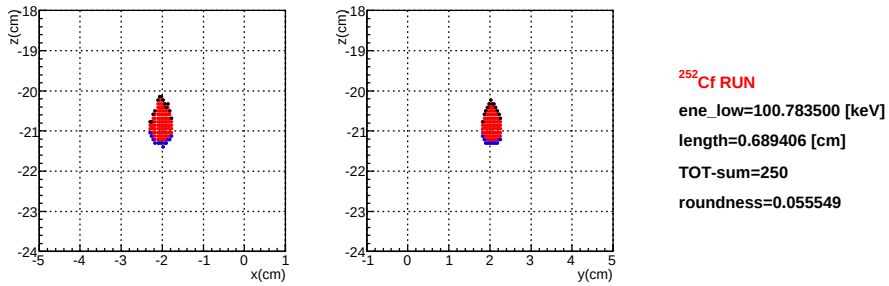

Figure 3.9: An event example that survived three cuts in ^{252}Cf source run[33]. The left figure shows the $x-z$ plane, the right figure shows the $y-z$ plane. Blue point and black point represent the rising and the falling points, respectively.

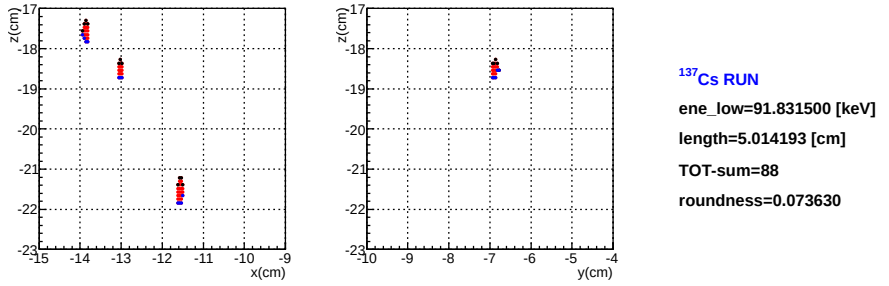

Figure 3.10: Track sample measured with a ^{137}Cs source, cut by the length-cut[33].

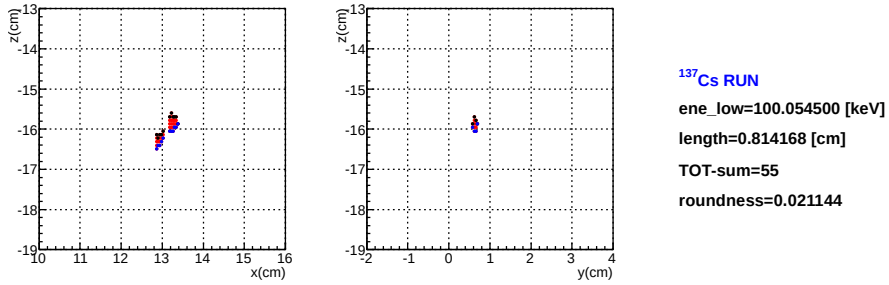

Figure 3.11: Track sample measured with a ^{137}Cs source, cut by the TOT-sum cut[33].

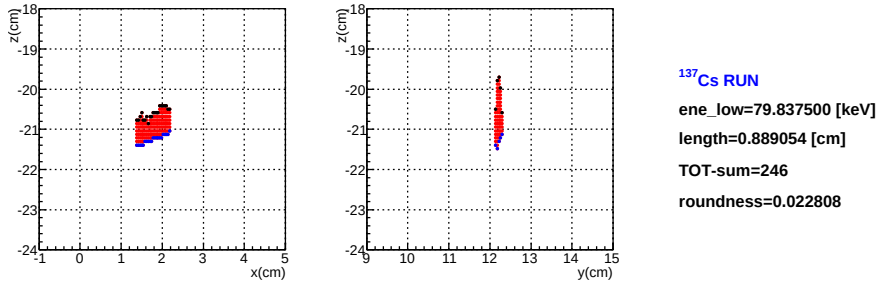

Figure 3.12: Track sample measured with a ^{137}Cs source, cut by the roundness-cut[33].

It is difficult to measure the absolute coordinate in the z direction for the events taken

with the self trigger mode in dark matter search. However, it is known that roundness which is one of γ-ray cut parameters is related to the absolute coordinate in z. Figure 3.13 shows the roundness dependence on the drift distance measured with the external trigger mode. The roundness has a weak correlation with the drift distance(z in Figure 3.13). However, the quantitative evaluation of the cut efficiency with respect to the drift distance is not known. In this thesis, the roundness cut was not applied the background study since the background around the μ-PIC needs to be studied.

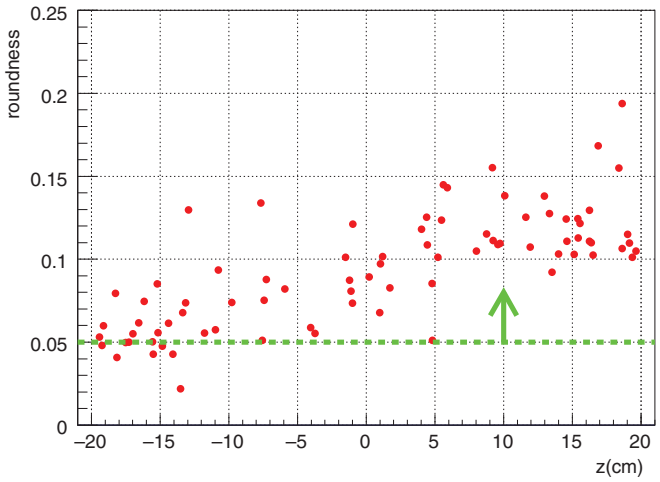

Figure 3.13: The relation between measured roundness and drift distance[35]。

3.2 Preceding dark matter search with NEWAGE-0.3b'

The dark matter search with the NEWAGE-0.3b' was conducted at the Kamioka Underground laboratory in 2013. The measurement details are summarized in Table 3.1. Figure 3.14 shows the results. The red line shows the result using the direction sensitive method, and the blue dotted line shows the conventional method using the energy spectrum only. The thin red line is the measurement results with NEWAGE-0.3a which is a preceding detector (" NEWAGE surface run " in Figure 3.14), and the result in Kamioka(" NEWAGE2010(RUN5) " in Figure 3.14). The measurement in 2013 marked the best direction-sensitive limits[33](" THIS WORK(RUN14) " in Figure 3.14), while the limit was far worse and does not reach the region where the presence of dark matter is suggested(" DAMA allowed " in Figure 3.14) and a further sensitivity improvement was required. The sensitivity of RUN14 was limited by the background events, not the statistics. Understanding and reducing of the background was necessary. The aim of this study is to improve the sensitivity to the DAMA region as a consequence of understanding and reducing the background.

RUN ID	gas filling	period	live time	mass	exposure
RUN14-1	2013/07/17	2013/7/20 − 8/11	17.1 days	10.36 g	0.177 kg · days
RUN14-2	2013/10/17	2013/10/19 − 11/12	14.5 days	10.36 g	0.150 kg · days
RUN14			31.6 days		0.327 kg · days

Table 3.1: Conditions of underground measurement RUN14.

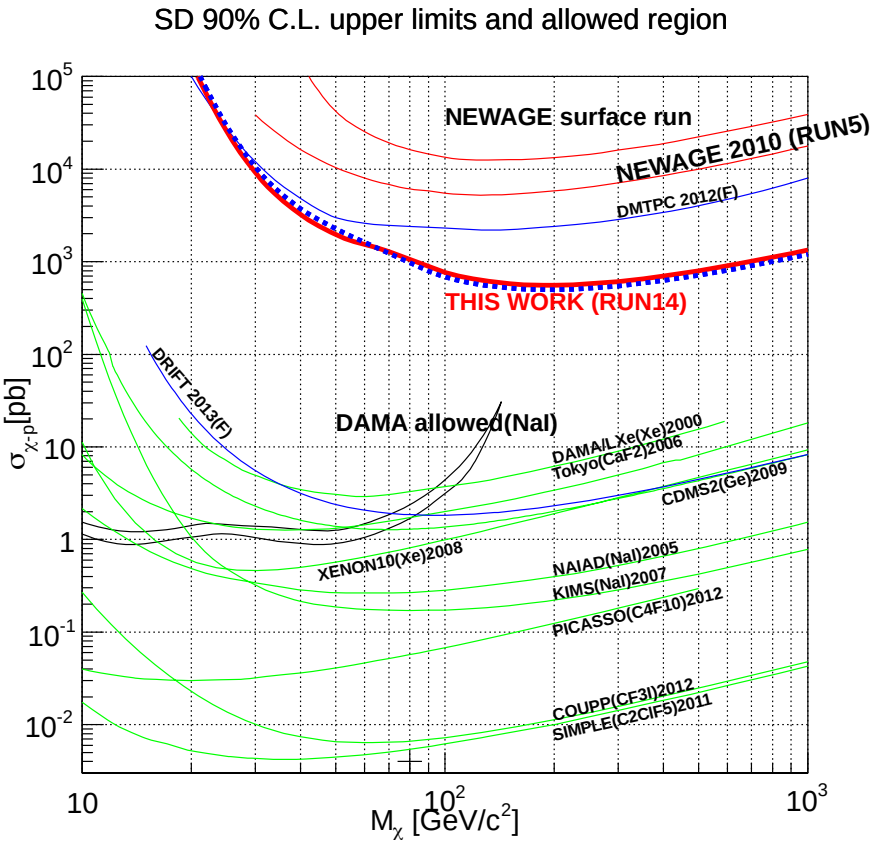

Figure 3.14: Search results of dark matter so far in NEWAGE[35](NEWAGE surface run, NEWAGE 2010, This work(RUN14)). The horizontal axis shows the mass of WIMP, and the vertical axis shows the scattering cross section in the SD reaction of protons and WIMP. THIS WORK(RUN14) is the limit obtained by the measurement in 2013.

3.3 Background study : possible sources

Understanding and reducing the background was necessary to improve the sensitivity. This subsection discusses the background understanding. Possible background candidates are illustrated in Figure 3.15. A is an ambient radiation event. B and B' are the α-ray events from the radon in the gas region. C and C' are U/Th(the uranium-238 and thorium-232) chain α-ray events in the μ-PIC components. " ' " means the events whose energy depositions are not amplified by the GEM. A region where energy depositions are not amplified by the GEM is defined as a gap region("gap" in Figure 3.15) and a region where energy depositions are amplified by the GEM is defined as a TPC region("TPC"

in Figure 3.15).

The ambient radiation includes the ambient γ-rays and the ambient neutron radiations. The ambient radiation was quantitatively understood by previous studies[33]. The background energy spectrum due to the ambient γ-rays from U/Th and ^{40}K in the rock was estimated taking account of the γ-ray rejection efficiency. The background energy spectrum due to the ambient neutron was evaluated. Their expected energy spectra are shown in Figure 3.16. For the 50 - 60 keV bin, the energy spectra predicted from the ambient radiation(" Environment gamma-rays " and " Environment neutrons " in Figure 3.15) are more than one orders of magnitude smaller than the measured energy spectrum(" RUN-14 (with all cuts) " in Figure 3.15). Therefore, it was understood that the ambient radiations were not the main background source.

α-ray backgrounds from the radon(^{220}Rn and ^{222}Rn) were investigated. α-rays from the radon usually have kinetic energies of several MeV, but they can be low energy background events if they hit the detector material before depositing all the energy they have. The radon concentration in the detector gas was know from the 6 MeV peak study[33]. The results can be interpreted with 14.0 [mBq/m^3] of ^{220}Rn or 9.3 [mBq/m^3] of ^{222}Rn. The energy spectra by α-rays from the radon predicted by the simulation are shown in Figure 3.17. For the 50 - 60 keV bin, the energy spectra from the radon(" ^{220}Rn in gas 14.0 [mBq/m^3] " and " ^{222}Rn in gas 9.3 [mBq/m^3] " in Figure 3.17) are more than three orders of magnitude smaller than the measured energy spectrum("RUN-14(without roundness-cut)" in Figure 3.17). Therefore, it was understood that they are not the main background sources.

Previous studies suggested that α-rays in the detector component from U/Th was the main background. In this study, the U/Th content in the detector was measured and their effects were quantitatively discussed.

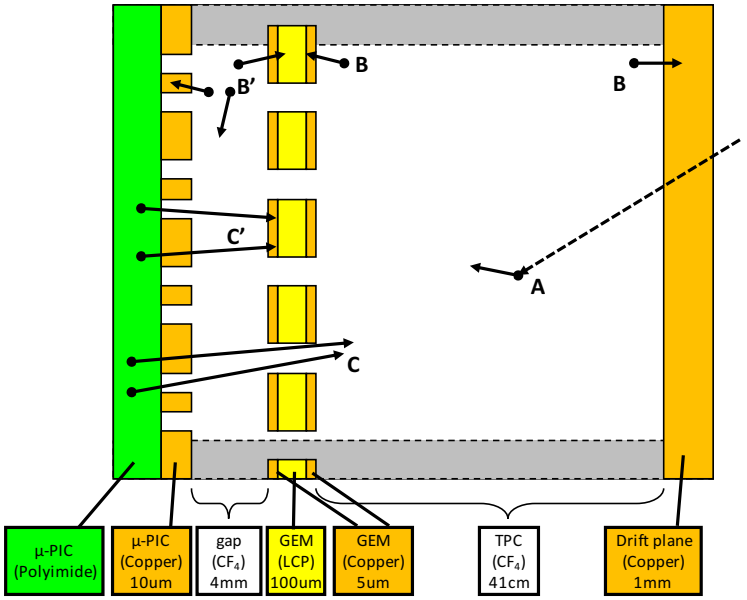

Figure 3.15: The schematic view of background candidates. A is ambient radiation event. B and B' are the α-ray events from the radon in the gas region. C and C' are α-ray events from U/Th chain in μ-PIC components. " ' " indicates the events whose energy depositions are not amplified by the GEM.

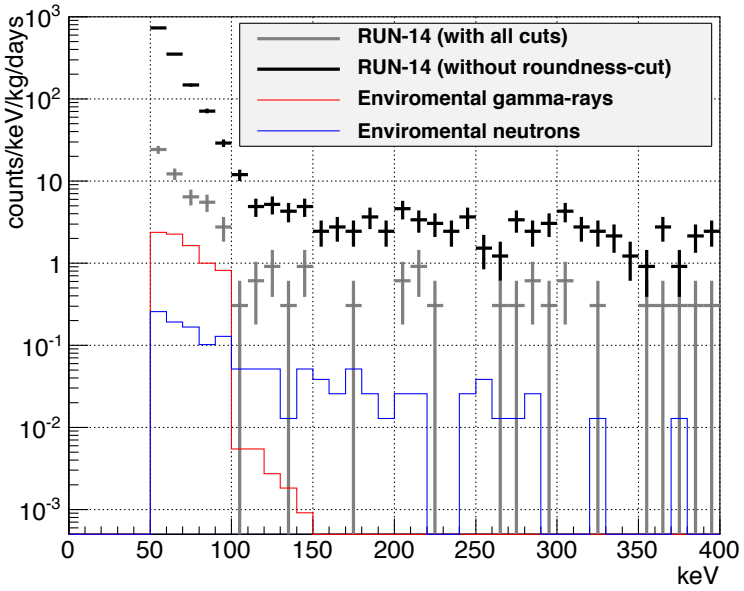

Figure 3.16: The energy spectra of RUN-14 and the estimated ambient backgrounds[33]. The gray cross is NEWAGE2015(RUN14) with the all cuts. The black cross is NEWAGE2015(RUN14) without the roundness cut. The red line shows an expected energy spectrum by the ambient γ-ray. The blue line shows an expected energy spectrum by the ambient neutron.

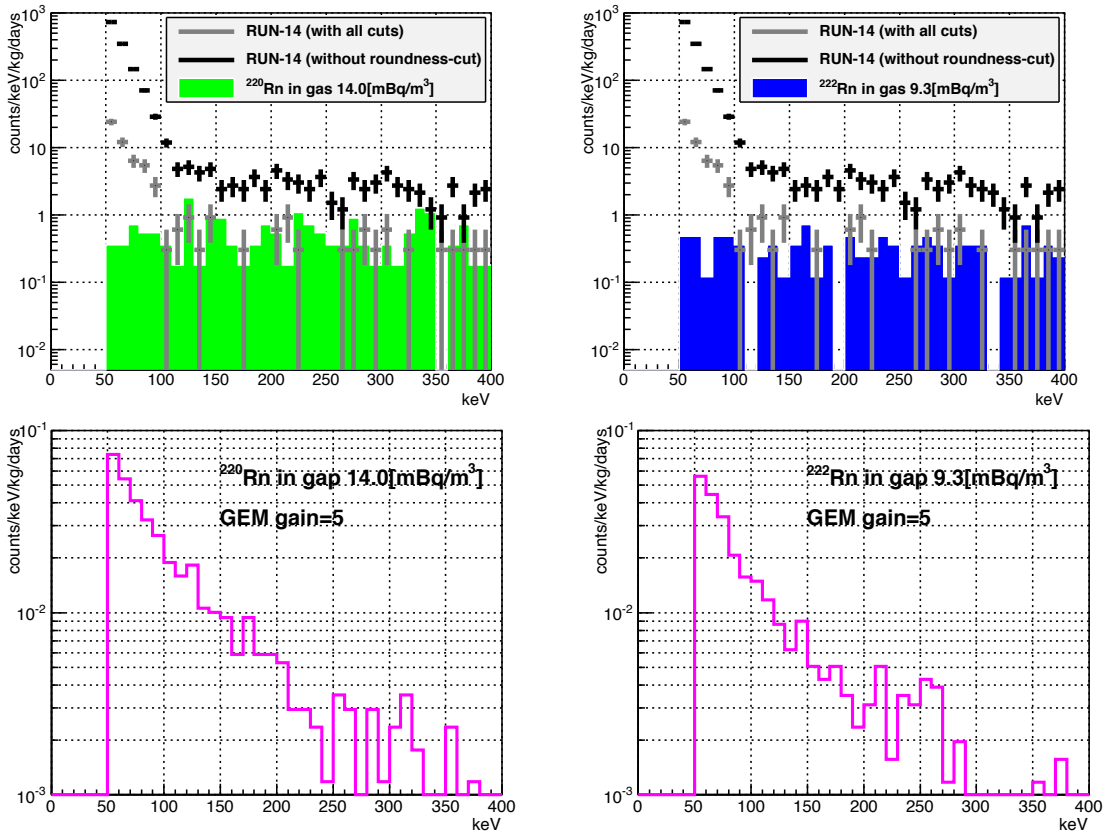

Figure 3.17: The energy spectra of the α-ray events from radon(^{220}Rn and ^{222}Rn)[33]. The black cross is NEWAGE2015(RUN14) without roundness cut. The gray cross is NEWAGE2015(RUN14) with all cuts. The estimated energy spectra of the α-ray backgrounds from ^{220}Rn (left) and ^{222}Rn (right) in the detection volume. The upper figure shows the α-ray events whose energy depositions are amplified by the GEM, and the lower figure shows the α-ray events whose energy depositions are not amplified by the GEM.

3.4 Background study : The measurement of the radioactive contaminations

This chapter reviews Ref[34] which is the author's master thesis. In this section, the α-ray background events from the U/Th contamination of the detector components are discussed. Therefore, U/Th contaminations of each component of the NEWAGE-0.3b' detector were measured. α-rays in the U/Th chains can be one of the main backgrounds since they are nuclear tracks and hard to be rejected by the event selections. It is important to know the distribution of U/Th in the detector is in order to understand and reduce the background and improve the sensitivity.

3.4.1 High Purity Germanium(HPGe) detector

HPGe (High Purity Germanium) detector which is one of the γ ray detectors was used to measurement of U/Th contaminations. The HPGe detector is a semiconductor detector using a high purity Ge crystals. The HPGe detector has a high energy resolution

and they are suitable for a precise measurement of the U/Th contamination.

Figure 3.18 shows the layout of the HPGe detector used in this study. It was located on the 1st basement of the University of Tokyo Hongo Campus Faculty of Science No.1 Building. The Ge crystal had a diameter of 57.1 mm, a length of 54.6 mm, a volume of 134 cm^3. The energy resolution was about 2 keV full-width at the half maximum (FWHM). In order to shield γ rays and β rays from the outside, 15 cm of lead and 7.5 cm of oxygen free copper are used as a shield. In order to reduce the noise generated by thermal excitation of electrons, the Ge crystal is cooled to 77 K by liquid nitrogen. A cold finger is used so as not to lose the shielding effect of the radiation.

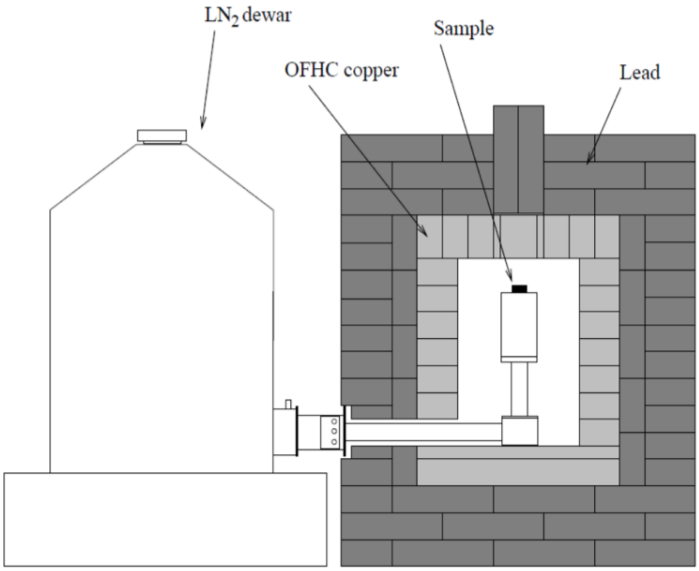

Figure 3.18: The layout of the HPGe detector. " Lead " and " OFHC copper " are used as outer and inner shields for shielding against the external γ-rays and β-rays.

3.4.2 Sample measurement

Figure 3.19 shows the μ-PIC structural diagram and the measured sample. μ-PIC has a base structure made of a polyimide (PI) with a thickness of 800 µm (" B " part in the μ-PIC sectional view in Figure 3.19) sandwiched by two layers of PI with a thickness of 100 µm (" A " parts in the μ-PIC cross section in Figure 3.19). Each part of the μ-PIC, namely 800 µm part, 100 µm part, and plating solution for electrode formation, the glass cloth used as a reinforcing material in the PI 100 µm part and PI 800 µm part were measured with the HPGe detector. The whole piece of the μ-PIC was also measured. PI containing glass cloth, will be expressed as PI(w/GC) in the following discussions. The glass cloth sheet of the reinforcing material was taken out from the PI(w/GC)100 µm part by dissolving the polyimide using NaOH and KOH solutions. The glass cloth sheet was also measured. The thickness of glass cloth sheets taken out from the PI(w/GC)100 µm part were measured with a micrometer. The thickness t of the glass fiber was 87 ± 6 µm where the error is the standard deviation of the thickness of the twelve sheets. The PI(w/GC) of the 800 µm part could not be dissolved. Although it was impossible to know

the details of PI(w/GC) 800 µm part, it was confirmed that several sheets of glass cloth were used in one layer of PI(w/GC) 800 µm. The GEM, placed directly above μ-PIC in the NEWAGE-0.3b' detector, was also measured because it becomes a serious background source even with a small amount of radioactive impurities. Table 3.2 shows the geometry, mass, and measurement period and efficiencies of the HPGe detector for the measurement samples.

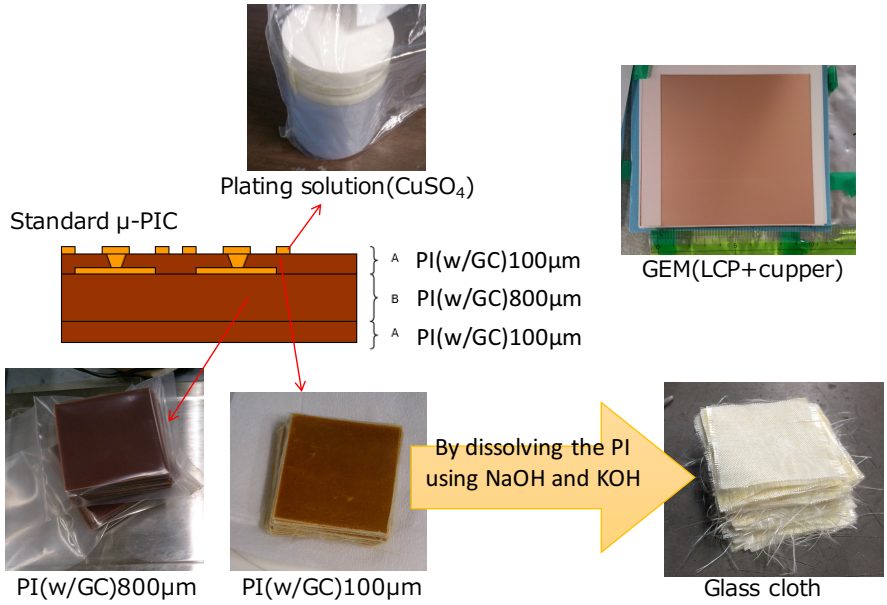

Figure 3.19: The μ-PIC structure diagram and measured samples.

Table 3.2: The details of measurement sample and γ-ray detection efficiencies for the each energies of interests.

	measurement	sample		efficiency [%]		
Sample	Period[day]	Mass[g]	Geometory[cm^3]	93 keV	583 keV	609 keV
μ-PIC	12.85	169.5	$5 \times 5 \times 2.47$	13.8	4.50	4.36
PI(w/GC) 800 µmpart	8.67	134	$5 \times 5 \times 2.88$	8.51	2.94	2.82
PI(w/GC) 100 µmpart	6.75	35	$5 \times 5 \times 0.98$	13.8	4.50	4.36
Plating solution[1]	5.92	72	$\phi 5 \times 3.3$	6.98	3.03	2.90
Glass cloth	22.67	15	$5 \times 5 \times 0.76$	14.0	4.51	4.50
GEM	6.17	27	$5 \times 5 \times 0.40$	14.2	5.31	4.97

3.4.3 Data analysis

γ-rays emitted from radioactive impurities contained in the sample were detected with the HPGe detector. The isotope species were identified by their energy and their amounts were known from the count rate, detection efficiencies and branching ratios. Figure 3.20 shows the energy spectrum obtained for the μ-PIC with an HPGe detector. The blue line shows the spectrum measured with the sample and the red line shows the

[1]The aqueous solution of copper sulfate

background spectrum measured without the sample. Several peaks from the U/Th series were observed. Peaks for the analysis of U/Th components were selected based on the condition that there was no peak from other nuclides nearby and the condition that the decay branching ratio was large so that the peaks are clearly obtainable. In this study, radioactivities of the upstream of the U series, the middle of the U series, and the Th series are obtained from the peak of 93 keV from the ^{234}Th decay, the peak of 609 keV from the decay of the ^{214}Bi and the peak of 583 keV from the decay of the ^{208}Tl, respectively. Table 3.3 summarizes the details of the isotopes of interest. $B_{\rm i}$ is the decay branching ratio. As mentioned in the section 2.3, there is a possibility that the radiative equilibrium is not established in the U series. The radiative equilibrium was checked for the U series by comparing the upstream and the middle-stream results.

Table 3.3: Nuclide used in U/Th content measurement

Nuclide	series	γ-ray energy [keV]	$B_{\rm i}$ [%]
^{234}Th	U upper stream	93	5.4
^{214}Bi	U middle stream	609	46.1
^{208}Tl	Th	583	84.5

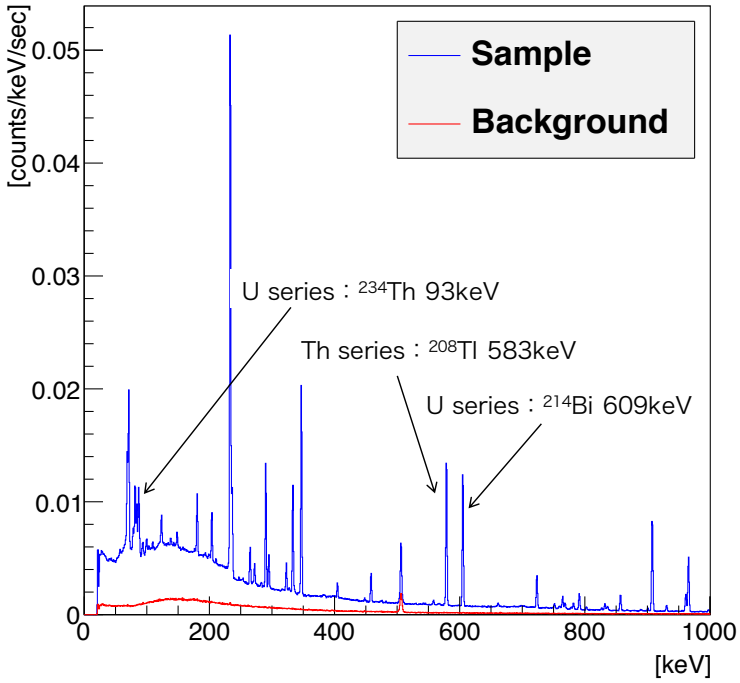

Figure 3.20: Energy spectra for the μ-PIC and background obtained with the HPGe detector.

The background is subtracted from the measurement data of the sample to obtain the net spectrum. An example of the net spectrum is shown in Figure 3.21. The net peak is then fitted with a Gaussian distribution and the peak count rate S [counts/sec] was obtained from the area. Here, in order to eliminate continuous components due to

Compton scattering of the higher energy γ-rays, the peak was fitted with Eq.3.2 which takes account of the constant term.

$$f(x) = a \exp\left\{-\frac{(x-b)^2}{2\sigma^2}\right\} + d, \tag{3.2}$$

where, a and d were treated as free parameters. b and σ were fixed with the corresponding energies and the energy resolution of 1 keV, respectively. Here, the count rate S [counts/sec] is given by

$$S = \sqrt{2\pi} a \sigma. \tag{3.3}$$

Next, the radioactivities of the isotopes were determined. When a certain isotope($=i$) gives a peak, the radioactivity $R_{\rm i}$ [counts/sec](= [Bq]) is known as follows.

$$R_{\rm i} = \frac{S}{B_{\rm i} \times \varepsilon_{\rm i}}, \tag{3.4}$$

where, $B_{\rm i}$ is the decay branching ratio which gives the corresponding peak, and $\varepsilon_{\rm i}$ is the γ-ray detection efficiency by the HPGe detector. The decay branching ratios of the peak used for determining the content are as shown in Table 3.3. The detection efficiency depends on the materials and the geometries of the samples. The detection efficiencies were obtained using Monte Carlo simulation, Geant4. Geant4 is a C ++ based software tool kit that simulates the reaction between radiation and matter. Table 3.2 summarizes the γ-ray detection efficiency for each energy in the measurement sample. The lower the γ-ray energy, the higher the reaction rate in the Ge crystal and the higher the detection efficiency. In addition, it was found that gamma rays are likely to rearch Ge crystals and the detection efficiency is higher when the measurement sample is smaller.

Finally, U/Th contaminations X [g/g] were calculated. When a radiation equilibrium is established, R can be regarded as radioactivity of the parents of the U/Th series, and U/Th content X [g/g] can be obtained as follows

$$X = \frac{1}{M_s}\frac{A}{N_A} N_0, \tag{3.5}$$

$$N_0 = \frac{R}{\lambda}, \tag{3.6}$$

$$\lambda = \frac{\ln 2}{T_{1/2}}, \tag{3.7}$$

where M_s is the mass of the sample, A is the atomic number, N_A is Avogadro's number, N_0 is the number of atoms, λ is the decay constant, and $T_{1/2}$ is the half-life of the parent of the decay series.

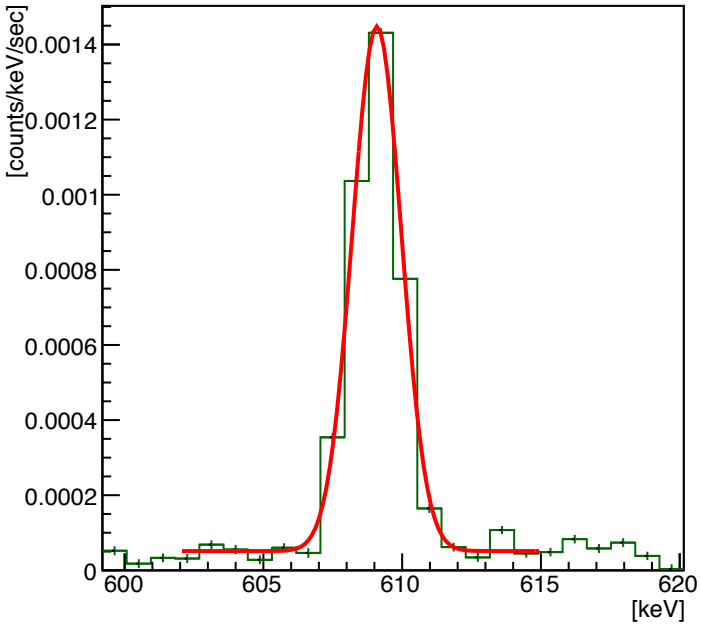

Figure 3.21: An examples of an peak of the net spectrum. The peak was fitted with a Gaussian distribution. The error shows the statistical error.

The background may be larger than the signal of the sample due to the statistical fluctuation. In this case, an upper limit value based on the Bayesian principle was given. The Bayesian principle introduces the prior probability and reflects it on the posterior probability. The prior probability $P(\mu)$ for the expectation value μ of the expected count rate was defined as Eq.3.8

$$P(\mu) = \begin{cases} 0 : \mu < 0 \\ 1 : \mu \geq 0 \end{cases} \tag{3.8}$$

This means that when $\mu \geq 0$, it has physical meaning, and when $\mu < 0$, it means that there is no physical meaning. Figure 3.22 shows a case where the background count was subtracted from the sample and the peak count rate became negative. An upper limit value giving a confidence level of 90% in the positive range was calculated in these cases.

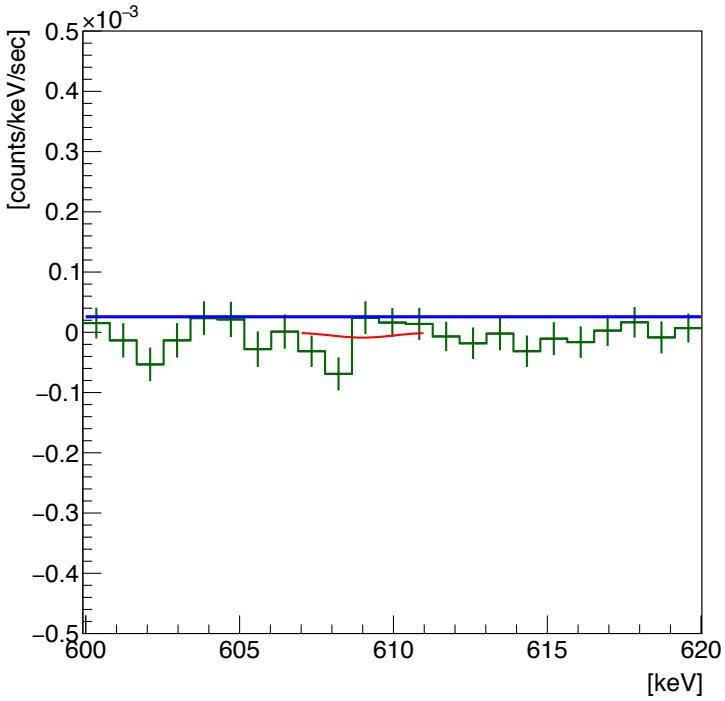

Figure 3.22: An example where the background was larger than the signal of the sample. The error shows statistical error. The blue line was the upper limit obtained by the Bayesian based on the fit result.

3.4.4 Result of U/Th contamination measurement

The measurement results of ^{238}U and ^{232}Th contaminations by the HPGe detector are shown in Table 3.4. From the measurement, it was found that the whole μ-PIC and related materials of PI(w/GC)800 µm part, PI(w/GC)100 µm part and the glass cloth were known to contain non-zero amounts of ^{238}U and ^{232}Th. It was found that the plating solution (aqueous solution of copper sulfate) and GEM was 5% or less of the μ-PIC radiation level. Since these may become background sources in the future, they need to be measured with more sensitive HPGe. The glass cloth is used as a reinforcing material of PI. One sheet of glass cloth was used for one PI(w/GC)100 µm part. Here, in order to consider the radioactivity in the PI(w/GC)100 µm part, Table 3.5 shows the radioactivity per unit area for the PI(w/GC)100 µm part and one glass sheet each. The U/Th contents of the glass cloth were found to be smaller than the PI(w/GC)100 µm part by about 10%. This result suggested that either U/Th were washed out during the taking-out the glass cloth from the PI(w/GC)100 µm part or U/Th were aloso contaminated in the polyimide part. The amount of U/Th contaminations in the PI(w/GC)100 µm part was considered to be explained by the glass cloth sheet. In the the discussion in the following sections, it is done using the value of PI(w/GC)100 µm part.

Table 3.4: The U/Th contaminations. The error takes into account only the statistical error.

Sample	^{238}Umiddle stream [10^{-6} g/g]	^{238}Uupper stream [10^{-6} g/g]	^{232}Th [10^{-6} g/g]
μ-PIC	1.17 ± 0.01	1.14 ± 0.01	5.84 ± 0.03
PI(w/GC)800 µmpart	0.78 ± 0.01	0.76 ± 0.01	3.42 ± 0.03
PI(w/GC)100 µmpart	0.39 ± 0.01	0.38 ± 0.01	1.81 ± 0.04
Plating solution[1]	< 0.01	< 0.13	< 0.06
Glass cloth	0.84 ± 0.03	0.91 ± 0.02	3.48 ± 0.12
GEM	< 0.02	< 0.17	< 0.12

Table 3.5: The U/Th contaminations per one sheet. The error takes account of only the statistical error.

Sample	^{238}Umiddle-stream [µBq/cm^2]	^{238}Uupper-stream [µBq/cm^2]	^{232}Th [µBq/cm^2]
PI(w/GC)100 µmpart	68.5 ± 1.5	66.4 ± 2.5	102.1 ± 2.3
glass cloth	64.5 ± 0.8	71.3 ± 1.4	86.8 ± 1.1

3.5 Background understanding

It was found that a large amount of U/Th was contained in the glass cloth used for the reinforcement of the PI. In this section, based on the measurement results obtained in Section 3.4.4, α-rays' backgrounds are studied quantitatively by the simulation and are compared with the measured data.

3.5.1 Simulation

α-rays from the decay of the U/Th series in the PI lose some of their initial energies in the PI before reaching the gas volume. It is thus important to estimate the energies of the α-rays coming out of the PI. Figure 3.23 shows the calculation result of α-ray range in the PI as a function of the initial energy by SRIM (Stopping and Range of Ions in Matter)[37]. SRIM is a simulation software that calculates the range and energy deposit of ions as they pass through matters by a semi-empirical formula based on experimental values. Therefore, it can be judged that α-ray of 10 MeV does not pass through the PI of 90 µm or more. The maximum energy of α-rays from the U/Th series is 8.785 MeV. From this, it can be judged that α-rays in the PI(w/GC)800 µm part and the PI(w/GC)100 µm part on the far side from the detection volume need not to be considered as the background sources.

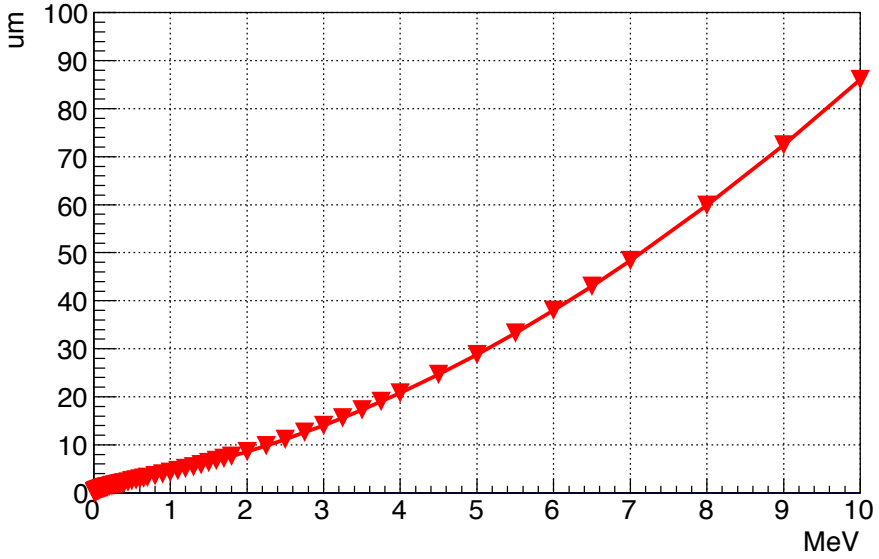

Figure 3.23: The simulation results by SRIM[33]. α-ray from U/Th series in PI has a kinetic energy of less than 8.785 MeV.

The simulation on the α-ray background was performed using Geant4[38]. The geometry of the detector in the simulation is shown Figure 3.24. The geometry of the PI(w/CG) 100 µm part was updated from Ref [34]. α-rays from U/Th series were generated from the orange mesh region of the PI(w/GC)100 µm part. For detailed understanding, the thickness of the glass sheet was measured using a micrometer. Measured thicknesses of the PI(w/CG) 100 µm part and the glass sheet were 90 µm and 87 $\pm$ 6 µm, respectively. The error is the standard deviation. 90 µm was used for the thickness of the PI(w/CG)100 µm part. The thickness of the glass sheet t was assumed to be 81 µm $< t <$ 90 µm with the PI(w/CG)100 µm thickness as the maximum. The α-ray events were classified into two types, those whose charges were amplified by GEM were defined as " TPC events " (C in Figure 3.24), and those whose charges were not amplified by the GEM was defined as " gap event " (C' in Figure 3.24). Since the gap events were not amplified by GEM, the charge detected by μ-PIC was smaller than the TPC event by a factor of GEM gain.

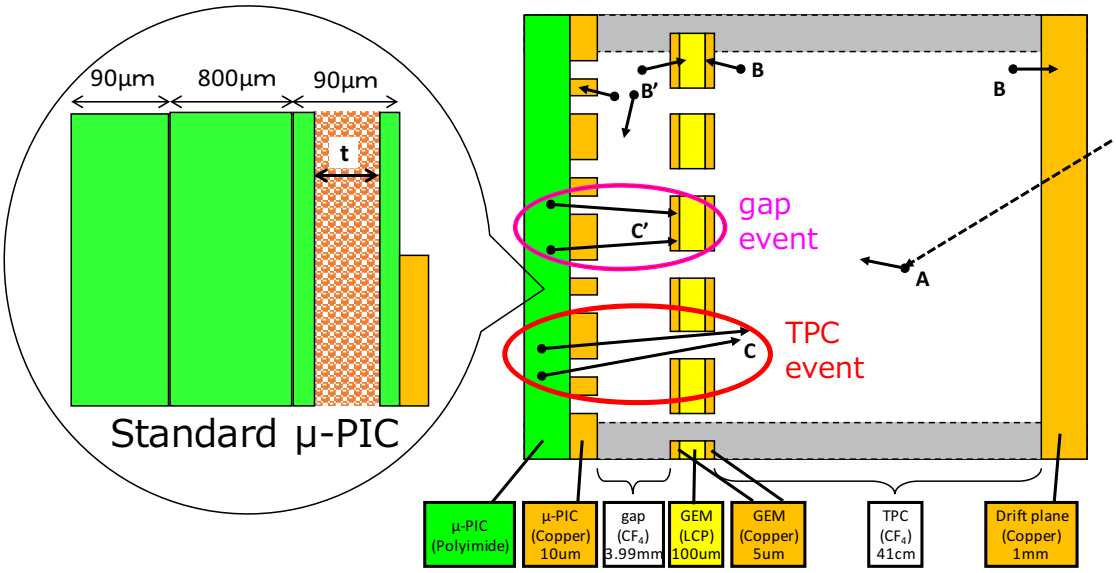

Figure 3.24: The geometry of the detector in the Geant4 simulation.

3.5.2 Simulation result

The simulation results are shown in Figure 3.25, Figure 3.26 and Figure 3.27. The black cross represents the measurement result in NEWAGE2015(RUN14) without the roundness cut. The red, green, and blue represent the results with different parameters. The gas gain of GEM($\equiv G_{\mathrm{GEM}}$) was assumed to be $7 < G_{\mathrm{GEM}} < 13$. Under the dark matter search condition, the gas gain of GEM and μ-PIC were not measured independently but only the combined total gain was measured. The gas gain of the GEM estimated from total gain and μ-PIC gain dependence of the anode voltage was about 10. The error for the GEM gain was estimated from the position dependence of the μ-PIC. The energy resolution was taken into account for the simulation. The energy resolution is sum of $\sigma_{\mathrm{uni}} = 20\%$ and $\sigma_{\mathrm{noise}} = 2$ keV[12]. Here σ_{uni} is the energy resolution estimated from the width of the radon peak and σ_{noise} is the energy resolution due to the electric noise. Since the energy depositions of the gap events have not $\times 10$ amplificated by the GEM, their energy depositions were interpreted $\times 1/10$ because the energies were defined for the TPC events. These gap events concentrated on the low energy side as shown in Figure 3.26 and Figure 3.27. Here, energy ranges of 50 - 150 keV and 150 - 400 keV were defined as " gap region " and " TPC region ", respectively.

The change in the energy spectrum of the TPC events due to the uncertainly of the thickness of the glass cloth is shown in Figure 3.25. The uncertainly of the glass cloth thickness t was $81\,\mu\mathrm{m} < t < 90\,\mu\mathrm{m}$. The average in the $150\,\mathrm{keV} - 400\,\mathrm{keV}$ energy range of RUN14 is 2.46 [counts/keV/kg/day]. The average in the $150\,\mathrm{keV} - 400\,\mathrm{keV}$ energy range of $81\,\mu\mathrm{m}$, $87\,\mu\mathrm{m}$ and $90\,\mu\mathrm{m}$ were 2.50, 2.50 and 3.16 [counts/keV/kg/day], respectively. The count rate of $1.02\ (+0.26 - 0.00)$ [counts/keV/kg/day] in the $150\,\mathrm{keV} - 400\,\mathrm{keV}$ energy range of RUN14 was over-explained. Here,the positive error represents that the thickness of the glass cloth is $90\,\mu\mathrm{m}$ and the negative error represents that the thickness of the glass cloth is $81\,\mu\mathrm{m}$ and $87\,\mu\mathrm{m}$.

The changes in the energy spectrum of the gap events due to the uncertainly of t are

shown in Figure 3.26. The rising component of the energy region of 50 keV − 150 keV is explained within the range of the uncertainly of the thickness of the glass cloth. The changes in the energy spectrum of the gap events due to the uncertainly of GEM gain are shown in Figure 3.27. The higher the assumed GEM gain was, the more the gap events were squeezed into the lower energy side. From Figure 3.26 and Figure 3.27, gap events from the U/Th series contained in the glass cloth in the PI(w/GC)100 µm part were found to explain the background near the threshold. This was the energy region limiting the detection sensitivity.

Since the background source limiting the detection sensitivity was in the PI(w/GC)100 µm part, it is important to understand the surface α-ray rate from the PI(w/GC)100 µm part. The surface α-ray rate was estimated using the measurement result of HPGe(Table 3.5). ^{238}U releases 8 α in its series decay. The α-ray rate from ^{238}U $R_{\mathrm{U}}[\alpha/\mathrm{cm}^2/\mathrm{h}]$ is calculated as follows

$$\begin{aligned} R_{\mathrm{U}}[\alpha/\mathrm{cm}^2/\mathrm{h}] &= (68.5 \pm 1.5)[\mu\mathrm{Bq}/\mathrm{cm}^2] \times 60 \times 60[\mathrm{sec/h}] \times 8\alpha \\ &= (1.97 \pm 0.04)[\alpha/\mathrm{cm}^2/\mathrm{h}] \end{aligned} \tag{3.9}$$

^{232}Th releases 6 α in its series decay. The α-ray rate from ^{232}Th $R_{\mathrm{Th}}[\alpha/\mathrm{cm}^2/\mathrm{h}]$ is calculated as follows

$$\begin{aligned} R_{\mathrm{Th}}[\alpha/\mathrm{cm}^2/\mathrm{h}] &= (102.1 \pm 1.5)[\mu\mathrm{Bq}/\mathrm{cm}^2] \times 60 \times 60[\mathrm{sec/h}] \times 6\alpha \\ &= (2.21 \pm 0.05)[\alpha/\mathrm{cm}^2/\mathrm{h}] \end{aligned} \tag{3.10}$$

The fractions of α-rays reaching the sensitive region were obtained from the simulation, $4.03^{+0.25}_{-0.47}$ % for ^{238}U and $5.19^{+0.28}_{-0.55}$ % for ^{232}Th. The error is the systematic error due to the glass cloth thickness. Considering this fraction, the surface α-ray rate expected from the standard μ-PIC is as follows

$$\begin{aligned} R_{\mathrm{HPGe}}[\alpha/\mathrm{cm}^2/\mathrm{h}] &= \{(1.97 \pm 0.04) \times (4.03^{+0.25}_{-0.47})\,\% + (2.21 \pm 0.05) \times (5.19^{+0.28}_{-0.55})\,\%\}[\alpha/\mathrm{cm}^2/\mathrm{h}] \\ &= (1.93 \pm 0.07) \times 10^{-1}[\alpha/\mathrm{cm}^2/\mathrm{h}] \end{aligned} \tag{3.11}$$

The α-ray detection efficiency of the gap and TPC region are defined as follows

$$\varepsilon_{\mathrm{gap}} = \frac{e_{\mathrm{gap}}}{T_{\mathrm{all}}}, \tag{3.12}$$

$$\varepsilon_{\mathrm{TPC}} = \frac{e_{\mathrm{TPC}}}{T_{\mathrm{all}}}, \tag{3.13}$$

where, e_{gap} and e_{TPC} are the number of α-ray events of gap region and TPC region in the simulation, respectively. T_{all} is the total number of α-ray events detected in the simulation. These were obtained as $\varepsilon_{\mathrm{gap}} = 1.77^{+3.24}_{-1.26} \times 10^{-2}$ and $\varepsilon_{\mathrm{TPC}} = 2.04^{+0.08}_{-0.28} \times 10^{-3}$, respectively. Therefore, the surface α-ray rate R_{gap} and R_{TPC} can be calculated as follows

$$R_{\mathrm{gap,RUN14}}[\alpha/\mathrm{cm}^2/\mathrm{h}] = \frac{I_{\mathrm{gap}}[\mathrm{count/kg/day}] \times mass[\mathrm{kg}]}{\varepsilon_{\mathrm{gap}} \times S[\mathrm{cm}^2]}, \tag{3.14}$$

$$R_{\mathrm{TPC,RUN14}}[\alpha/\mathrm{cm}^2/\mathrm{h}] = \frac{I_{\mathrm{TPC}}[\mathrm{count/kg/day}] \times mass[\mathrm{kg}]}{\varepsilon_{\mathrm{TPC}} \times S[\mathrm{cm}^2]}, \tag{3.15}$$

where, I_{gap} and I_{TPC} are the α rate per unit mass [kg] per unit time [day], " $mass$ " is the target mass(=10.36 [g]) and S is the fiducial area ($= 24 \times 28$ [cm^2]). The $R_{\mathrm{gap,RUN14}}$ and $R_{\mathrm{TPC,RUN14}}$ are the total flux of the surface α-ray from the PI(w/o GC)100 µm part estimated from the I_{gap} and I_{TPC}, respectively. From Eq.(3.14) and (3.15), the $R_{\mathrm{gap,RUN14}}$ and $R_{\mathrm{TPC,RUN14}}$ are $(5.0^{+12.5}_{-3.3}) \times 10^{-1}$ and $(1.9^{+0.3}_{-0.1}) \times 10^{-1}$ [α/cm^2/h].

It is summarized in the surface α-ray rate Table 3.6 obtained from each method. Each measured value of the surface α-ray rate obtained from the different method showed the consistent results. Since $R_{\mathrm{TPC,RUN14}}$ was more accurately measured than $R_{\mathrm{gap,RUN14}}$, $R_{\mathrm{TPC,RUN14}}$ was adopted and $R_{\mathrm{RUN14}} \equiv R_{\mathrm{TPC,RUN14}}$ was defined.

Table 3.6: The summary of the surface α-ray rate using the standard μ-PIC.

Method	[α/cm^2/h]
R_{HPGe}	$(1.9 \pm 0.1) \times 10^{-1}$
$R_{\mathrm{gap,RUN14}}$	$(5.0^{+12.5}_{-3.3}) \times 10^{-1}$
$R_{\mathrm{TPC,RUN14}}$	$(1.9^{+0.3}_{-0.1}) \times 10^{-1}$

The glass cloth in the PI(w/GC)100 µm part was found to be the main background source in the energy region relevant for the dark matter direct search experiment. Therefore, changing the PI(w/GC)100 µm part to a low background material was expected to increase the sensitivity. When the background is limiting the sensitivity, the detection sensitivity decreases, the sensitivity improves accordingly as long as the background limits the sensitivity. A goal of this study was set that the sensitivity would reach the DAMA region. The sensitivity of our goal is shown in Figure 3.29. In order to reach the DAMA region, it was necessary to improve the detection sensitivity by a factor of 50. Therefore, the requirement was to find a new material which had 50 times smaller amount of U/Th in the PI(w/GC)100 µm part and to create a new μ-PIC with it.

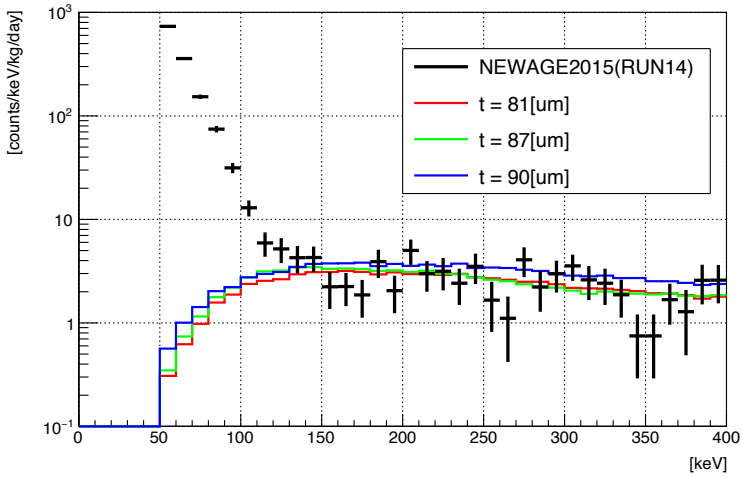

Figure 3.25: The changes of the energy spectrum of TPC events due to the uncertainly of the thickness of glass cloth in the PI(w/GC)100 µm. The red line shows the result when the thickness of the glass cloth was 81 µm, the green line shows the case when the thickness of the glass cloth was 87 µm, the blue line shows the result when the thickness of the glass cloth was 90 µm, the black cross is NEWAGE2015(RUN14) data without roundness cut.

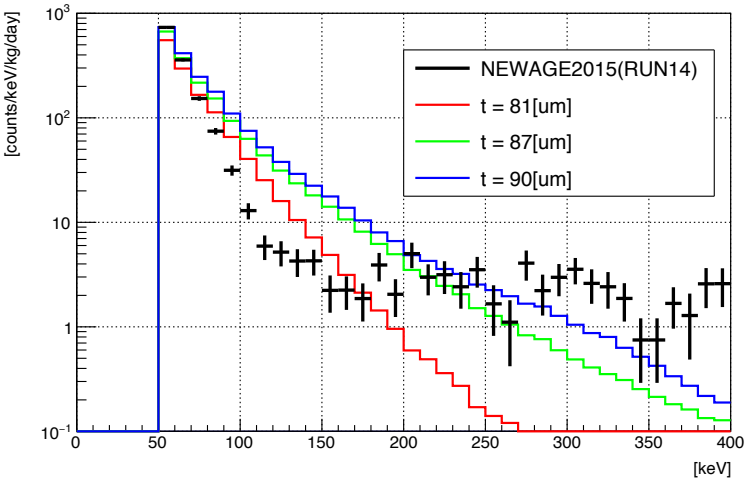

Figure 3.26: The change of the energy spectrum of the gap events due to the uncertainly of the thickness of the glass cloth in the PI(w/GC)100 µm part. The gas amplification of GEM was assumed to be 10. The red line shows the result when the thickness of the glass cloth was 81 µm, the green line shows the case when the thickness of the glass cloth was 87 µm, the blue line shows the result when the thickness of the glass cloth was 90 µm, the black cross was NEWAGE2015(RUN14) data without roundness cut.

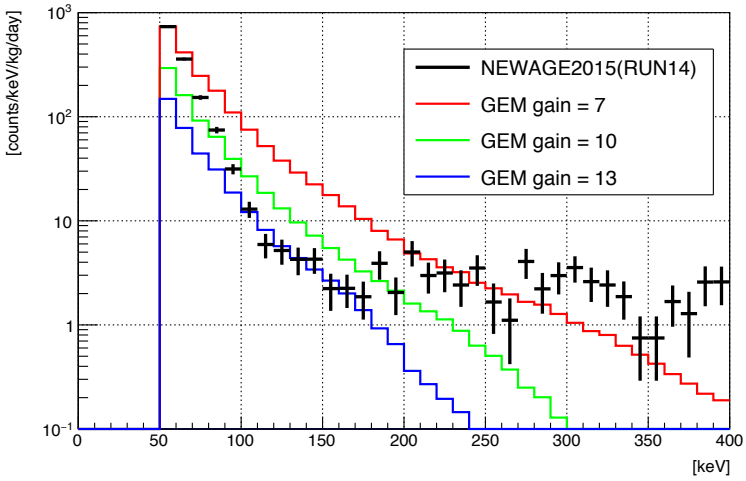

Figure 3.27: The change of the energy spectrum of the gap events due to the uncertainly of the GEM gain. The glass thickness was assumed to be 90 µm. The red line shows the result when the gas gain of GEM was assumed to be 7, the green line shows the case when the gas gain of GEM was assumed to be 10, the blue line shows the result when the gas gain of GEM was assumed to be 13, the black cross is NEWAGE2015(RUN14) data without roundness cut.

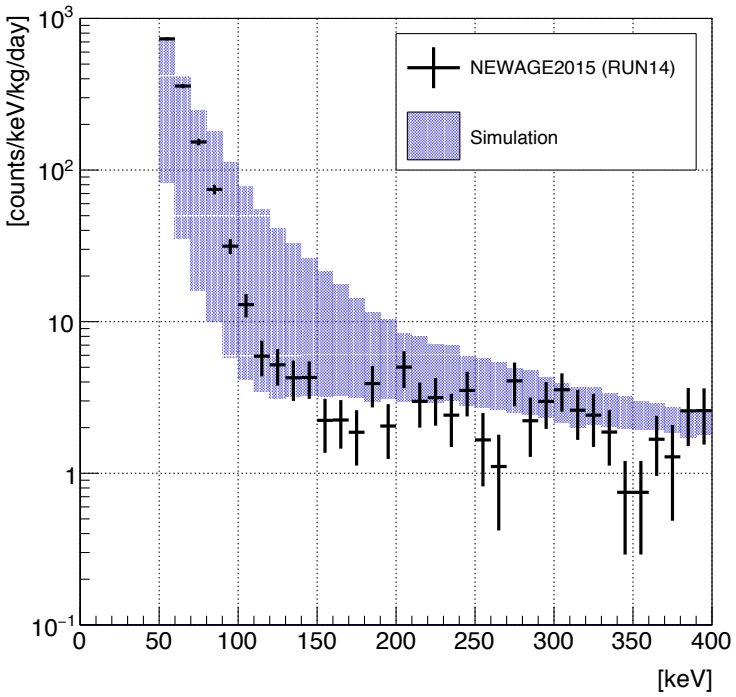

Figure 3.28: The comparison of the energy spectrum expected by simulation and the measurement by NEWAGE 2015(RUN14)[33]. The purple band is expected energy spectrum in the simulation and the black cross is NEWAGE2015(RUN14) without the roundness cut.

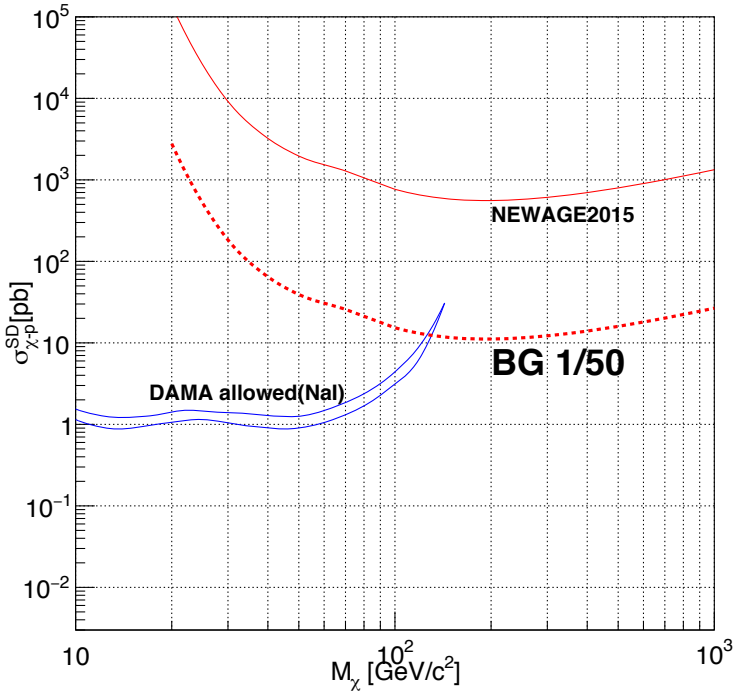

Figure 3.29: " NEWAGE2015 " is the current sensitivity. " BG 1/50 " is the sensitivity goal of this thesis. The horizontal axis shows the mass of the WIMP, and the vertical axis shows the scattering cross section in the SD interaction of protons and WIMP.

4 Development of Low-α μ-PIC

The discussion in the previous chapter indicated that the main background of NEWAGE was the gap events due to α-rays from the U/Th series contained in the glass cloth in the polyimide(PI) 100 µm part. Since α-rays were helium nuclei and were actually nuclear-track events, it was difficult to discriminate them analytically. Therefore, it was necessary to remove these background sources at a hardware level. From the above discussion, a μ-PIC using a material with a smaller amount of U/Th contamination was developed.

4.1 Material selection

A new material with a smaller amount of U/Th contamination was searched. The details were described in Ref [34]. In this chapter the content of Ref [34] is briefly reviewed.

In order to make a new μ-PIC whose α-ray emission is 1/50 of the standard μ-PIC, it was necessary to search for a material which contained 1/50 or less of U/Th than the PI(w/GC)100 µm part did. A material consisting of a layer of PI without glass cloth(=w/o GC) and a layer of epoxy was chosen as a new material candidate. It had a layered structure of 80 µm in total with PI(w/o GC) part of 5 µm and epoxy part of 75 µm. The picture of this material is shown in Figure 4.1 The material looks curled since there is no glass cloth of the reinforcing material. It would not be a problem for the fabrication, since it will be thermal-bonded to the PI(w/GC)800 µm part.

The amount of U/Th contaminations in this material was measured with an HPGe detector. For this sample measurement, HPGe detector of the Kamioka Observatory was used to measure the low level contamination of the U/Th. The background at 609 keV of the HPGe detector in the University of Tokyo Hongo campus was 576 counts/keV/kg/day, whereas that of HPGe detector in the Kamioka Observatory was 0.7 counts/keV/kg/day. Details and γ-ray detection efficiencies of this new material are summarized in Table 4.1 and measurement results are summarized in Table 4.2. The reason that the upper limit value of the U series upper stream is one order of magnitude higher than the U series middle stream is because the branching ratio of 609 keV(middle-stream) is 46.1 % and the branching ratio of 93 keV(upper stream) is 5.4 %. The new material was found to have U/Th content less than 1/50 of the current PI100 µm part. Since this new material satisfied the requirement, a new μ-PIC(Low-α μ-PIC) was manufactured by replacing the PI 100 µm part with this new material[34].

Figure 4.1: The new material candidate, polyimide without glass cloth(PI w/o GC) 5 µm and epoxy75 µm.

Table 4.1: The details of PI(w/o GC) + epoxy and γ ray detection efficiencies by energies of interests.

	measurement	sample		efficiency		
Sample	Measurement period[day]	Geometry [cm^3]	Mass[g]	93 keV[%]	583 keV[%]	609 keV[%]
PI(w/o GC) 5 µm+epoxy 75 µm	6.75	$5 \times 5 \times 0.86$	22.67	14.31	6.79	6.45

Table 4.2: The U/Th content in the new material.

Sample	^{238}Umiddle stream [10^{-6} g/g]	^{238}Uupper stream [10^{-6} g/g]	^{232}Th [10^{-6} g/g]	Note
PI(w/GC) 100 µm	$(3.9 \pm 0.1) \times 10^{-1}$	$(3.8 \pm 0.1) \times 10^{-1}$	1.81 ± 0.04	Current material
PI(w/o GC) 5 µm+epoxy 75 µm	$< 2.98 \times 10^{-3}$	$< 2.86 \times 10^{-2}$	$< 6.77 \times 10^{-3}$	New material

4.2 Development of a low-α μ-PIC

4.2.1 Structural check of the low-α μ-PIC

A new μ-PIC with the main background source removed had been developed. This detector was named " Low-α μ-PIC ". The cross sectional view of the low-α μ-PIC is shown in Figure 4.2. The low-α μ-PIC was made by replacing the PI100(w/GC) µm part with the new material, PI(w/o GC)+epoxy. Figure 4.3 shows the appearance of the $10 \times 10\,\mathrm{cm}^2$ low-α μ-PIC prototype. It was produced in 2014. No problem was found for the production caused by changing the material. The microscopic view of the pixel electrodes is shown in Figure 4.4. Material change did not cause significant displacement of the anode electrode and the cathode electrode.

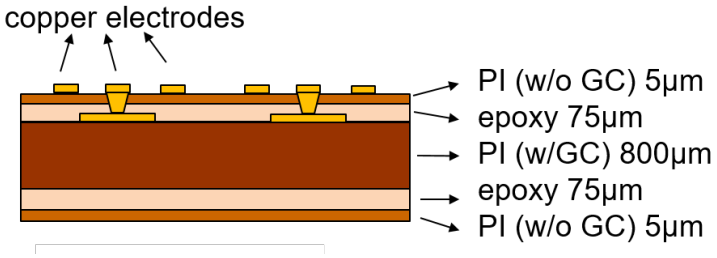

Figure 4.2: The cross sectional view of the low-α μ-PIC.

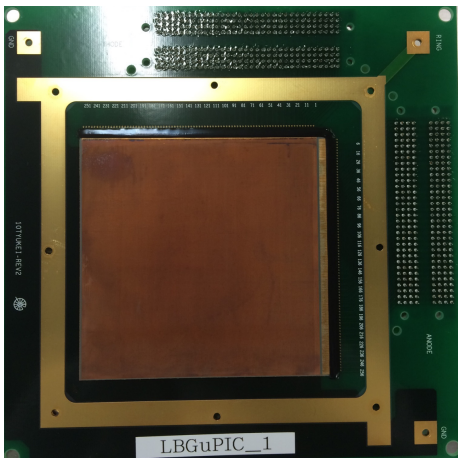

Figure 4.3: The picture of a $10 \times 10\,\mathrm{cm}^2$ low-α μ-PIC prototype.

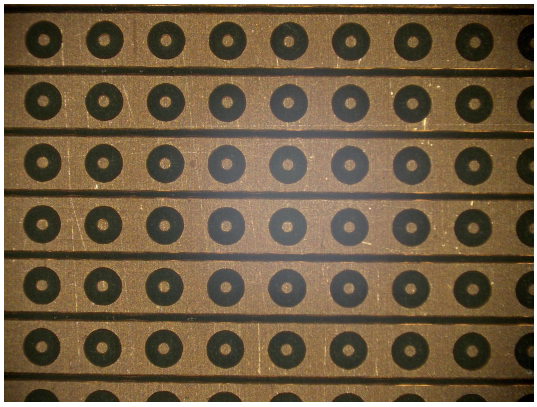

Figure 4.4: The microscopic view of the pixel electrodes of the low-α μ-PIC prototype.

The manufacturing method of the low-α μ-PIC is explained. The steps in the schematic view of the production process of a μ-PIC (Figure 4.5) are as follows. Samples were kept in the manufacturing process for investigating the possible contamination of radioactive impurities during the fabrication.

step 1 PI(w/GC) 800 μm of the core substrate was prepared. This was used as the sample 1.

step 2 Anode strips were formed on the PI(w/GC)800 µm, and PI(w/o GC)+epoxy and PI(w/GC) 800 µm were pressed together.The material after pressing was used as the sample 2.

step 3 After the holes were made by the laser, plating process was performed by growing a copper electrode. This material was used as the sample 3.

step 4 After processing to electrode for wire bonding, it became a finished product.This was used as the sample 4.

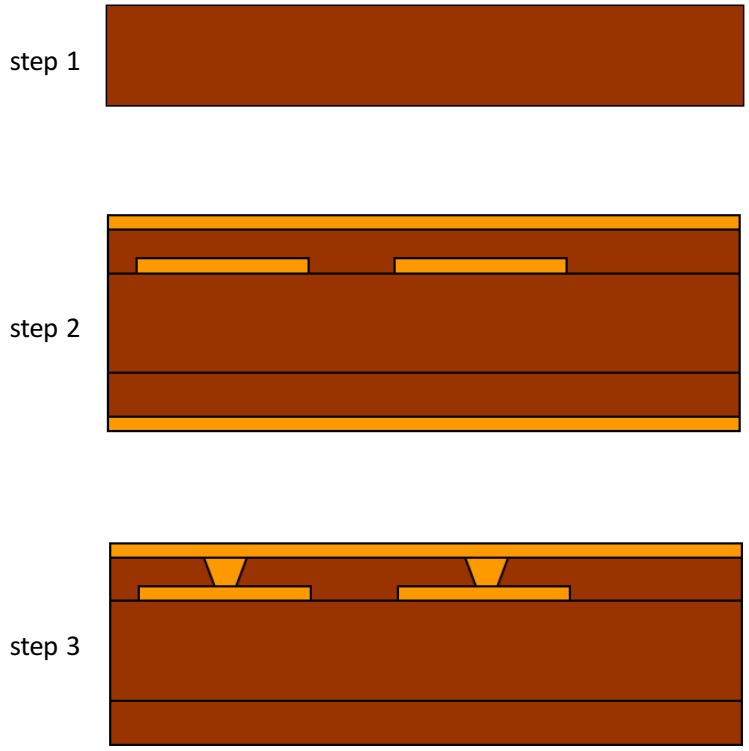

Figure 4.5: Production process of the low-α μ-PIC.

The U/Th contamination in the samples of the low-α μ-PIC production process was measured with the HPGe at the University of Tokyo Hongo Campus. Table 4.3 shows sample details and γ-ray detection efficiencies for each energy of interests, Table 4.4 shows the measurement results. Table 4.5 and Figure 4.6 show the radioactivity per μ-PIC unit area. From these result, it was found that the U/Th contamination of the low-α μ-PIC prototype (step 4 in Table 4.5) can be explained by the original contamination is the PI 800 µm part of the core substrate (step 1 sample in Table 4.5). Also, from Table 4.5 and Figure 4.6, the U/Th contaminations of sample 1 and sample 4 were found to be consistent with in errors, which indicates that there was no radioactive impurity contamination in the process of making the low-α μ-PIC prototype. From this, it can be said that U/Th contamination in the low-α μ-PIC prototype was as expected.

Table 4.3: Details of the measurement sample and γ-rays detection efficiency by energy.

	measurement	sample		efficiency		
Sample	Measurement period[day]	Mass[g]	Geometry [cm^3]	93 keV[%]	583 keV[%]	609 keV[%]
Sample 1	6.75	35.80	$5 \times 5 \times 0.69$	15.17	4.97	4.77
Sample 2	6.75	43.16	$5 \times 5 \times 0.79$	14.73	4.79	4.49
Sample 3	6.00	51.06	$5 \times 5 \times 0.60$	14.38	4.54	4.39
Sample 4	5.25	20.78	$5 \times 5 \times 0.40$	16.59	5.37	5.13

Table 4.4: U/Th contents of the quality control samples. Only the statistical errors are shown.

Sample	^{238}Umiddle stream [10^{-6} g/g]	^{238}Uupper stream [10^{-6} g/g]	^{232}Th [10^{-6} g/g]
Sample 1	$(6.2 \pm 0.1) \times 10^{-1}$	$(7.7 \pm 0.2) \times 10^{-1}$	2.99 ± 0.05
Sample 2	$(4.9 \pm 0.1) \times 10^{-1}$	$(5.5 \pm 0.1) \times 10^{-1}$	2.46 ± 0.04
Sample 3	$(4.3 \pm 0.1) \times 10^{-1}$	$(4.7 \pm 0.1) \times 10^{-1}$	2.16 ± 0.04
Sample 4	$(4.9 \pm 0.1) \times 10^{-1}$	$(6.1 \pm 0.2) \times 10^{-1}$	2.61 ± 0.07

Table 4.5: U/Th per μ-PIC unit area. Only the statistical errors are shown.

Sample	^{238}Umiddle stream [μBq/cm^2]	^{238}Uupper stream [μBq/cm^2]	^{232}Th [μBq/cm^2]
Sample 1	1366 ± 23	1719 ± 42	2112 ± 35
Sample 2	1307 ± 23	1475 ± 40	2096 ± 35
Sample 3	1354 ± 25	1472 ± 42	2174 ± 39
Sample 4	1268 ± 34	1580 ± 62	2150 ± 54

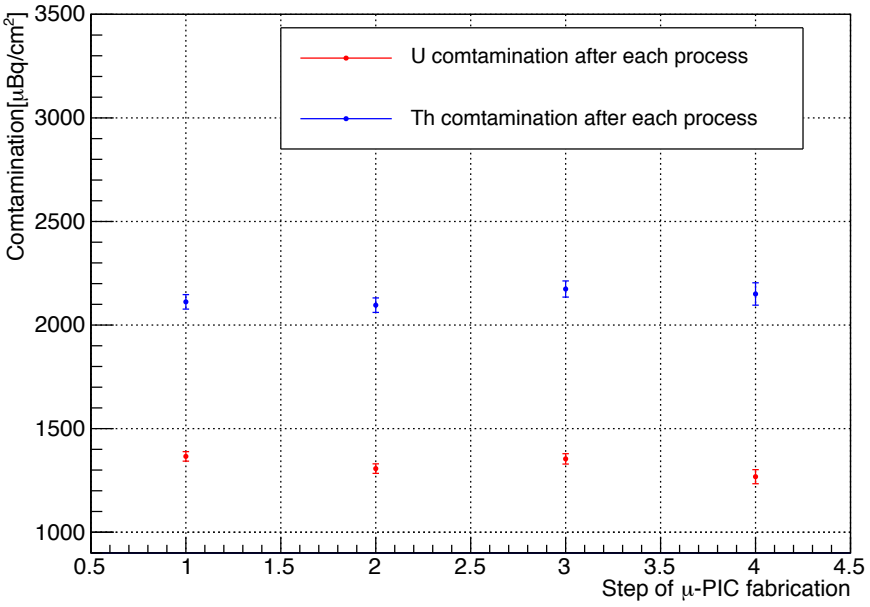

Figure 4.6: U/Th per μ-PIC unit area. Only the statistical errors are shown.

The geometry of the manufactured low-α μ-PIC were measured. The diameters of the anode electrodes (d_a in Figure 4.7), the diameters of the cathode holes (d_c in Figure 4.7)

and the height of the electrodes(t_{ac} in Figure 4.7) were measured using the digital microscope (KEYENCE VHX-2000). An example of a $10\times10\,cm^2$ μ-PIC image viewed with a digital microscope is shown in Figure 4.8. The measurement results of each parameter are listed in Table 4.6. Since the thickness of the insulator (t_i in Figure 4.7) can not be measured for the final products, the design values are shown. The measurement points were five places in total, four corners (about 4 mm inside from the edge) and the center of the detectors, and the average values and their standard deviations of five places are listed in Table 4.6. After confirming that there was no problem in the production of the 10 $\times$ 10 cm^2 low-α μ-PIC, 30 $\times$ 30 cm^2 low-α μ-PIC was manufactured in 2016. The outlook of the 30 $\times$ 30 cm^2 low-α μ-PIC after mounting on the board is shown in Figure 4.9. There was no problem due to enlarging the μ-PIC size to 30 cm and board mounting was also succeeded. The results of each measurement are listed in Table 4.6.

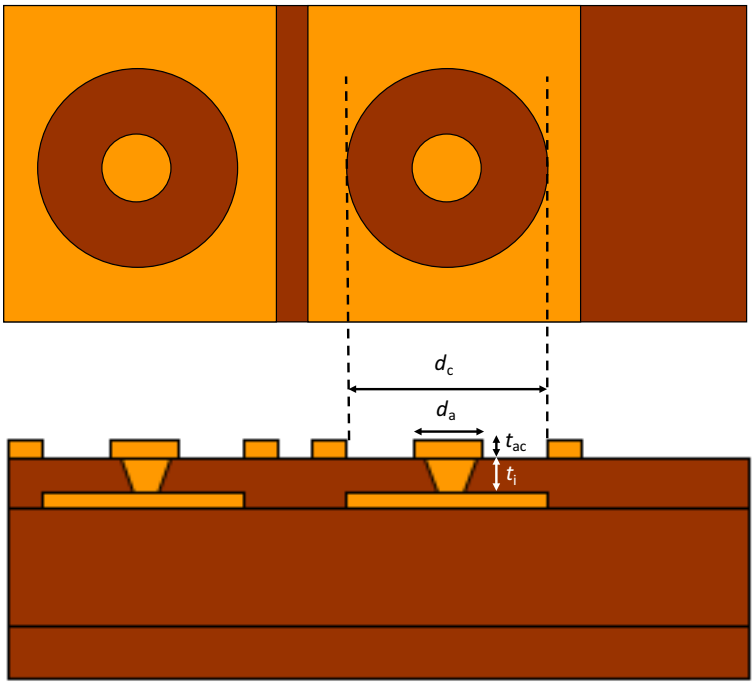

Figure 4.7: The measurement parameters of the 10 $\times$ 10 cm^2 stndard μ-PIC and the 10 $\times$ 10 cm^2 low-α μ-PIC.

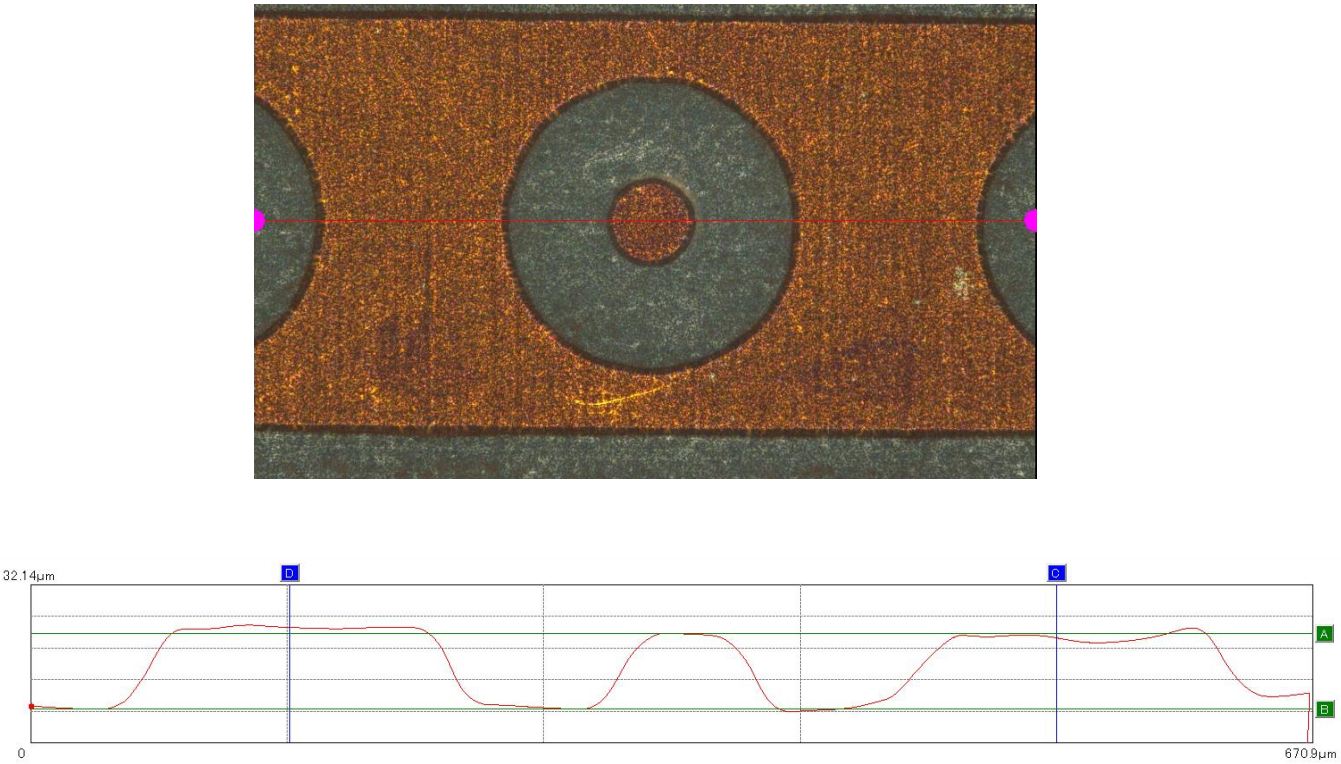

Figure 4.8: An example of cross sectional profile of the 10 × 10 cm^2 μ-PIC with the digital microscope. The sectional profile on the magenta line in the above figure is the lower figure.

Table 4.6: The measurement results and the design value of each parameter of 10 × 10 cm^2 standard(Std) μ-PIC and the 10 × 10 cm^2 low-α(LA) μ-PIC. The errors are the standard deviation. The parameters in the table are defined in Figure 4.7.

Parameter	10×10 cm^2 Std μ-PIC[µm]	10×10 cm^2 LA μ-PIC[µm]	30×30 cm^2 LA μ-PIC[µm]	Design value of std μ-PIC	Design value of LA μ-PIC[µm]
d_a	58.7 ± 2.8	64.4 ± 2.8	62.9 ± 2.5	60	60
d_c	251.2 ± 3.4	240.0 ± 3.0	242.3 ± 2.3	250	250
t_{ac}	10.7 ± 0.8	15.4 ± 1.1	14.1 ± 1.4	15	20
d_i				75	80

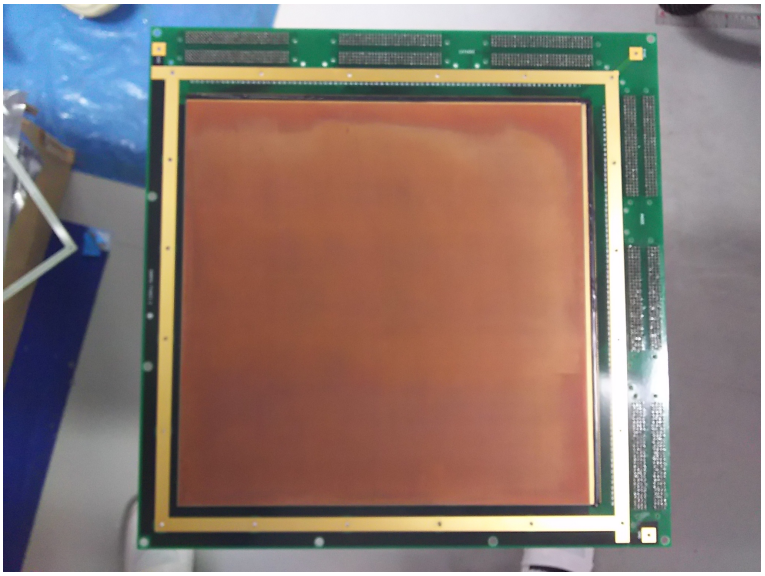

Figure 4.9: The outlook of the 30 × 30 cm^2 low-α μ-PIC after mounting to the board.

4.2.2 Performance simulation

A gas amplification simulation was carried out to predict the performance of the low-α μ-PIC. The simulation study was carried out using Garfield++[39]. Garfield++ is a toolkit for the detailed simulation of particle detectors that use gas and semi-conductors as sensitive medium. It was compatible with MPGD for microscopic calculations and can be calculated in three dimensions. It consists of a combination of multiple simulators, Heed[40] for ionization and Magboltz[41] for charge transport. A simple three dimensional electric field structure can be created with the default tool in Garfield ++, but complicated things need to be calculated by an external program. In this study, we used Gmsh[42] for production and mesh creation of the μ-PIC geometry and Elmer[43] for electric field calculation. Figure 4.10 shows the geometry of the μ-PIC produced with Gmsh, Figure 4.11 shows the mesh structure of μ-PIC produced with Gmsh based on the geometry, and Figure 4.12 shows the electric field structure of the μ-PIC calculated by Elmer based on the mesh structure.

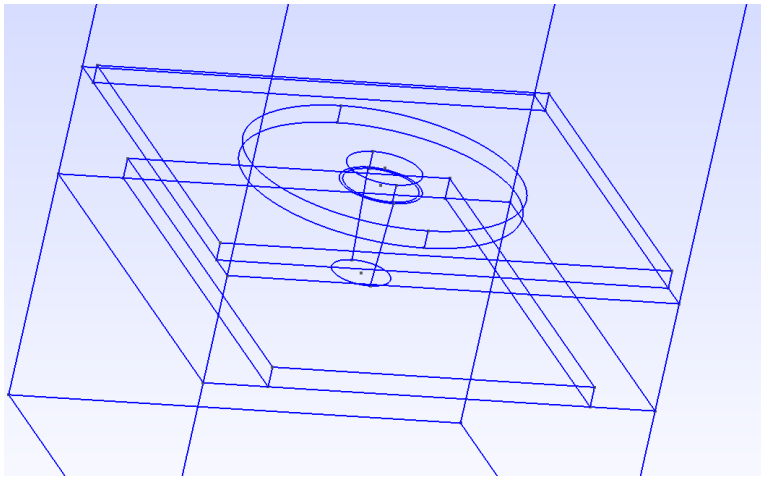

Figure 4.10: The geometry of the μ-PIC produced with Gmsh.

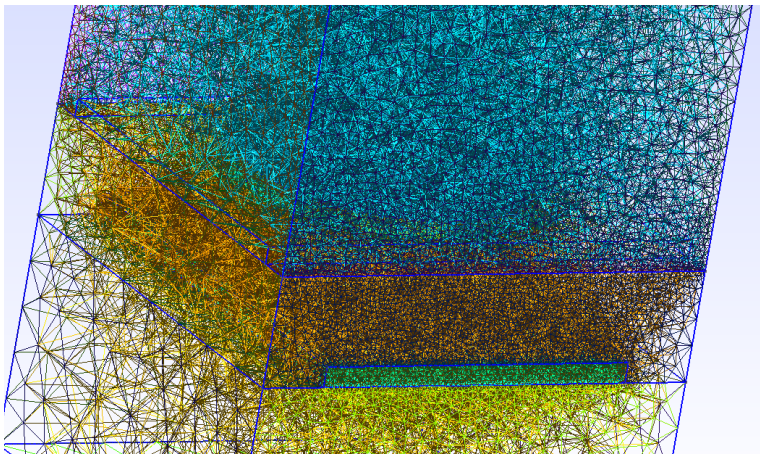

Figure 4.11: The mesh structure of the μ-PIC produced with Gmsh.

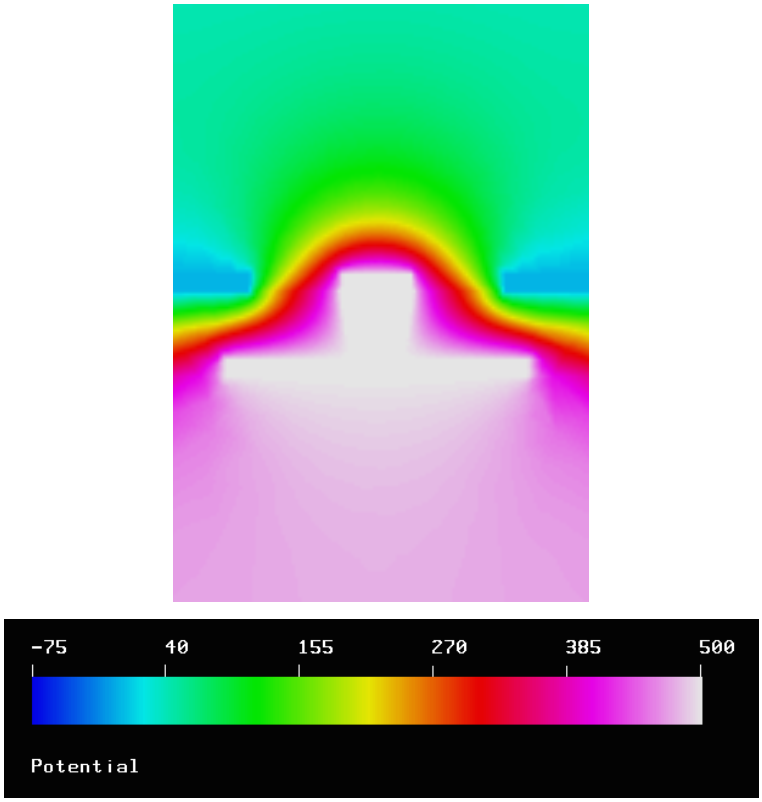

Figure 4.12: The electric field structure calculated by Elmer based on the μ-PIC mesh structure. The anode voltage is 500 V. The color contour represents the magnitude of the potential [V].

The gas region above the electrodes with a depth of 1.5 mm for the electron drift was filled with argon-ethane gas mixture (9:1) at a pressure of 760 Torr in Garfield++ simulation. Argon-ethane gas mixture (9:1) is widely used in the gas detector performance check because the gas gain is large. Seed electrons are generated at a random position in the region of $400 \times 400\,\mu m^2$ 1.0 mm above the electrodes(Figure 4.13). The drift electric field is set to 0.5 kV/cm, and the cathode voltage is set to 0 V. Nominal values were used as the dielectric constants of the insulator of the standard μ-PIC and low-α μ-PIC; 3.2 and 4.3, respectively. The dielectric constants of the gas and electrodes were set at 1 and 10^{10}, rspectively. The ratio of Penning effect is set to 0.31 from Ref. [21]. The simulation result of the gas gain is shown in Figure 4.14 and Figure 4.15.

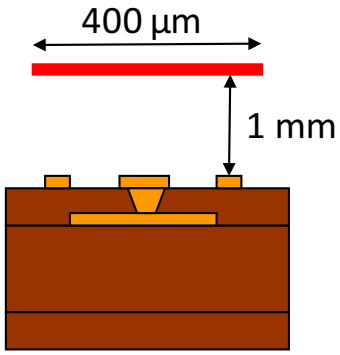

Figure 4.13: The region where the seed electrons are generated. Initial electrons were generated at a random position in the red region of $400 \times 400\,\mu m^2$ and 1.0 mm above the electrodes.

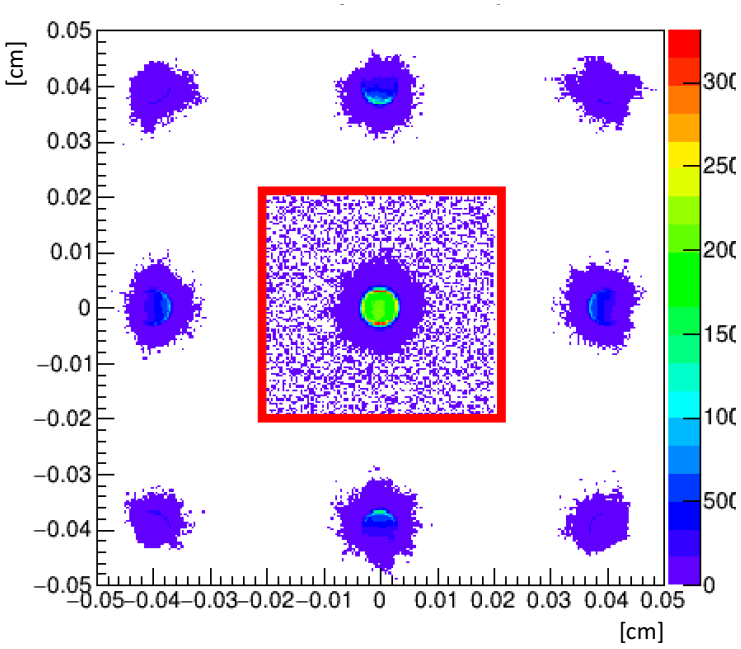

Figure 4.14: The 2D map of the initial position of electrons of a standard μ-PIC with anode voltage of 500V. The seed electrons were generated from inside the red square 1 mm above the μ-PIC plane.

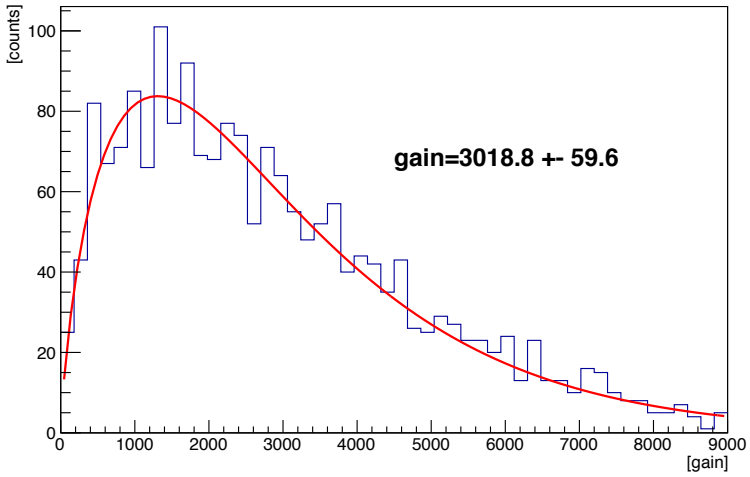

Figure 4.15: A simulation result of gas gain using Garfield++. This histogram is the single-electron spectrum of 2000 events of a low-α μ-PIC with the anode voltage of 500V. The red line shows the fit result with the Polya distribution.

The distributions of gains of single electrons spectrum is known to be described by the Polya distribution for proportional counters. The Polya distribution is written as follows

$$g(x) = \left(\frac{x(1+\theta)}{\bar{A}} \right)^{\theta} \exp\left(-\frac{x(1+\theta)}{\bar{A}} \right) \tag{4.1}$$

where x is the gas gain, θ is gives the theoretical limit of energy resolution and it is related to the proportion of electrons with the energy beyond the ionization threshold and $\bar{A}$ is the average gas gain. Gas gain is obtained by fitting the Single-electron spectrum with Polya distribution. $\bar{A}$ is the gas gain obtained from the simulation.

Figure 4.16 shows the anode voltage dependence of the gas gain by the simulation. The geometries of the μ-PICs are shown in Table 4.6. The simulation that indicated the low-α μ-PIC would about 1.3 times higher gain than the standard μ-PIC. This result was reasonable because the electrodes of the low-α μ-PIC were higher than those of standard μ-PIC.

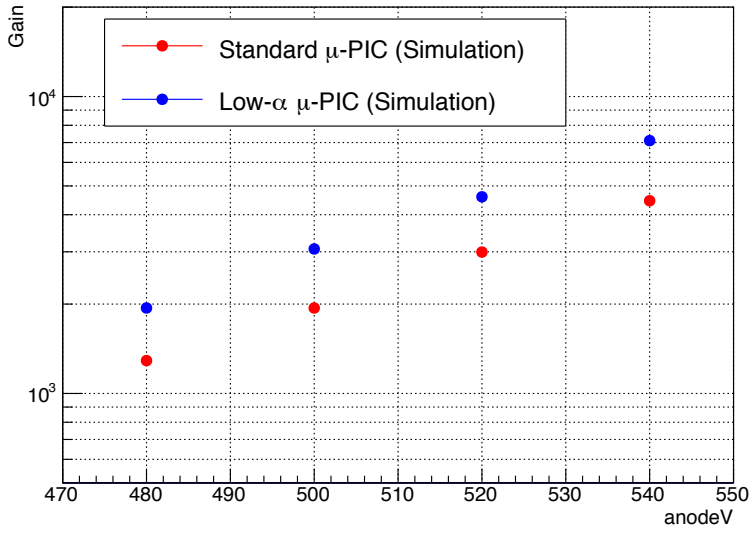

Figure 4.16: Simulation results of the gas gains as a function of the voltage supplied to the anode electrodes of the standard μ-PIC and the low-α μ-PIC.

4.3 Performance of the low-α μ-PICs

The performance of the low-α μ-PICs was measured in the test chamber. The position dependence and the anode-voltage dependence of gas gains of the low-α μ-PICs were investigated. Results are also discussed in terms of the requirements of the low-α μ-PIC.

4.3.1 Set up

The outer view of the test chamber and a schematic drawing of the set up used for the performance tests are shown Figure 4.17 and Figure 4.18, respectively. The test chamber was made of aluminum. There were nine kapton window of 10×10 cm^2. The thickness of the kapton window was 125 µm. The drift mesh was made of SUS304, the wire diameter is 0.02 mm, the mesh pitch is 0.068 mm, and the opening ratio was 59.7%. The detector was set in the vessel filled with a gas flow of argon-ethane mixture (9:1). A drift voltage of -500V was supplied to the drift mesh that formed a drift field of 0.55 kV/cm in a drift length of 0.9 cm. Since the μ-PIC part is 1 mm including the substrate, the drift length is 0.9 cm.

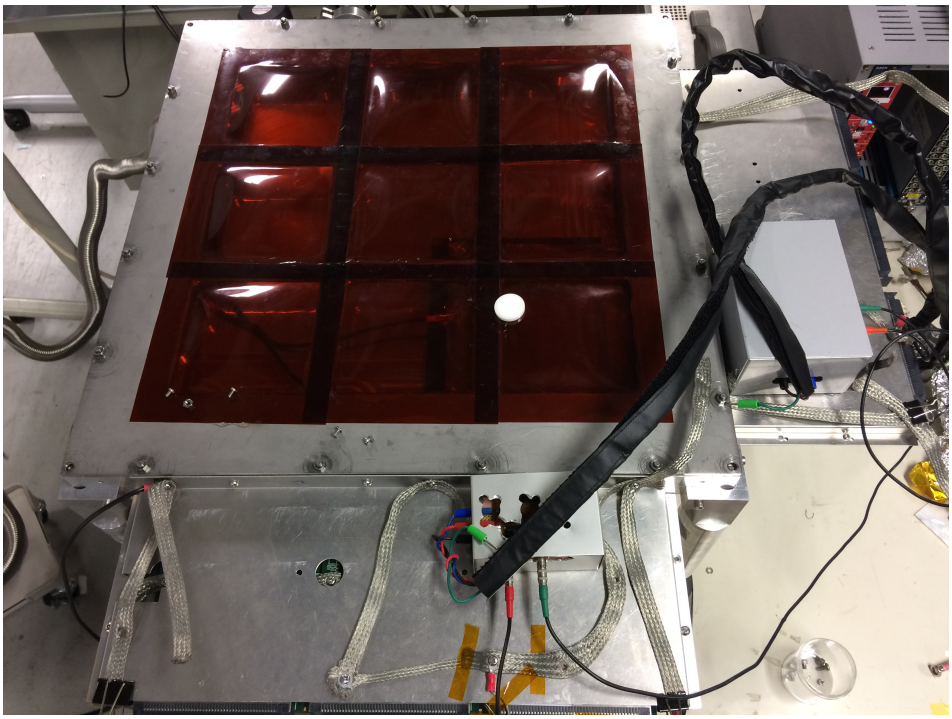

Figure 4.17: The outer view of the vessel used to evaluate the performance of the μ-PIC

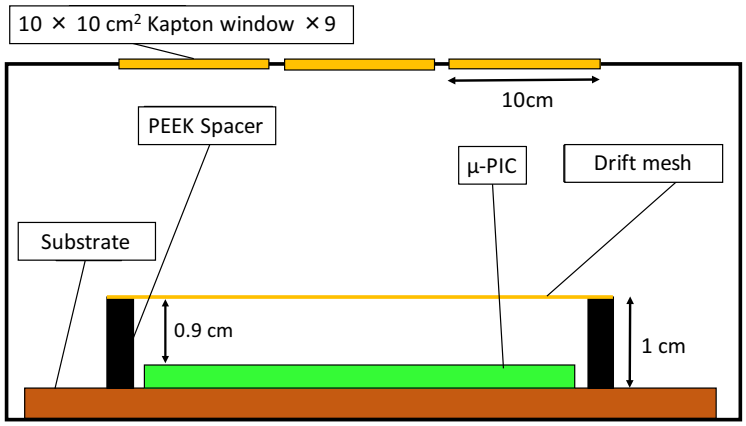

Figure 4.18: A schematic drawing of the detector used for the performance check of the μ-PICs.

4.3.2 Measurement method

The gas gains were measured by the characteristic X-rays from a radioactive source of ^{55}Fe. ^{55}Fe is a radioactive isotope which decays into ^{55}Mn by an electron-capture process. X-rays of 5.9 keV are emitted from the ^{55}Fe source.

A flowchart of the data acquisition system (DAQ) is shown in the Figure 4.19. A GNV-240G (GNomes Design) was used as the waveform digitizer. The dynamic range and resolution of the voltage were 0 - 1 V with 8 bit and those of time were 8168 ns

and 2 ns. 32 strips of the anode electrodes were connected and the charges from them were amplified by an charge-sensitive amplifier and used as a trigger. 32 strips of cathode electrodes were also connected, and their charges were amplified by an charge-sensitive amplifier and recorded by a waveform digitizer. CREMAT CR110 was used for the anode amp and CREMAT CR-110 + LF356N were used for the cathode amplifier. The anode amplifier circuit is shown in Figure 4.20, and the cathode amplifier circuit is shown in Figure 4.21. The gain of the anode and cathode amplifiers were -0.7 [V/pC] and -4.0 [V/pC], respectively. An example of waveform is shown in Figure 4.22. The rise time constant of the signal is about 1000 ns.

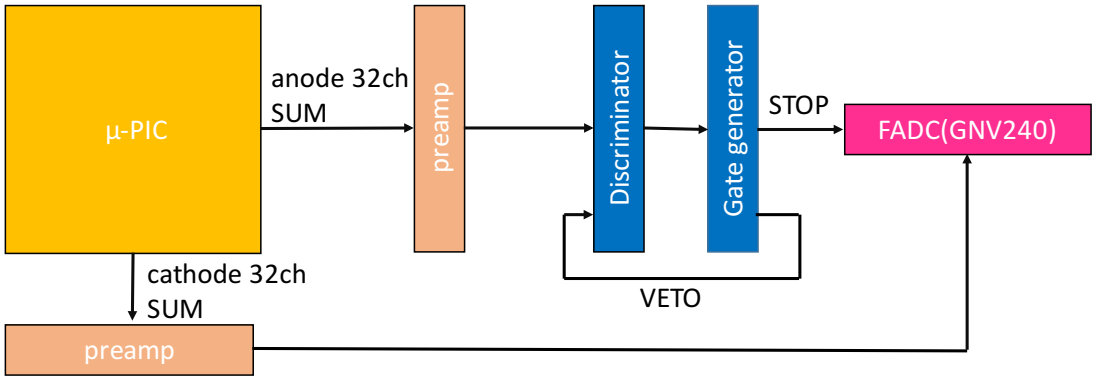

Figure 4.19: The set up of DAQ used for the gas gains measurement.

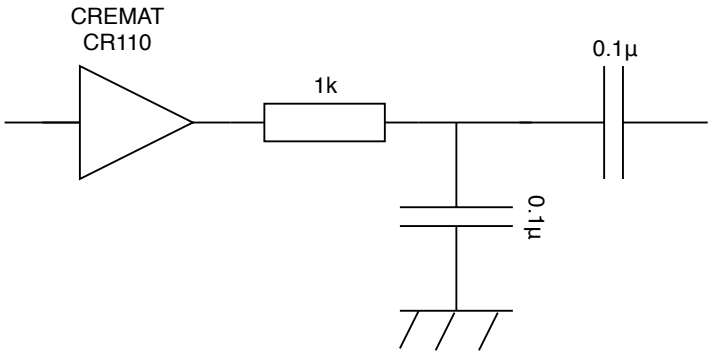

Figure 4.20: The anode amplifier circuit.

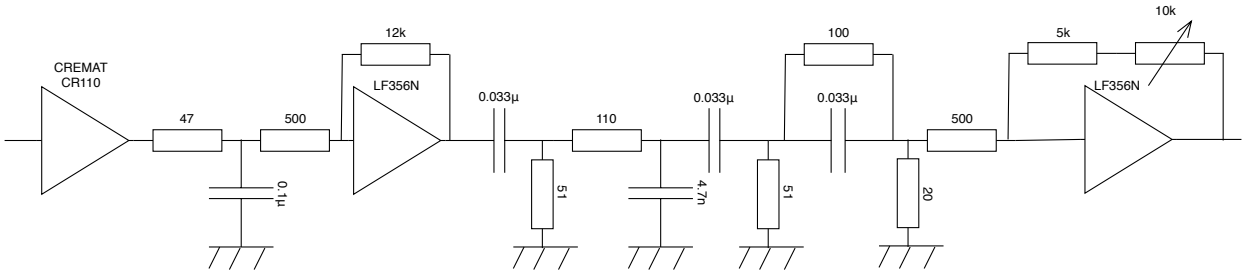

Figure 4.21: The cathode amplifier circuit.

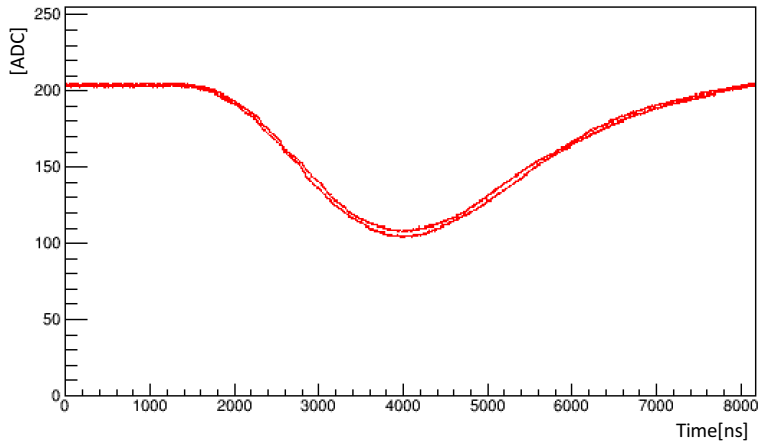

Figure 4.22: An example of a waveform.

The peak value from the waveform was used to calculate the gas gains. 0 - 500 ns region was defined as the base region and 2000 - 7000 ns region was defined as the signal region. The average value of the base region was used as the base value, and the maximum value of the signal region was taken as the peak value. The pulse height value of the signal was calculated by the (peak value) - (base value) to obtain the energy spectrum of the signal.

Since the signal is recorded by the GNV-240G, it is necessary to calibrate the DAQ including the cathode amplifier and the GNV-240G. Figure 4.23 shows the diagram for the calibration. A test charge was fed to the amplifier by inputting a square wave through a capacitor (1 pF). A waveform corresponding to the charge amount was recorded. The trigger signal from the pulse generator was used to stop the GNV-240G. The input charge was scanned and the response is shown in Figure 4.24. The calibration factor was given by Eq.(4.2).

$$G_{\mathrm{amp}}[\mathrm{pC/ADC}] = \frac{[\mathrm{pC}] + 5.71 \times 10^{-3}}{1.12 \times 10^{-3}} \tag{4.2}$$

Eq.(4.2) and Eq.(4.3) were used to convert the pulse height value of the signal into the charge amount and calculate the gas gains.

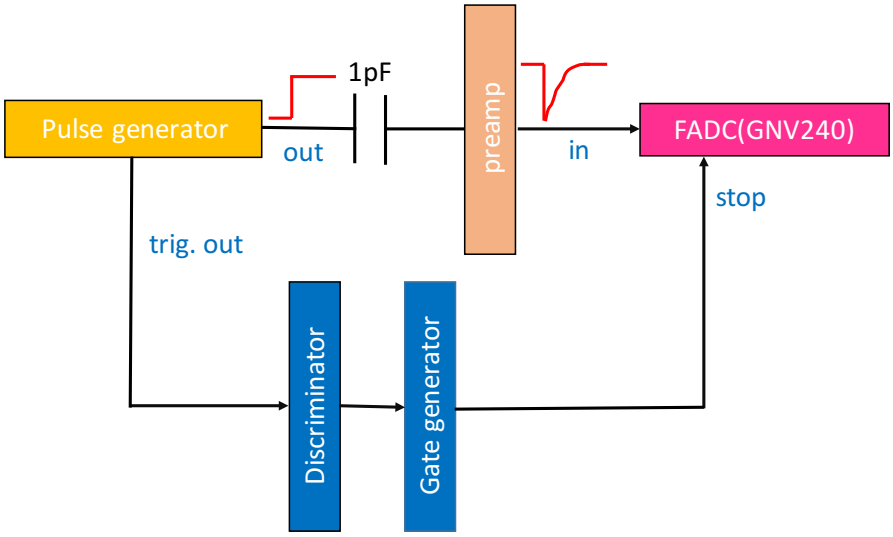

Figure 4.23: The DAQ for the calibration.

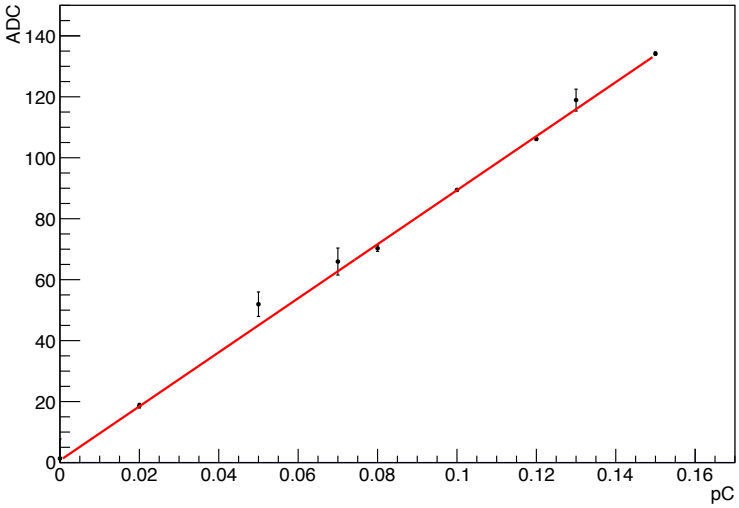

Figure 4.24: The calibration line of ADC and charge.

An energy spectrum of ^{55}Fe is shown in Figure 4.25. The anode voltage is 520 V. This is the main peak at 5.9 keV. In the gas gains measurement, this main peak events were used. The gas gains were calculated from the results fitted with a Gaussian distribution. The gas gain was defined as follows

$$G_{\mathrm{gas}} = \frac{W_{\mathrm{Ar}} \times G_{\mathrm{amp}}[\mathrm{pC/ADC}] \times \mathrm{ADC\,value}}{(5.9\,\mathrm{keV}) \times \mathrm{e}^{-}} \tag{4.3}$$

where $\mathrm{W_{Ar}}$ is the W value of argon (26 eV), and e^{-} is the elementary charge. The gas gain of the anode voltage of 520 V is 3051.0 ± 8.8. The energy spectrum of ^{55}Fe calibrated to energy is shown in Figure 4.26.

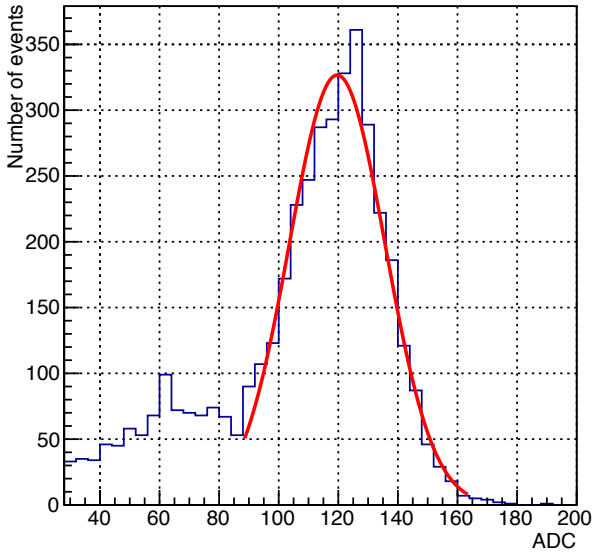

Figure 4.25: The energy spectrum of ^{55}Fe measured by the $10\times10\,\mathrm{cm}^2$ standard μ-PIC. The anode voltage is 520 V. The gas gain is 3051.0 ± 8.8.

4.3.3 Measurement result

The requirements for the low-α μ-PIC were set as follows.

- Non-uniformity of the gas gain : $< 20\,\%$
  From the energy resolution of 6 MeV radon peak at RUN14[33]
- Gas gain : > 1000 using the argon-ethane gas mixture(9:1) at 760 Torr
  In order to have a sufficient detection efficiency for a nuclear recoil event with the 50 keV threshold under dark matter search conditions(CF_4 at 76 Torr)
- Surface α-ray rate : $< 1/50$
  In order to reach the DAMA region

The gas gains were measured the for the $10\times10\,\mathrm{cm}^2$ standard μ-PIC (SN 071220-1), the prototype $10\times10\,\mathrm{cm}^2$ low-α μ-PIC (SN 160115-2) and the $30\times30\,\mathrm{cm}^2$ low-α μ-PIC (SN 161130-5). The measurement of the position dependence of the $10\times10\,\mathrm{cm}^2$ standard μ-PIC and the $10\times10\,\mathrm{cm}^2$ low-α μ-PICs were carried out at the anode voltage of 520 V and 530 V, respectively. These results are shown in Figure 4.27. Numbers in the histogram represent relative gains. The histograms of the relative gains are shown in Figure 4.28. The energy resolution of 6 MeV radon peak at RUN14 was 20 %. Therefore, the requirement of the non-uniformity of the gas gain of the low-α μ-PIC is set to 20 %. Here, the non-uniformity of the gas gain σ was represented as a ratio normalized by the average value of the amplification as follows

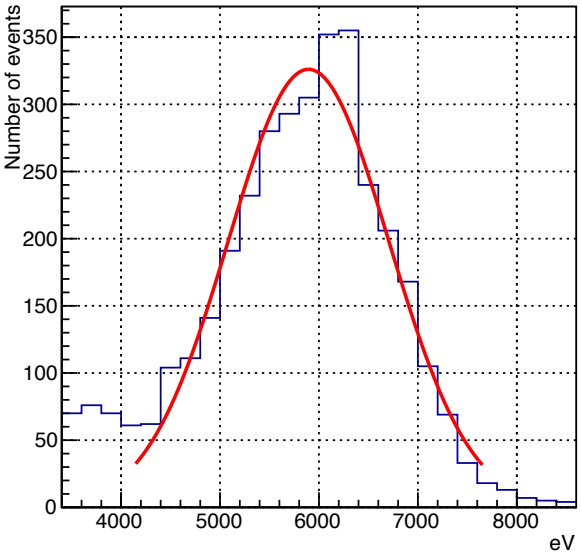

Figure 4.26: The energy spectrum of ^{55}Fe calibrated to energy. This was measured by the $10\times10\,\mathrm{cm}^2$ standard μ-PIC. The anode voltage is 520 V.

$$\sigma\ [\%] = \frac{S_{G_{\mathrm{gas}}}}{\overline{G_{\mathrm{gas}}}} \times 100, \tag{4.4}$$

$$\overline{G_{\mathrm{gas}}} = \frac{1}{N}\sum_i \sum_j G_{\mathrm{gas}}(i,j), \tag{4.5}$$

$$S_{G_{\mathrm{gas}}} = \sqrt{\frac{1}{N}\sum_i \sum_j (G_{\mathrm{gas}}(i,j) - \overline{G_{\mathrm{gas}}})^2}, \tag{4.6}$$

where, $S_{G_{\mathrm{gas}}}$ is the standard deviation of the position dependence, $\overline{G_{\mathrm{gas}}}$ is the average value of the position dependence of gas gains, N is the number of the measurement points and $G(i,j)$ is the gas gain at the measurement points. i and j represent the anode and the cathode position, respectivety. From this point onwards, unless otherwise specified, the defined σ is normalized by the average value as in Eq.4.4. The average gas gain of the standard $10\times10\,\mathrm{cm}^2$ μ-PIC was 1312 and the average gas gain of the $10\times10\,\mathrm{cm}^2$ low-α μ-PIC was 822. The non-uniformity of the gas gain of the $10\times10\,\mathrm{cm}^2$ standard μ-PIC ($\equiv \sigma_{\mathrm{sta10cm}}$) and low-$\alpha$ μ-PIC ($\equiv \sigma_{\mathrm{LA10cm}}$) were 15 % and 13 %, respectively and the low-α μ-PIC was found to show a similar or better performance as the standard μ-PIC. They achieved 20% or less, which is the requirement of the position resolution.

The $30\times30\,\mathrm{cm}^2$ low-α μ-PIC was divided into 32 parts and the gas gains were measured. The measurement was carried out at the anode voltage of between 520 V and 540V. The measurement results of the $30\times30\,\mathrm{cm}^2$ low-α μ-PIC are shown in Figure 4.29 and Figure 4.30. The position of the square represents the measurement points. For the measurement points at the voltage different from 540 V, the value corrected to the one corresponding to 540 V gas gain based on the gain curve in Figure 4.29. The average gas gain of the $30\times30\,\mathrm{cm}^2$ low-α μ-PIC was 1997. The non-uniformity of the gas gain of the 30×30 cm^2 low-α μ-PIC was 16 % ($\equiv \sigma_{\mathrm{LA30cm}}$). The $30\times30\,\mathrm{cm}^2$ low-α μ-PIC was

measured every 5 cm and the measurement area was about 17 % of the all area. The non-uniformity of the gas gain of the 5×5 cm^2 area of the low-α μ-PIC was obtained from the measurement result of the 10×10 cm^2 low-α μ-PIC. The results for the 10×10 cm^2 low-α μ-PIC were divided into 4 parts, and the non-uniformity of the gas gain was calculated in each area. The average of the non-uniformity of the gas gain of the 5×5 cm^2 of the low-α μ-PIC ($\equiv \sigma_{\mathrm{LA5cm}}$) was 10 %. The non-uniformity of the gas gain of the whole 30×30 cm^2 low-α μ-PIC ($\equiv \sigma_{\mathrm{all\,LA30cm}}$) was calculated by combining this results with the non-uniformity measurement of 30×30 cm^2 by sampling. Obtained results was $\sigma_{\mathrm{all\,LA30cm}} = \sqrt{\sigma^2_{\mathrm{LA5cm}} + \sigma^2_{\mathrm{LA30cm}}} = 19$ %. This value satisfied the requirement of 20 %.

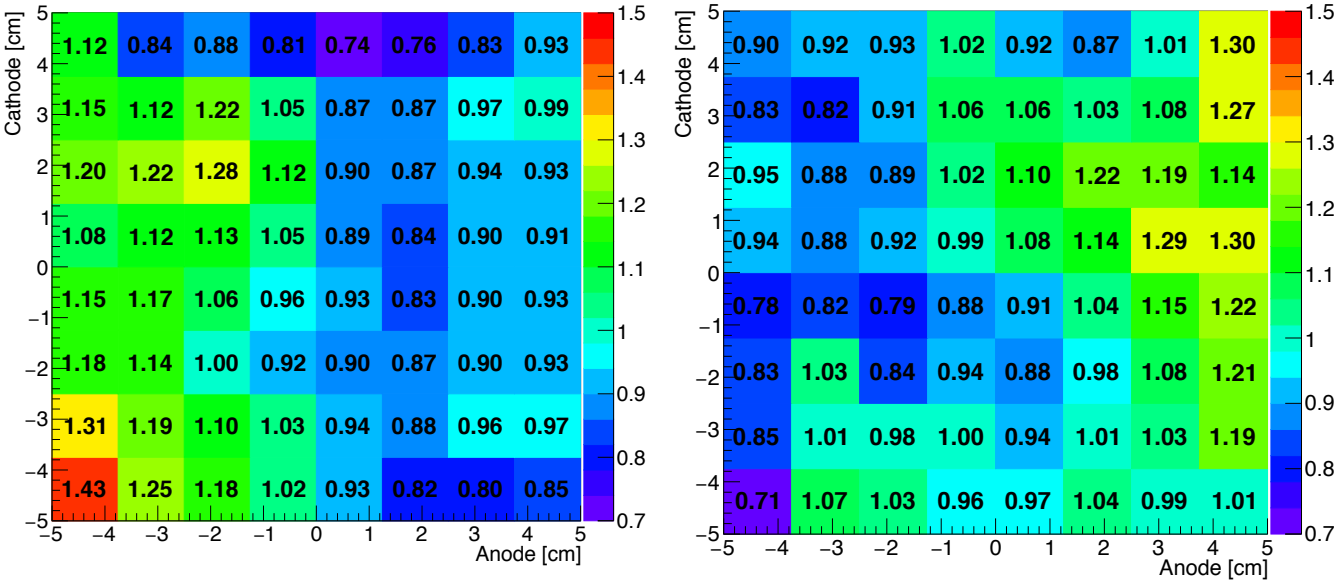

Figure 4.27: The position dependence of gas gains of 10 × 10 cm^2 standard μ-PIC (left) and Low-α μ-PIC (right). Numbers in the histogram represent relative gains. The measurement of the 10×10 cm^2 standard μ-PIC and the 10×10 cm^2 low-α μ-PICs were carried out at the anode voltage of 520 V and 530 V, respectively.

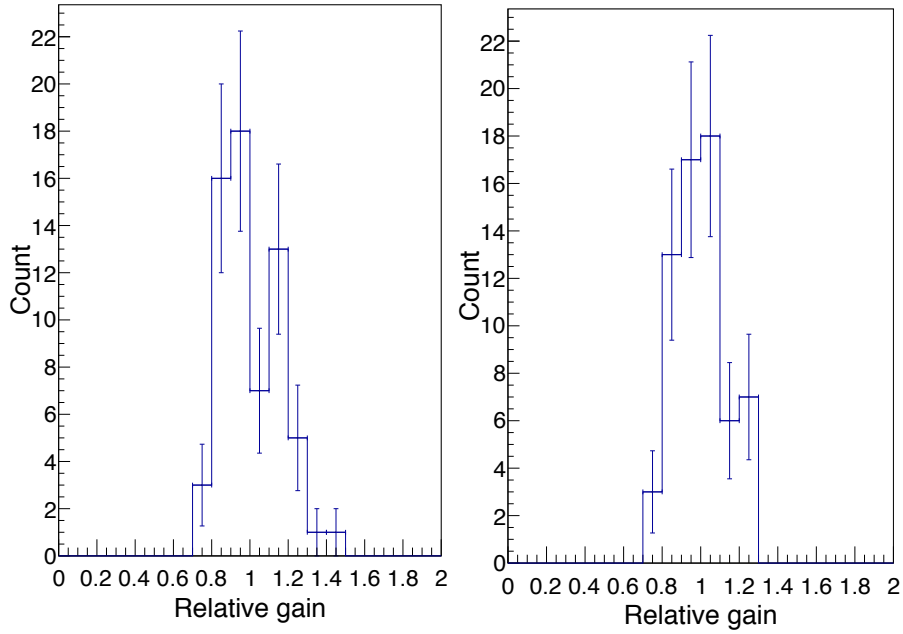

Figure 4.28: The position dependences of the gas gains of the $10\times10\,\mathrm{cm}^2$ standard μ-PIC (left) and $10\times10\,\mathrm{cm}^2$ low-α μ-PIC (right). The statistical errors are shown.

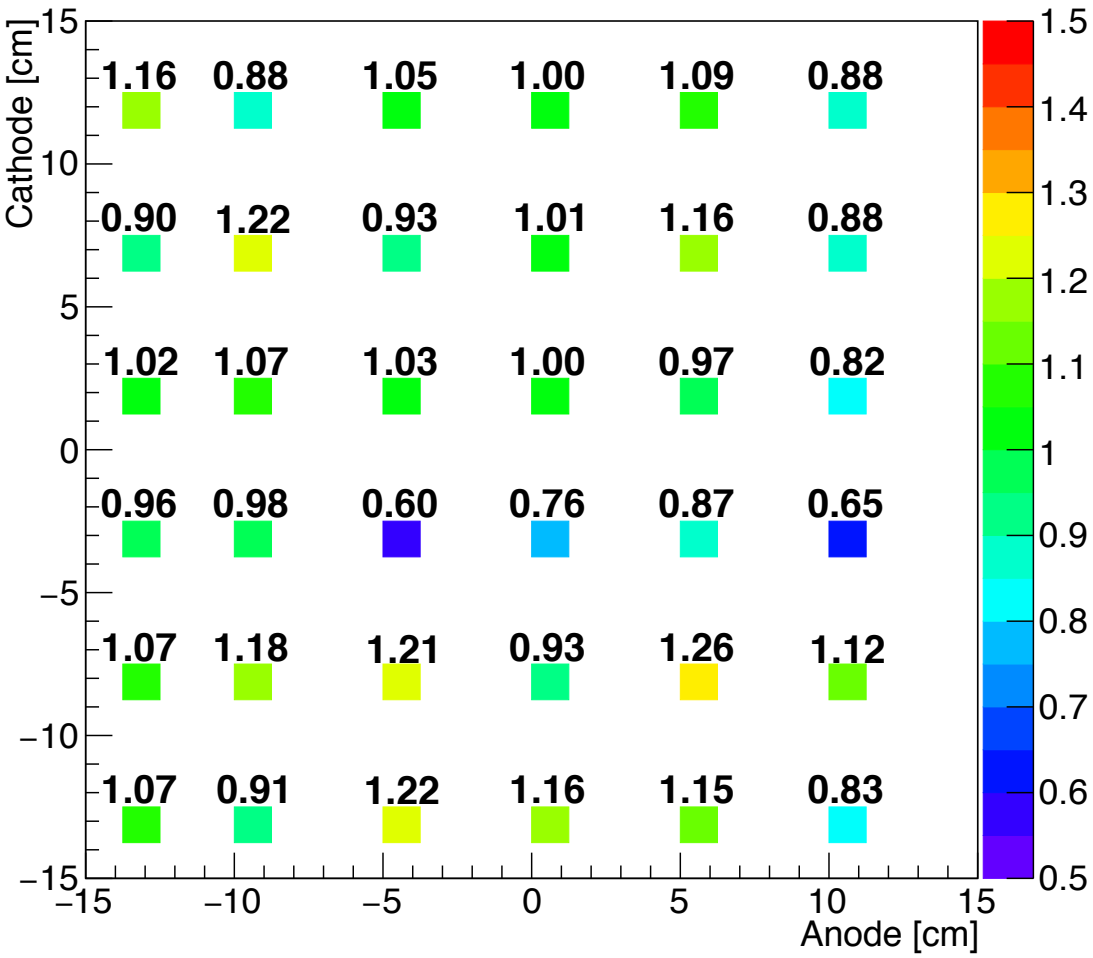

Figure 4.29: The position dependence of the gas gains of the 30 × 30 cm^2 low-α μ-PIC. Numbers in the histogram represent relative gains. The position and the size of the square represents the measurement points. The measurement was carried out at the anode voltage of between 520 V and 540V. The region measured at a voltage different from 540 V was corrected to the one corresponding to 540 V based on the gain curve.

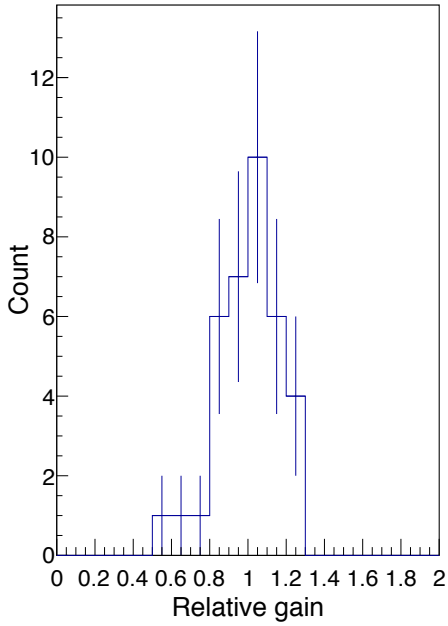

Figure 4.30: The position dependences of the gas gains of the $30\times30\,\mathrm{cm}^2$ low-α μ-PIC. The statistical errors are shown.

The comparison between the measurement result and the simulation using Garfield++ of the$10\times10\,\mathrm{cm}^2$ standard μ-PIC are shown in Figure 4.31. The upper limit of the measurement was determined by discharges, and the lower limit value was determined by the electric noise. As for the simulation of standard μ-PIC using Garfield ++, there existed a previous study[44]. It was confirmed that the simulation result using Garfield ++ was consistent with the measurement result using our system.

The anode-voltage dependences of the gas gain for $10\times10\,\mathrm{cm}^2$ and $30\times30\,\mathrm{cm}^2$ low-α μ-PICs are shown in Figure 4.32. Simulation results with a geometry constructed with measured parameters are shown for comparison. A significant difference between the measured and simulation results of the gas gain of the low-α μ-PIC s was observed. This difference will be discussed in Section 5. The requirement of gas gain with argon-ethane gas mixture (9:1) at 760 Torr was 1000. From Figure 4.32, both $10\times10\,\mathrm{cm}^2$ and $30\times30\,\mathrm{cm}^2$ low-α μ-PIC have achieved gas gain 1000 at 510 V and were found to satisfy the requirement.

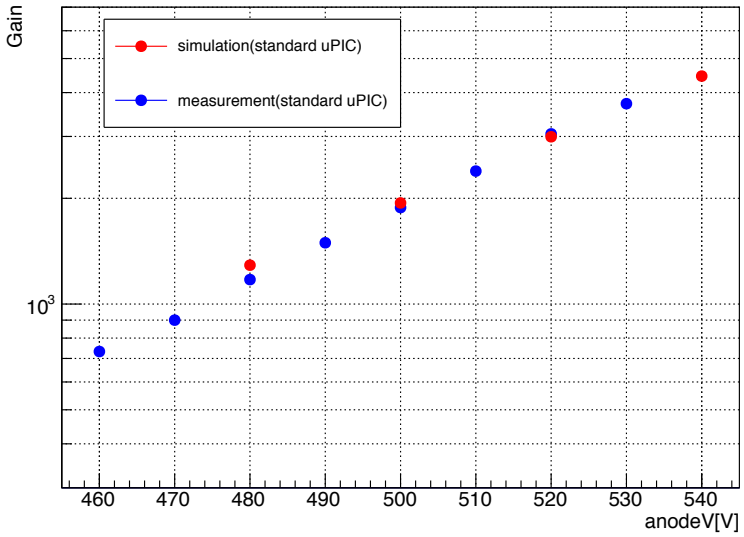

Figure 4.31: Gas gains as a function of the voltage supplied to the anode electrodes of the 10×10 cm^2 standard μ-PIC and the simulation by the geometry of the measurement result(Table 4.6) of standard μ-PIC.

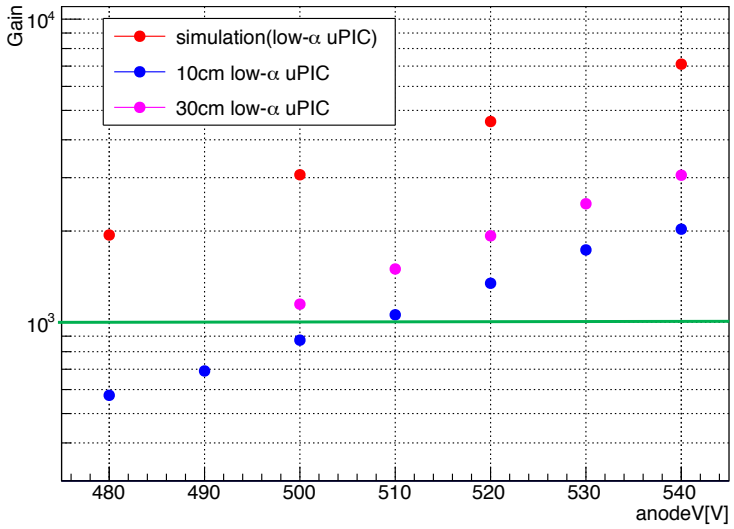

Figure 4.32: Gas gains as a function of the voltage supplied to the anode electrodes of the 10×10 cm^2 and 30×30 cm^2 low-α μ-PIC and the simulation by the geometry of the measurement result(Table 4.6) of the low-α μ-PIC. The green line represents the requirement of the gas gain.

4.4 Background measurement of the low-α μ-PIC

Since the main background source as the dark matter detector was the surface α-rays from the μ-PIC, it was necessary to measure the surface α-rays from the low-α μ-PIC. This measurement was carried out in the underground to reduce the cosmic ray background. The α-ray emission from the low-α μ-PIC was measured using the NEWAGE-0.3b' system at Kamioka underground laboratory. One of the $30\times30\,\mathrm{cm}^2$ low-α μ-PICs, S/N 161130-4,

was installed in the NEWAGE-0.3b', taking place of a standard μ-PIC, S/N 070309-1. The schematic view of the NEWAGE-0.3b' is shown in Figure 3.2. The detector condition is summarized in Table 4.7. The vacuum vessel was filled with CF_4 at 76 Torr. The vessel was equipped with a gas circulation system using cooled activated carbon. The measurement details are summarized in Table 4.8. The main run number(22) is changed when the state of the detector is changed. The sub run number(1) is changed when gas is changed.

	voltage	current
Low-α μ-PIC	470 V	~ 2 nA
GEM-top	-530 V	$< 1\,\mu$A
GEM-bottom	-280 V	$< 1\,\mu$A
DRIFT	-3.76 kV	21.9 μA

Table 4.7: Detector operation condition for the α-ray emission measurement of the low-α μ-PIC.

RUN ID	gas filling	period	live time	mass	exposure
RUN22-1	2018/06/06	2018/6/8 – 8/9	47.17 days	10.36 g	0.489 kg · days

Table 4.8: Conditions of underground measurement RUN22.

One of the largest concerns of the low-α μ-PIC was the stability of the detector, namely discharges. Figure 4.33 shows the anode current of the low-α μ-PIC where jumps in the current monitor can be recognized as the discharges. Only one discharge was recorded throughout the measurements time of about 47 days. The anode leak current during the stable operation was $\sim$ 2 nA. The current has no problem in applying voltage to the μ-PIC and it was found that stable measurement was realized.

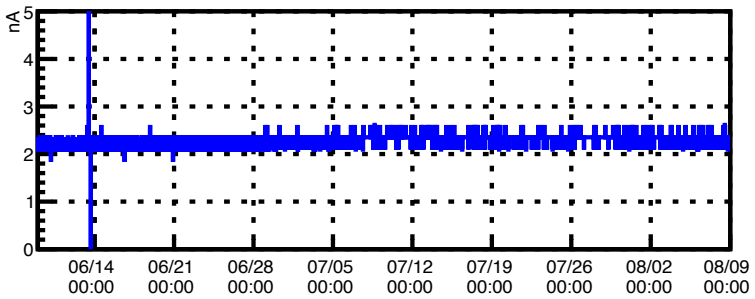

Figure 4.33: The current value of the low-α μ-PIC during the test run(RUN 22-1). The figure shows the monitored current in RUN 22-1. A current jump recorded on June14 is a discharge event.

α-ray events were selected by applying the cuts shown below. The fiducial cut and energy cut were the same as the previous one explained in Section 3.1.2. The length-cut and TOT-sum cut parameters were reconsidered because the gas gain was changed by

exchanging with the low-α μ-PIC. These cut parameters were determined as follows by comparing the electron recoil events caused by the ^{137}Cs radiation source and the nuclear recoil events caused by the ^{252}Cf radiation source.

- **Fiducial-cut** : -14 [cm] < X < 14[cm], -10 [cm] < Y < 14[cm]
- **Energy-cut** : 50 [keV] < Energy < 400[keV]
- **length-cut** : track-length[cm] $< 0.833 + 0.0017 \times$ E[keV]
  for the rejection of long events. (Figure 4.34)
- **TOT-sum-cut** : TOT-sum> 96
  for the rejection of non-continuous events. (Figure 4.35)

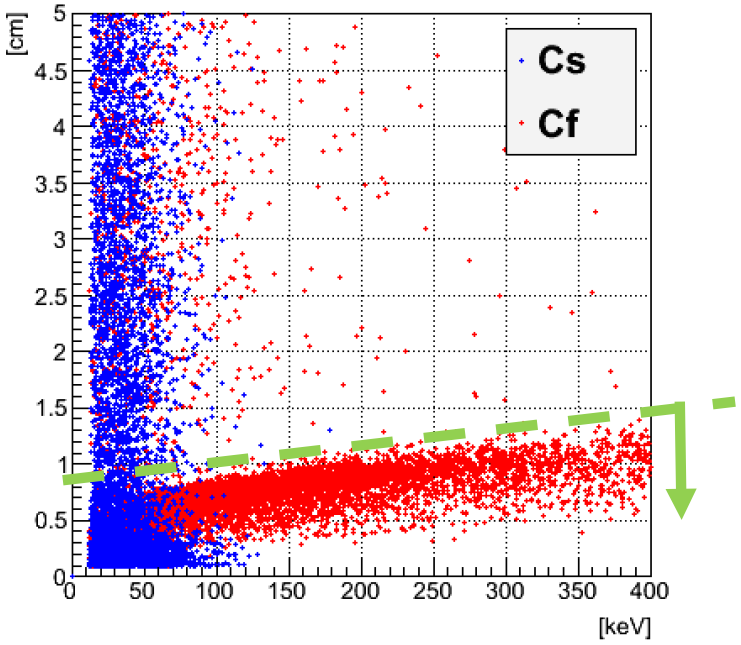

Figure 4.34: Energy dependence of the track length.

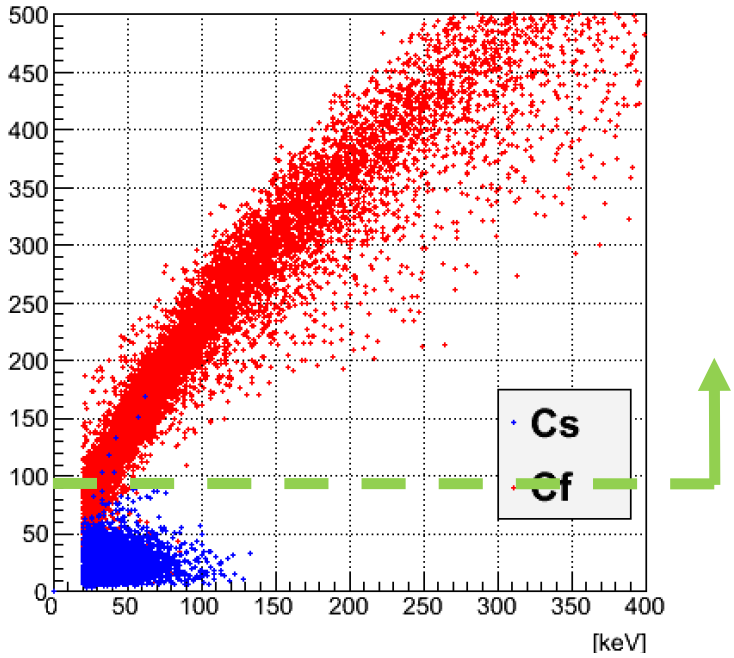

Figure 4.35: Energy dependence of the TOT-sum after the length cut.

Figure 4.36 shows the detection efficiency of the nuclear recoil events after the length cut and the TOT-sum cut. The detection efficiency of nuclear recoil event was obtained by comparing measurement data irradiated with neutron and the simulation. In the measurements of the detection efficiency, ^{252}Cf is placed at (0, 0, 25.5), (0, 25.5, 0), (0, 0, 47.5), (0, 0, -25.5), (0, -25.5, 0),(0, 0, -47.5). This is to cancel the track direction dependence. The detection efficiency is obtained by dividing the energy spectrum of the measured value by the energy spectrum in the simulation. Figure 4.36 shows the detection efficiency obtained by taking the and average the data form directions.

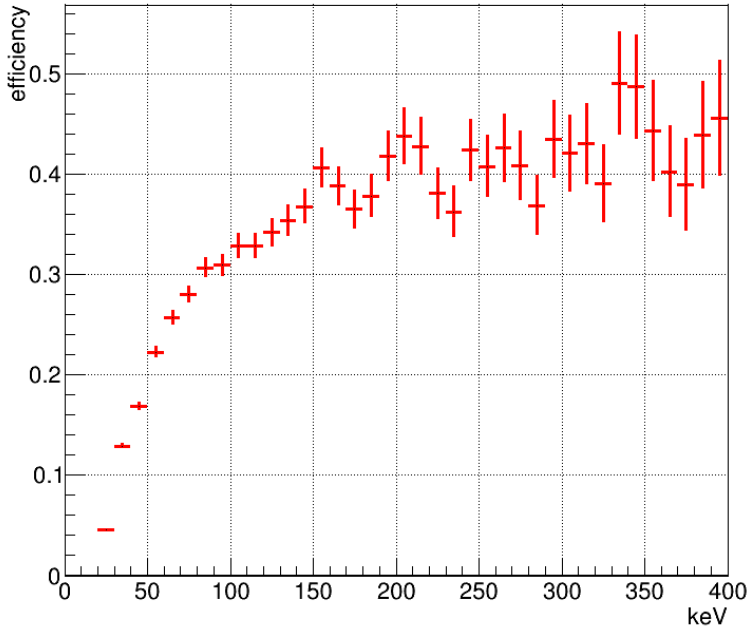

Figure 4.36: The detection efficiency of nuclear events after the length cut and the TOT-sum cut.

The energy spectra after the length cut and the TOT-sum cut are shown in Figure 4.37. It is known that roundness explained in Section 5.2 which is one of γ-ray cut parameters is related to the absolute coordinate in z. This cut was not used since the quantitative evaluation of the cut efficiency with respect to the drift distance is not. The α-ray detection efficiency at RUN22 ($\varepsilon_{\mathrm{gap,RUN22}}$ and $\varepsilon_{\mathrm{TPC,RUN22}}$) was defined similarly to Eq.(3.12) and (3.13) as follows,

$$\varepsilon_{\mathrm{gap,RUN22}} = \frac{e_{\mathrm{gap}}}{T_{\mathrm{all}}}, \tag{4.7}$$

$$\varepsilon_{\mathrm{TPC,RUN22}} = \frac{e_{\mathrm{TPC}}}{T_{\mathrm{all}}}. \tag{4.8}$$

These were obtained as $\varepsilon_{\mathrm{gap,RUN22}} = 2.1^{+3.1}_{-1.0} \times 10^{-2}$ and $\varepsilon_{\mathrm{TPC,RUN22}} = 1.7 \times 10^{-3}$, respectively. Since there was a possibility of detecting unknown backgrounds, the surface α-ray rate of RUN22 ($R_{\mathrm{gap,RUN22}}$ and $R_{\mathrm{TPC,RUN22}}$) were discussed with the upper limits. The surface α-ray rate R_{gap} and R_{TPC} can be calculated similarly to Eq.(3.14) and (3.15) as follows

$$R_{\mathrm{gap,RUN22}}\,[\alpha/\mathrm{cm}^2/\mathrm{h}] = \frac{I_{\mathrm{gap,RUN22}}[\mathrm{count/kg/day}] \times mass[\mathrm{kg}]}{\varepsilon_{\mathrm{gap}} \times S[\mathrm{cm}^2]}, \tag{4.9}$$

$$R_{\mathrm{TPC,RUN22}}[\alpha/\mathrm{cm}^2/\mathrm{h}] = \frac{I_{\mathrm{TPC,RUN22}}[\mathrm{count/kg/day}] \times mass[\mathrm{kg}]}{\varepsilon_{\mathrm{TPC}} \times S[\mathrm{cm}^2]}, \tag{4.10}$$

where, $I_{\mathrm{gap,RUN22}}$ and $I_{\mathrm{TPC,RUN22}}$ are the α rate per unit mass [kg] per unit time [day], " *mass* " is the target mass(=10.36 [g]) and S is the fiducial area ($= 24 \times 28$ [cm^2]). In the TPC region, there were only 3 events. The average detection efficiency in the TPC region was 0.41 ± 0.03. The error is the standard deviation of the detection efficiency in the TPC region. $I_{\mathrm{TPC,RUN22}}$ [count/kg/day] $< 6.68/(0.41-0.03\times1.64)/0.489 = 37.9$ [count/kg/day] was obtained at a 90 % confidence level (C.L.). Therefore, $R_{\mathrm{TPC,RUN22}} < 1.4\times10^{-2}$ [α/cm^2/h] was obtained at a 90 % C.L.. In the gap region, $R_{\mathrm{gap,RUN22}}$ is given an upper limit. From the above, the $R_{\mathrm{gap,RUN22}} < (3.09+2.98\times1.64)\times10^{-3} = 8.0\times10^{-3}$ [α/cm^2/h] (90 %C.L.) was obtained.

The measurement results using the standard μ-PIC (RUN14) and the low α-μ-PIC (RUN22) were summarized in Table 4.9. R_{HPGe} was calculated from Eq.3.11. Since $R_{\mathrm{gap,RUN22}}$ was a more strict limit than $R_{\mathrm{TPC,RUN22}}$, $R_{\mathrm{gap,RUN22}}$ was adopted and $R_{\mathrm{RUN22}} \equiv R_{\mathrm{gap,RUN22}}$ was defined. Comparing R_{RUN14} and R_{RUN22}, it was confirmed that the surface α-ray rate was less than 1/24. Since there is a possibility that unknown backgrounds exist, and lack of statistics, that the goal of 1/50 reduction was not confirmed. By understanding and taking into consideration the backgrounds with an increased statics, the background reduction of the low-α μ-PIC should be studied more precisely.

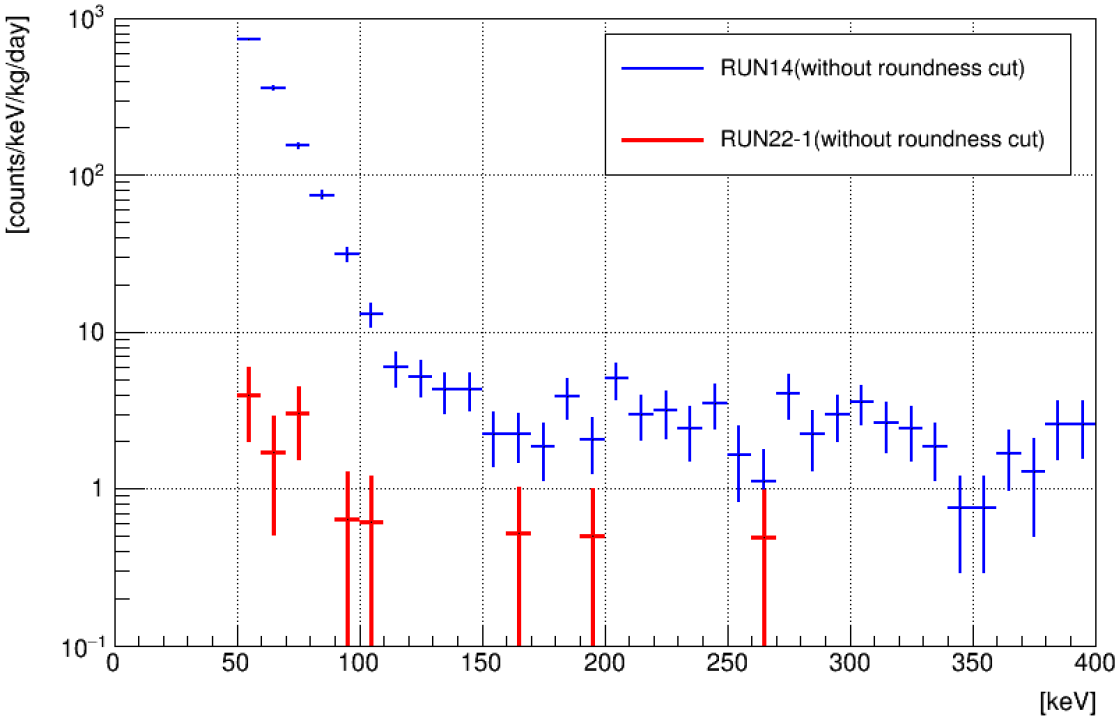

Figure 4.37: The energy spectra the length cut and the TOT-sum cut. The red histogram is RUN22-1 (this work). The blue (RUN14: Kamioka first run[35]) one is the previous work.

Table 4.9: The summary of the surface α-ray rate.

Method	$[\alpha/\mathrm{cm}^2/\mathrm{h}]$	Note
R_{HPGe}	$(1.93 \pm 0.07) \times 10^{-1}$	Standard μ-PIC
$R_{\mathrm{gap,RUN14}}$	$(5.0^{+12.5}_{-3.3}) \times 10^{-1}$	
$R_{\mathrm{TPC,RUN14}}$	$(1.9^{+0.3}_{-0.1}) \times 10^{-1}$	
$R_{\mathrm{gap,RUN22}}$	$< 8.0 \times 10^{-3}$ (90% C.L.)	Low-α μ-PIC
$R_{\mathrm{TPC,RUN22}}$	$< 1.4 \times 10^{-2}$ (90% C.L.)	

5 Discussion

5.1 Understanding the gas gain of the low-α μ-PIC

As discussed in Section 4.3.3, the gas gains of $30\times30\,\mathrm{cm}^2$ low-α μ-PIC were different from those of the $10\times10\,\mathrm{cm}^2$ low-α μ-PIC. The gas gain of the $30\times30\,\mathrm{cm}^2$ low-α μ-PIC was about $\times1.5$ larger than that of the $10\times10\,\mathrm{cm}^2$ low-α μ-PIC. The gas gains calculated by the simulation were not consistent with the measurement in the low-α μ-PIC. The simulation result was about $\times3.5$ and $\times2.3$ larger than the measurement result of the $10\times$ 10 cm^2 low-α μ-PIC and $30\times$ 30 cm^2 low-α μ-PIC, respectively. In this section, the reasons of these discrepancies are discussed. First, the measurement results are compared, then the simulation result and measurement results are compared.

Gas gains depend on the electric field structure. The geometrical parameters of the μ-PIC which would affect the electric field were the height of the anode electrode and the cathode electrode (t_{ac}), the diameter of the anode electrode (d_{a}), the diameter of the cathode hole (d_{c}), and the thickness of the insulator (d_{i}). These parameters of the μ-PICs, except d_{i} were measured. Gas gains were discussed based on these values in this chapter. The results are shown in Table 5.1. The result of the $30\times30\,\mathrm{cm}^2$ low-α μ-PIC were consistent with the result of $10\times10\,\mathrm{cm}^2$ low-α μ-PIC within the error. Figure 5.2, 5.3 and 5.4 show the dependence of gas gains on t_{ac}, d_{a} and d_{c} by the simulation. t_{ac} and d_{a} were changed by 5 µm step, and d_{c} was changed by 10 µm step. The step size of the parameter in the simulation is determined by the size of the mesh(<5 µm). The simulation results shown in Figure 5.2, 5.3 and 5.4 indicated that at least 5 µm of difference on these parameters were required to have a gain difference of $\times1.5$. The standard deviations of t_{ac}, d_{a} and d_{c} of 30 $\times$ 30 cm^2 low-α μ-PIC were 1.4 µm, 2.5 µm and 2.3 µm, respectively. The standard deviations of t_{ac}, d_{a} and d_{c} of 10 $\times$ 10 cm^2 low-α μ-PIC were 1.1 µm, 2.8 µm and 3.0 µm, respectively. These three parameters were found not to cause a sufficient change of the gain to explain the difference of the gains of the 30 $\times$ 30 cm^2 and the 10 $\times$ 10 cm^2 low-α μ-PIC.

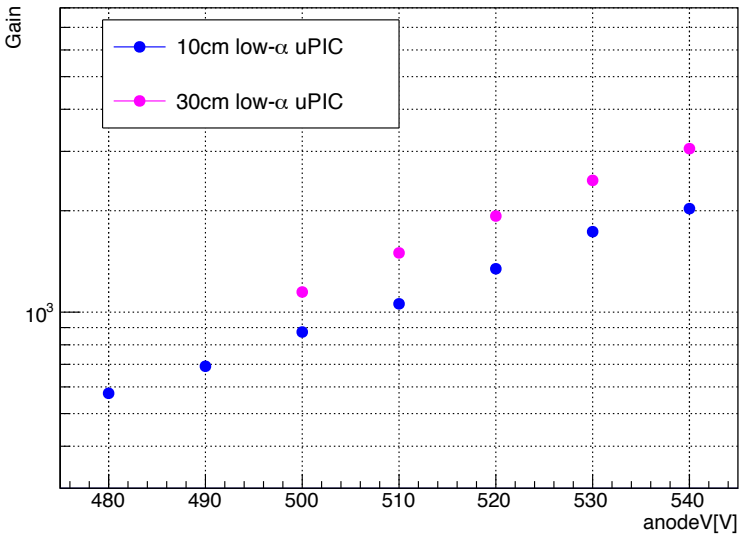

Figure 5.1: Gas gains as a function of the voltage supplied to the anode electrodes of the $10\times10\,\mathrm{cm}^2$ and $30\times30\,\mathrm{cm}^2$ low-α μ-PIC.

Table 5.1: The measurement results and the design value of each parameter of 30 × 30 cm^2 low-α μ-PIC and the 10 × 10 cm^2 low-α μ-PIC. Errors are the standard deviation.

Parameter	30× 30 cm^2 low-α μ-PIC [µm]	10× 10 cm^2 low-α μ-PIC [µm]	Design value [µm]
Height of anode and cathode electrode(t_{ac})	14.1 ± 1.4	15.4 ± 1.1	20
Diameter of anode electrode(d_a)	62.9 ± 2.5	64.4 ± 2.8	60
Diameter of cathode electrode(d_c)	242.3 ± 2.3	240.0 ± 3.0	250
Insulator thickness(d_i)			80

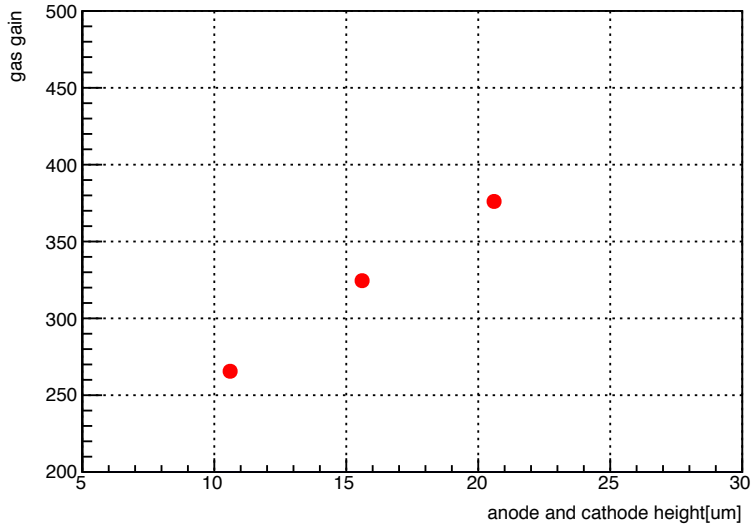

Figure 5.2: The geometry dependence of the gas gains calculated by the simulation. The parameter is the height of the anode and the cathode electrodes. The anode voltage is 400V.

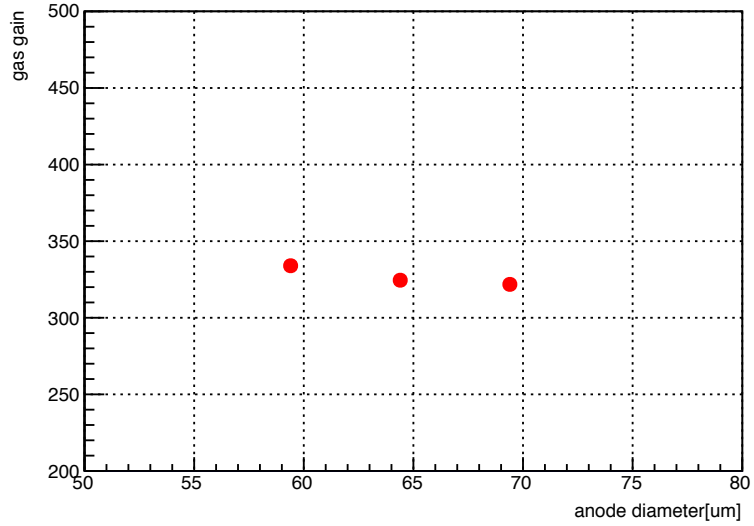

Figure 5.3: The geometry dependence of the gas gains calculated by the simulation. The parameter is the diameter of the anode electrodes. The anode voltage is 400V.

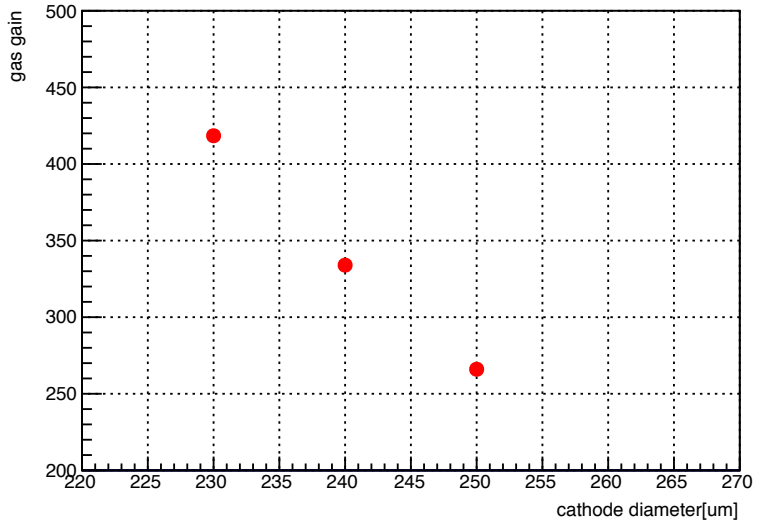

Figure 5.4: The geometry dependence of the gas gains calculated by the simulation. The parameter is the cathode holes. The anode voltage is 400V.

Next, the dependence of the gas gain on the thickness of the insulator was considered. The thickness of the insulator of a low-α μ-PIC can not be measured after the completion of the μ-PIC. If the thickness of the insulating layer of $30\times30\,\mathrm{cm}^2$ low-α μ-PIC was 80 µm and the thickness of the insulator of 10×10 cm^2 low-α μ-PIC was 50 µm, it can be explained that the gain differs by $\times1.5$. However, it is unlikely that the thickness of the insulator became to 50 µm during the low-α μ-PIC fabrication process.

From these discussion, no parameter combination was found to explain the gain difference between the $30\times$ 30 cm^2 low-α μ-PIC and $10\times$ 10 cm^2 low-α μ-PIC. It was considered that there might be still other parameters that have not yet been taken into consideration. From the same discussion as above, it was suggested that there would be unknown parameters affecting the gas gains in addition to the four parameters.

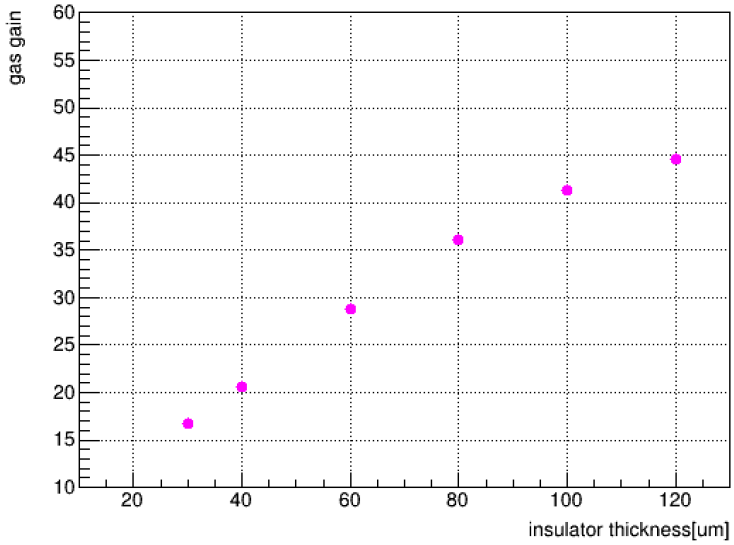

Figure 5.5: The dependence of the insulator thickness by the simulation.

5.2 Expected dark matter sensitivity using the low α μ-PIC

In this chapter, the detection sensitivity to dark matter was discussed. There is the roundness cut in addition to length cut and TOT-sum cut for the dark matter run. In this chapter, the roundness cut was introduced to compare with the previous dark matter search run (RUN14). This parameter was determined as follows by comparing the electron recoil events caused by the ^{137}Cs radiation source and the nuclear recoil events caused by the ^{252}Cf radiation source.

- **roundness-cut** : roundness > 0.04
  for the rejection of the events remained in ^{137}Cs-run shown in Figure 5.6. Roundness is defined as Eq 3.1.

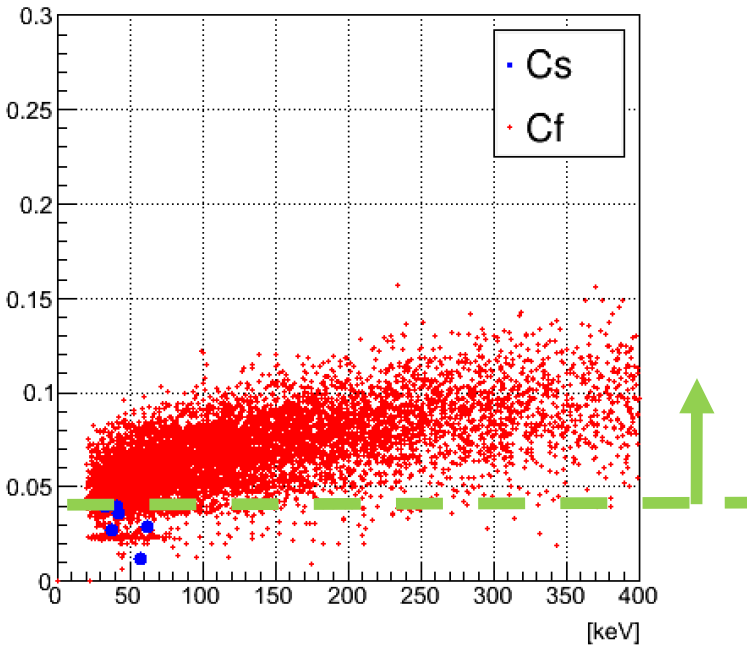

Figure 5.6: Energy dependence of the roundness after the length cut and TOT-sum cut.

Figure 5.7 shows the detection efficiency of the nuclear recoil events after the length cut, the TOT-sum cut and the roundness cut. The detection efficiency was about 20 % at 50 keV. The energy spectrum with roundness cut under the dark matter search environment is shown in Figure 5.8.

The improved sensitivity for the dark matter search was estimated from the obtained spectrum. The energy range for the dark matter search was $50 - 400$ keV. Integral values of RUN14 in the $50 - 400$ keV region was 1449 ± 102 counts/kg/day. The error is the statistical one. In RUN22, since these were 5 events in $50 - 400$ keV (1 event in $60 - 70$ keV bin, 3 events in $70 - 80$ keV bin and 1 event in $160 - 170$ keV bin), the event rate was discussed with a Poisson distribution for the 90 % confidence interval. The average value of the weighted detection efficiency by the number of events was 0.27. The event rate of RUN22 in $50 - 400$ keV was $5^{+4.99}_{-3.16}/0.489/0.27 = 38^{+38}_{-24}$ counts/kg/day. From the

comparison of the values, the sensitivity was estimated to be improved by a factor of 38^{+38}_{-24}(90 % interval).

Since the background spectrum of RUN 22 might be different from the one of RUN 14, the improvement factor was compared with those of the two subset energy ranges; i.e. $50 - 150$ keV and $150 - 400$ keV. The integral values of RUN14 in the $50 - 150$ keV region was 1375 ± 100 counts/kg/day. The error is the statistical one. In RUN22, since there were 4 events in $50 - 150$ keV the event rate was discussed with a Poisson distribution for the 90 % confidence interval. The average value of the weighted detection efficiency by the number of events was 0.25. The event rate of RUN22 in $50 - 150$ keV was $4^{+4.60}_{-2.53}/0.489/0.25 = 33^{+38}_{-21}$ counts/kg/day. From the comparison of the values, the sensitivity was estimated to be improved by a factor of 42^{+48}_{-27}(90 % interval). The integral value of RUN14 in the $150 - 400$ keV region were 74 ± 16 counts/kg/day. In RUN22, since there was only 1 event in the $150 - 400$ keV region, the event rate was discussed with a Poisson distribution for the 90 % confidence interval.The average detection efficiency in the $150 - 400$ region at RUN22 was 0.41. The event rate in the $150 - 400$ region was $1^{+3.36}_{-0.89}/0.489/0.41 = 5^{+17}_{-4}$ count/kg/day. From the comparison of the values, the sensitivity was estimated to be improved by a factor of 15^{+50}_{-12}(90 % interval). Since the sensitivity estimated from $50 - 400$ keV was consistent with the sensitivities estimated from two subset energy regions, the value from the $50 - 400$ keV region were used for the further discussion.

The expected sensitivity is shown in Figure 5.9. Here, the estimation was assumed that the spectrum shape of RUN22 at $50 - 400$ keV was not changed from the spectrum of RUN14. The detection sensitivity is expected to be improved by a factor of 38^{+38}_{-24}(90 % interval) than the one of RUN14. It was expected to reach the DAMA region which was the target of this thesis. The dark matter sensitivity was improved by this work so that the sensitivity reached the DAMA region at confidence level very close to 90 %.

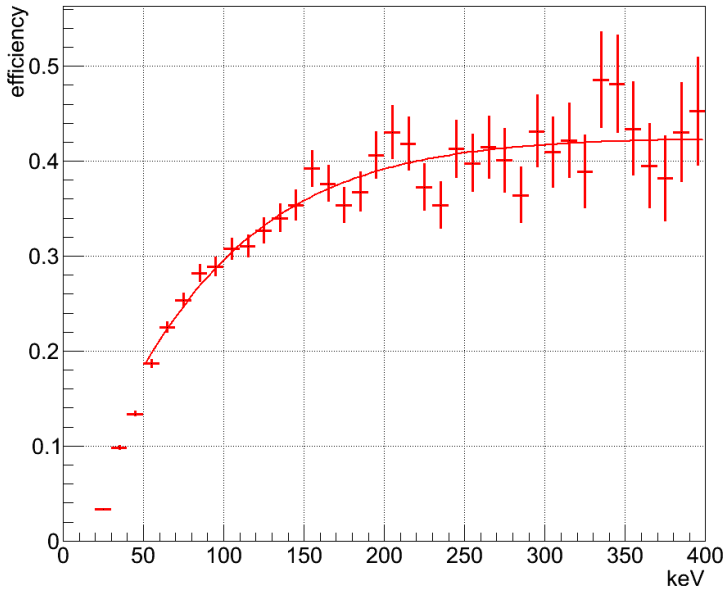

Figure 5.7: The detection efficiency of nuclear events after the length cut, the TOT-sum cut and the roundness cut.

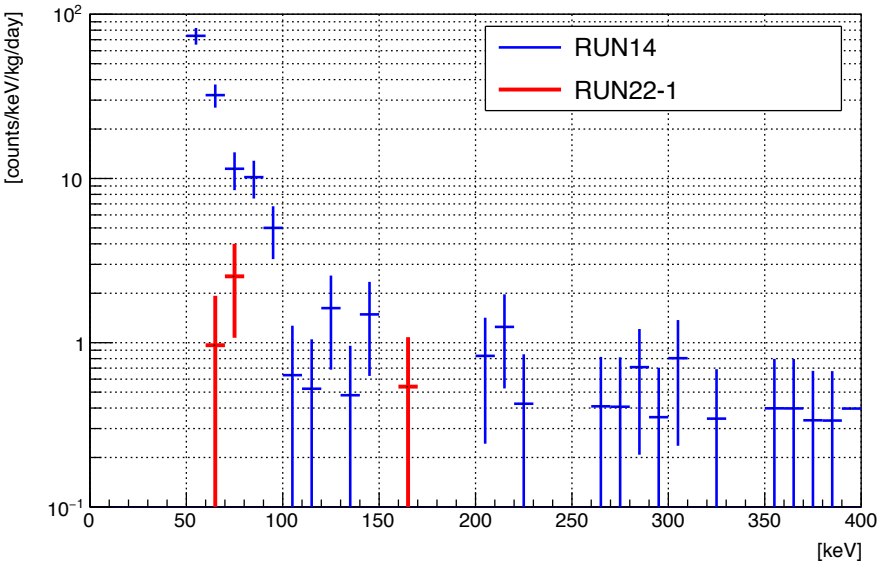

Figure 5.8: Measured energy spectrum. The red histogram is RUN22-1 (this work). The blue (RUN14: Kamioka first run)[35] one is the previous work.

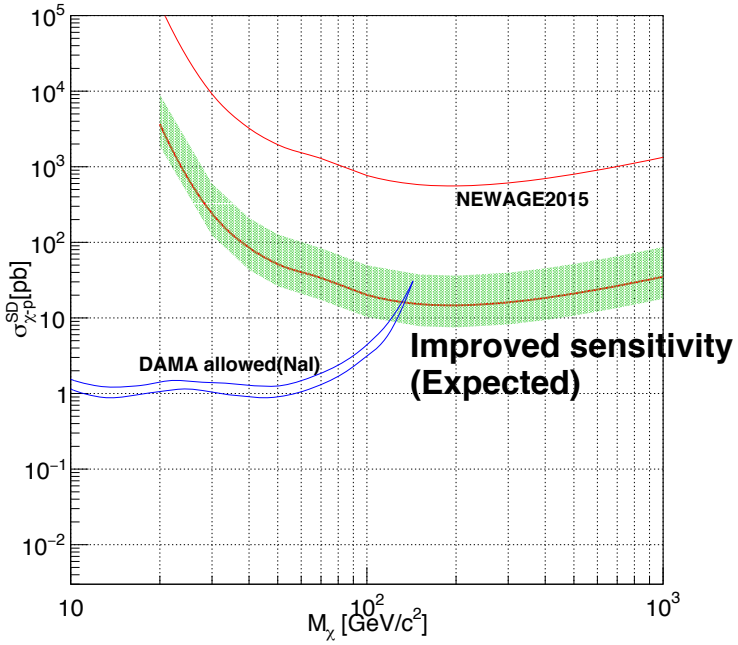

Figure 5.9: The expected sensitivity (“ Improved sensitivity ”). The green band represents the error relative to the detection sensitivity from a Poisson distribution for 90 % confidence interval. The horizontal axis shows the mass of the WIMP, and the vertical axis shows the scattering cross section in the SD interaction of protons and WIMP.

6 Conclusions

NEWAGE is a direction sensitive dark matter search experiment read by a μ-TPC using μ-PIC. NEWAGE has the world's highest sensitivity in the direction sensitive method. However, the detection sensitivity of NEWAGE has not reached those of the conventional method, and a further improvement was required. The detection sensitivity of NEWAGE was limited by the backgrounds, and understanding and reduction of the backgrounds was necessary.

As a result of this thesis, the main background of NEWAGE was found to be " gap events " due to α-rays caused by the decay of the U/Th series contained in the glass cloth in the μ-PIC. A " low-alpha μ-PIC " with the background source removed was developed. Low-α μ-PICs with sizes of 10×10 cm^2 and 30×30 cm^2 were produced without any problem and their performances were precisely studied. The low-α μ-PIC was confirmed to show the required gas gain (1000 at 760 Torr of argon-ethane gas mixture (9:1)). The non-uniformity of the gas gain (19 %) also satisfied the requirement(20 %). The α-ray background was studied in Kamioka underground laboratory. As a results of the background study, it was found that the α-ray emission was reduced to 1/24 or less compared with the standard μ-PIC. Although the requirement value of 1/50 was not confirmed mainly because the lack of the statistics, this result was a very promising one. The detection sensitivity is expected to be improved by a factor of 38^{+38}_{-24}(90 % interval) than the one of RUN14. The dark matter sensitivity was improved by this work so that the sensitivity reached the DAMA region at confidence level very close to 90 %.

Acknowledgements

I would like to first thank the staffs of Kobe University for helping my research activities. I am deeply grateful to Associate professor Kentaro Miuchi for his guidance and encouragements in this work. This thesis would not be completed without his support. His leadership always led me to the right direction so that I can accomplish researches throughout my master and doctoral programs in Kobe University. I am also grateful to Dr. Kiseki nakamura. He taught me a lot of things about the analysis and experiment. Without his advice, my study would not have been going well. I would like to express my gratitude to Associate professor Atsuhiko Ochi. Without his help, I would not have understood the gas detectors. I would like to express my great gratitude to Professor Yasuo Takeuchi and Professor Hisatomo Harima. Yumi Yokoyama and Kazumi Yoshida supported my research activities as a secretary of the Kobe particle physics group. I would like to thank them. I thank to the member of Kamioka institution for helping underground experiments: Hiroyuki Sekiya, Koichi Ichimura, Kazuyoshi Kobayashi and Ko Abe. I specially thank the NEWAGE collaborators: Ryota Yakabe, Yushiro Yamaguchi, Tomonori Ikeda, Miki Nakazawa, Hirohisa Ishiura, Hiroshi Ito and Takuma Nakamura. Thanks to them, I had a good time.

Finally, I would like to express my deepest thanks to my family. I could not spend my research life without their support.

References

[1] Planck Collaboration A&A 571,A16 (2014).

[2] F. Z. et al. Astrophys. J. (1937) 217.

[3] K. G. Begeman, A. H. Broeils, and R. H. Sanders MNRAS (1991) 523.

[4] D. Crowe et al., Astrophys. J. 648 (2006) L109 .

[5] R. A. Knop et al. Astrophys. J. 598 (2003) 102.

[6] D. J. Eisenstein et al. Astrophys. J. 633 (2005) 560.

[7] D. Kirkman, D. Tytler, N. Suzuki, J. M. O'Meara and D. Lubin *et al.*, Astrophys. J. Suppl. Ser. 149 (2003) 1.

[8] R. D. Peccei and Helen R. Quinn et al. Phys. Rev. Lett. 38 (1977) 1440.

[9] A. Boyarsk et al. Ann. Rev. Nuc. Part. Sci. 59 (2009) 191.

[10] Hardy M. Hodges Phys. Rev. D 47 (1993) 456.

[11] G. Jungman *et al.*, Phys. Rep. 267 (1996) 195

[12] H. Nishimura Doctor Thesis Kyoto University (January 2009).

[13] J. D. Lewin and P. F. Smith Astropart. Phys. 6 (1996) 87.

[14] R. Bernabei et al.rPhysics Letters B 424 (1998) 195-201

[15] R. Bernabei et al. Phys. Lett. B 480 (2000) 23.

[16] R. Bernabei et al. arXiv:1805.10486v1.pdf.

[17] PRL 113, 081302 (2014).

[18] D. Spergel Phys. Rev. D 37 (1988) 1353.

[19] J.B.R. Battat et al. Astroparticle Physics 91 (2017) 65-74.

[20] S. Ahlen et al. Phys. Lett. B 695 (2011) 124.

[21] Q̈ Şahin et al, JINST 2010 P05002.

[22] Particle Data Group, 2014 Review of Particle Physics., Chapter 31. PARTICLE DETECTORS AT ACCELERATORS http://http://pdg.lbl.gov/2015/download/rpp2014-Chin.Phys.C.38.090001.pdf

[23] F. Sauli, *GEM: A new concept for electron amplification in gas detectors Nucl. Instr. and Meth. A* **386** (1997) 531.

[24] Fabio Sauli, Nuclear Instruments and Methods in Physics Research A 805 (2016) 2-24

[25] https://gdd.web.cern.ch/GDD/gemgeneral.html

[26] Y.Giomataris, et al. Nuclear Instruments and Methods in Physics Research A 376 (1996) 29-35

[27] A. Ochi, et al., Nucl. Instr. and Meth. A 471 (2001) 264.

[28] S.Cebrian et al., Astropart. Phys. 34 (2011) 354.

[29] J. Castel et al. arXiv:1812.04519v1.

[30] F.J. Iguaz et al., Eur. Phys. J. C 76, 529 (2016)

[31] Radioisotope Pocket Data Book 11th Edition Japan Radioisotope Association(JRIA)

[32] Table of Isotopes Richard B.Firestone Virginia S. Shirley.

[33] K. Nakamura Doctor Thesis Kyoto University (January 2014).

[34] T. Hashimoto Master Thesis Kobe University (February 2015).

[35] K. Nakamura et al. Prog. Theor. Exp. Phys. (2015) 043F01.

[36] R. Yakabe Doctor Thesis Kobe University (January 2018).

[37] J.F. Ziegler, J.P. Biersack SRIM The Stopping and Range of Ions in Matter, Code (1985).

[38] S. Agostinelli et al. Nucl. Instr. Meth. Phys. Res. A 506 (2003) 250.

[39] Garfield++, Version v1r0 ,http://garfieldpp.web.cern.ch/garfieldpp/

[40] http://heed.web.cern.ch/heed/

[41] http://magboltz.web.cern.ch/magboltz/

[42] C. Geuzaine and J.-F. Remacle, International Journal for Numerical Methods in Engineering 79(11), pp. 1309-1331, 2009.

[43] https://www.csc.fi/web/elmer

[44] A. Takada,et al. Journal of Instrumentation 8 C10023 (2013).